Developement od Multiband Band-Pas Filters in Planar Technologies

Yi Wu

THÈSE DE DOCTORAT DE

L'INSTITUT NATIONAL DES SCIENCES APPLIQUÉES RENNES

ECOLE DOCTORALE N° 601
Mathématiques et Sciences et Technologies de l'Information et de la Communication
Spécialité : *Électronique*

Par

Yi WU

Development of Multiband Band-Pass Filters in Planar Technologies

Thèse présentée et soutenue à Rennes, le 18 Juin 2021
Unité de recherche : Institut d'Électronique et des Technologies du numéRique (IETR -- UMR CNRS 6164)

Thèse N° : 21ISAR 18 / D21 - 18

Rapporteurs avant soutenance :

Stéphane BILA	Directeur de Recherche, XLIM, Limoges
Gaëtan PRIGENT	Maître de Conférence, HDR, ENSEEIHT, Toulouse

Composition du Jury :

Président :	Cédric QUENDO	Professeur, Université de Bretagne Occidentale, Brest
Examinateurs :	Stéphane BILA	Directeur de Recherche, XLIM, Limoges
	Gaëtan PRIGENT	Maître de Conférence, HDR, ENSEEIHT, Toulouse
	Florence PODEVIN	Maître de Conférences, HDR, Université Grenoble Alpes
	Cédric QUENDO	Professeur, Université de Bretagne Occidentale, Brest
	Erwan FOURN	Maître de Conférences, HDR, INSA, Rennes
Dir. de thèse :	Philippe BESNIER	Directeur de Recherche, IETR, Rennes

Table of Contents

RÉSUMÉ EN FRANÇAIS

Les systèmes de communication émergents se doivent désormais d'être polyvalents et compatibles avec plusieurs normes ou standards de communication, et parfois simultanément. Ceci a généré une demande nouvelle de composants RF ou micro-ondes pouvant fonctionner sur plusieurs plages de fréquences tout en conservant des spécifications exigeantes en termes de compacité, de performances radio-électriques ou encore de coût. Parmi tous les composants d'une chaîne d'émission/réception, les filtres passe-bande jouent un rôle clé dans la sélection des signaux d'intérêt. Ils y occupent aussi une surface importante de par leur nombre et leur encombrement. Leur importance et leur empreinte est donc d'autant plus grande dans les systèmes multibandes et leur intégration d'autant plus difficile.

Les filtres multi-bandes apparaissent ainsi comme une solution attractive pour sélectionner simultanément plusieurs bandes de fréquence tout en réduisant l'empreinte et le coût des circuits. Ils font l'objet d'une attention particulière du monde de la recherche depuis le début des années 2000 avec de nombreux travaux sur les cas bi- ou tri-bandes notamment [1, 2, 3, 4, 5, 6]. Les travaux proposant un nombre de bandes plus importants sont beaucoup plus rares [7, 8]. L'objectif de cette thèse est donc d'étudier et de développer des nouvelles solutions de synthèse et de nouvelles méthodes de conception de filtres multibandes avec un nombre quelconque de bandes passantes simultanées. Leur implémentation en technologie microruban sous diverses topologies a également été mise en oeuvre.

Le mémoire se décline en 6 chapitres (incluant l'introduction formant le chapitre 1 et les conclusions et perspectives décrites au chapitre 6) auxquels s'ajoute une annexe donnant des éléments théoriques ou expérimentaux complémentaires non décrits directement dans le corps du manuscrit par souci de clarté.

Chapitre 2 : État de l'art

Après une présentation des principaux outils théoriques associés au développement de filtres qui seront utilisés dans le cadre de cette thèse, le mémoire commence par un état de l'art des filtres micro-ondes multibandes. Il a ainsi été mis en évidence quatres méthodes principales pour concevoir de tels filtres. La première méthode consiste simplement à connecter ensemble des filtres passe-bande et coupe-bande [4, 5, 6]. Un exemple simplement basé sur l'association série d'un filtre passe-bande avec un filtre coupe-bande est présenté en Figure 1.

La seconde méthode consiste simplement à connecter ensemble plusieurs filtres mono- ou

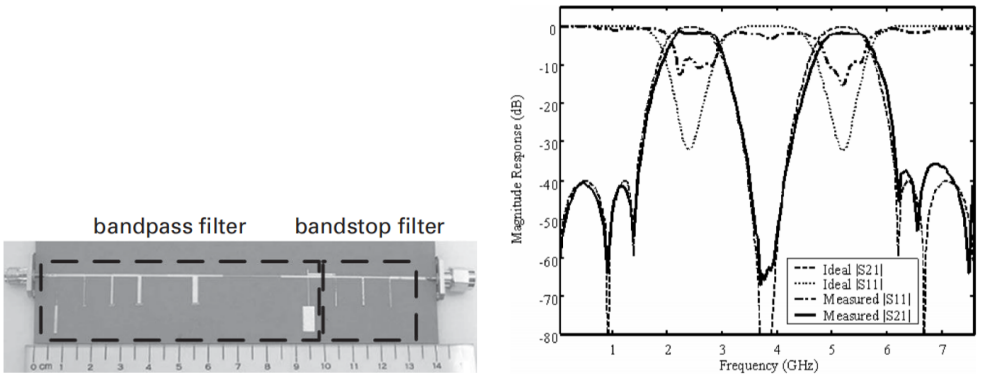

(a) (b)

FIGURE 1 – Représentation schématique (a) et réponses en fréquence (b) d'un filtre bi-bande proposé dans [4].

bi-bandes [9, 10]. La Figure 2 présente un exemple de filtre bi-bande conçu suivant ce concept [9]. Deux filtres passe-bandes composés de résonateurs en anneaux en boucle ouverte repliés permettent d'obtenir ce filtre bi-bande, chaque filtre pouvant être facilement réglé individuellement.

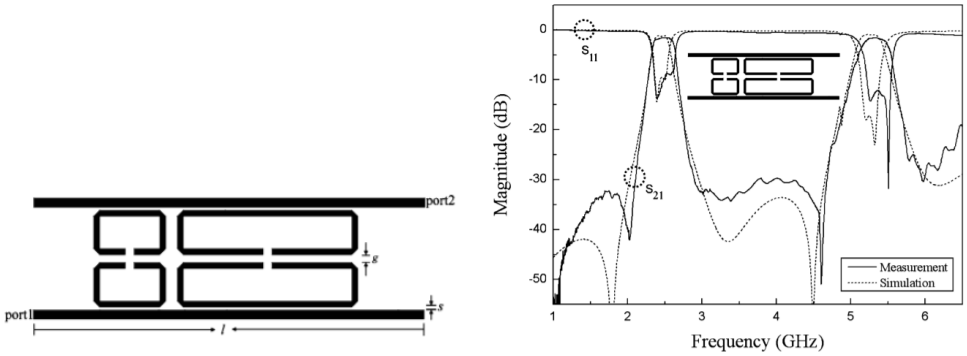

(a) (b)

FIGURE 2 – Représentation schématique (a) et réponses en fréquence (b) d'un filtre bi-bande proposé dans [9].

L'utilisation de résonateurs multi-modaux constitue la brique de base de la troisème méthode de conception de filtres multibandes. Ces résonateurs multimodaux sont des structures pouvant supporter simultanément plusieurs modes de résonance dont les fréquences ne sont pas les harmoniques les unes des autres. C'est une solution très attractive notamment pour la conception de filtres multibandes compacts. En technologies planaires, ce sont surtout des résonateurs à saut d'impédance (SIR pour Stepped-Impedance Resonator en anglais) qui sont utilisés [11, 12, 13]. Cette méthode est aussi relativement facilement applicable à des technologies volumiques [14, 15] (cf. Figure).

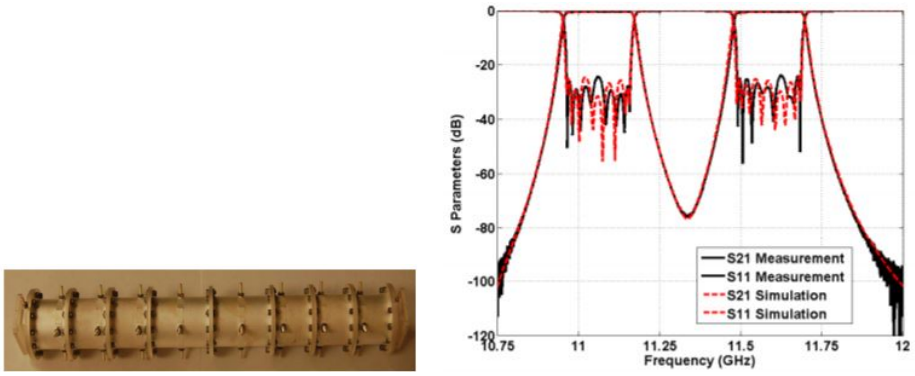

(a) (b)

FIGURE 3 – Photographie d'un filtre bi-bande volumique (a) et réponses associées (b) [14].

La dernière méthode fait appel à des techniques avancées basées sur des outils plus théoriques comme l'optimisation de matrices de couplage [7, 16] ou la transformation de fréquence [17, 18]. Si l'approche basée sur les matrices de couplage donne de très bons résultats (cf. Figure **??**), elle nécessite l'optimisation d'un très grand nombre de paramètres, même pour un nombre relativement limité de bandes passantes, ce qui implique l'utilisation de ressources informatiques importantes. Quant à la transformation de fréquence, elle permet de passer d'un prototype passe-bas normalisé à un filtre multibande dénormalisé de manière complètement analytique. Elle a donc l'avantage d'être directe et rapide mais seuls les cas bi-bandes et tri-bandes étaient décrits jusqu'à présent dans l'état de l'art. Cette méthode, applicable à un grand nombre de topologies et de technologies différentes, est très prometteuse pour la conception de filtres multibandes à condition de pouvoir développer une synthèse analytique pour un nombre quelconque de bandes passantes. C'est donc principalement à partir de cette technique qu'ont été développés les travaux effectués pendant cette thèse.

Chapitre 3 : Synthèse directe de filtres passe-bande multibandes par transformation de fréquence

Le principe de la transformation de fréquence est d'associer toutes les bandes passantes d'un filtre multibande au prototype passe-bas dans le domaine normalisé comme le présente la Figure 5. Cette transformation se base sur l'équation de passage d'un prototype passe-bas normalisé vers un filtre dénormalisé. Cette équation de transformation, bien connue dans le cas de filtres passe-bas, passe-haut, passe-bande ou coupe-bande dénormalisés, peut s'exprimer de la façon

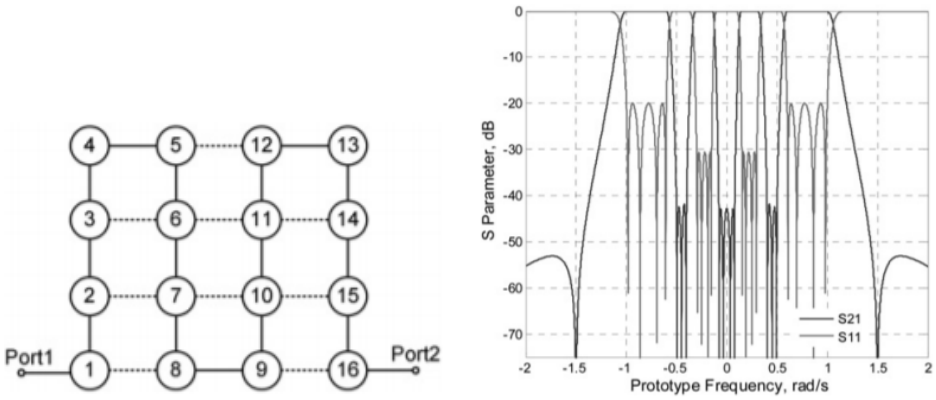

(a) (b)

FIGURE 4 – Schéma de couplage d'un filtre multibande (a) et réponse associée basée sur un algorithme d'approximation (b) proposé dans [16].

suivante dans le cas d'un filtre multibande à N bandes passantes :

$$\begin{aligned}\Omega &= T^{(N)}(\omega) \\ &= b_0\left(\frac{\omega}{\omega_0} - \frac{\omega_0}{\omega}\right) - \sum_{k=1}^{N-1} \frac{1}{b_k\left(\frac{\omega}{\omega_k} - \frac{\omega_k}{\omega}\right)}\end{aligned} \tag{1}$$

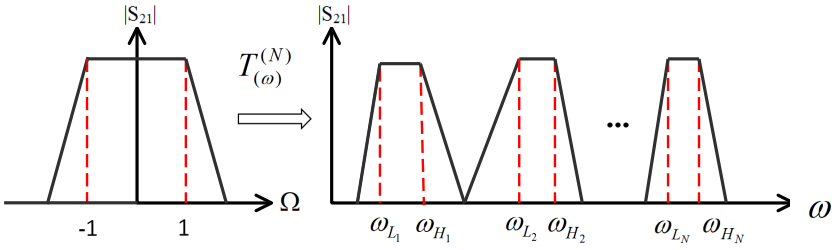

FIGURE 5 – Transformation de fréquence d'un prototype passe-bas normalisé vers un filtre multibande dénormalisé.

Dans cette équation, $T^{(N)}$ est la fonction de transformation, ω_0 et b_0 sont respectivement la pulsation de résonance et le paramètre de pente du filtre passe-bande global et les paramètres ω_k et b_k ($k \in [1; N-1]$) sont ceux des $N-1$ filtres coupe-bandes venant diviser le premier en N bandes passantes. La procédure complète de synthèse pour un nombre N quelconque de bandes passantes est présentée en détails dans ce chapitre, avec l'ensemble des outils mathématiques associés. Cette procédure permet d'exprimer les paramètres de sorties (les pulsations de résonance ω_k et les paramètres de pente b_k ($k \in [0; N-1]$)) en fonction des paramètres d'entrée, à

savoir les fréquences de coupure basses et hautes des différentes bandes passantes (ω_{L_i} et ω_{H_i}, cf. Figure 5).

L'équation de transformation de fréquence proposée ici (1) conduit à des résonateurs multi-bandes en étoile comme le présente la Figure 6. Une capacité du prototype passe-bas normalisé est alors transformée en un résonateur multibande composé d'un résonateur passe-bande et de $N-1$ résonateurs coupe-bandes en parallèle (cf. Figure 7). A partir de cette transformation, plusieurs exemples avec 3, 4 ou 5 bandes passantes ont été conçus et fabriqués en technologie microruban. Un exemple de filtre à 5 bandes passantes est présenté en Figure 8 avec ses résultats de simulations électromagnétiques (EM) et de mesures. Ces dernières sont, comme pour les autres exemples, en très bonne corrélation, validant les méthodologies de synthèse et d'implémentation proposées.

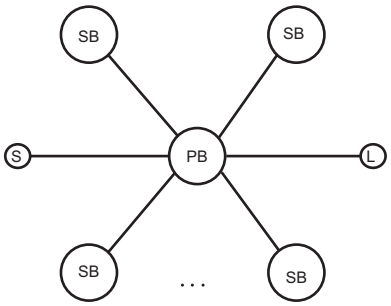

FIGURE 6 – Représentation schématique d'un résonateur multibande en étoile.

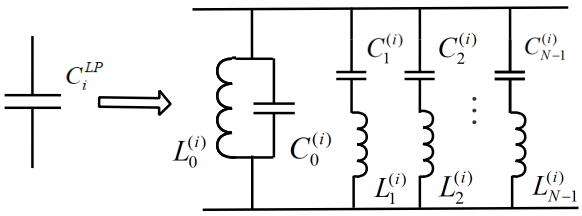

FIGURE 7 – Transformation d'une capacité du prototype passe-bas normalisé en un résonateur multibande.

Au-delà de 5 bandes, comme on peut le constater sur la Figure 8, l'implémentation monocouche à base de stubs utilisée dans ces premiers exemples devient très délicate en raison du manque de place disponible pour insérer de nouveaux stubs. Une solution alternative multicouche a donc également été étudiée dans le cadre de cette thèse. Cette solution bien qu'intéressante reste difficile à mettre en oeuvre.

Ce chapitre se poursuit par la présentation d'une autre solution d'implémentation à base de lignes couplées et non plus de stubs. Un exemple de filtre quadri-bande et ses résultats de simulations EM et de mesures sont présentés sur la Figure 9.

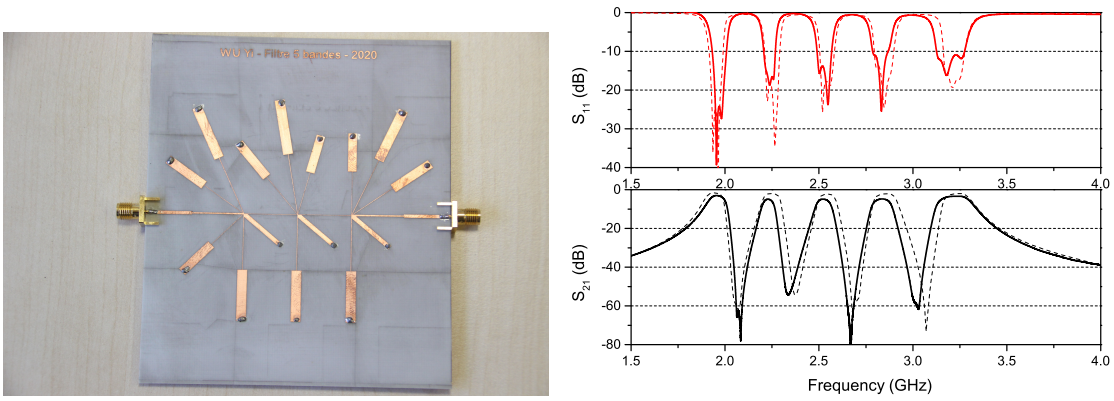

(a) (b)

FIGURE 8 – Photographie du filtre 5-bandes réalisés (a) et ses résultats de simulations EM (lignes discontinues) et de mesures (lignes continues) (b).

A la fin de ce chapitre, l'aspect très général de cette technique de synthèse de filtres multi-bandes est mis en avant à travers divers exemples de filtres en lignes idéales utilisant d'autres approximations (Butterworth, elliptique). Certaines limites sont aussi présentées. Enfin, une conclusion vient terminer ce chapitre en résumant les points majeurs qui y sont présentés.

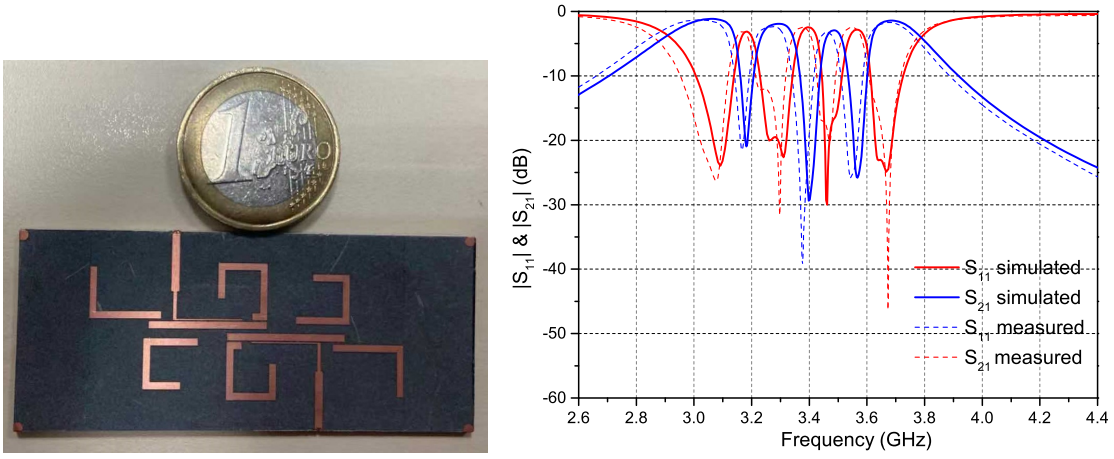

(a) (b)

FIGURE 9 – Photographie du filtre quadri-bandes à lignes couplées réalisés (a) et ses résultats de simulations EM (lignes continues) et de mesures (lignes discontinues) (b)

Chapitre 4 : Synthèse de filtres passe-bande multibandes en topologie en ligne

Une des limites de la méthode de synthèse proposée dans le chapitre 3 est l'implémenta-

tion technologique dans les cas d'un grand nombre de bandes passantes. Une nouvelle solution simplifiant cette implémentation est proposée dans le chapitre 4. Elle se base aussi sur une transformation de fréquence mais avec une nouvelle fonction de transformation $T^{(N)}$ donnée en équation (2). Cette nouvelle fonction de transformation se traduit par une structure en ligne des résonateurs multibandes (cf. Figure 10(a)) et non plus en étoile. Une capacité du prototype passe-bas normalisé est alors transformée en une structure en échelle comme celle présentée en Figure 10(b).

$$\Omega = T^{(N)}(\omega) = b_0\left(\frac{\omega}{\omega_0} - \frac{\omega_0}{\omega}\right) - \cfrac{1}{b_1\left(\frac{\omega}{\omega_1} - \frac{\omega_1}{\omega}\right) - \cfrac{1}{b_2\left(\frac{\omega}{\omega_2} - \frac{\omega_2}{\omega}\right) - \cfrac{1}{b_3\left(\frac{\omega}{\omega_3} - \frac{\omega_3}{\omega}\right)\cdots - \cfrac{1}{b_{N-1}\left(\frac{\omega}{\omega_{N-1}} - \frac{\omega_{N-1}}{\omega}\right)}}}}, \tag{2}$$

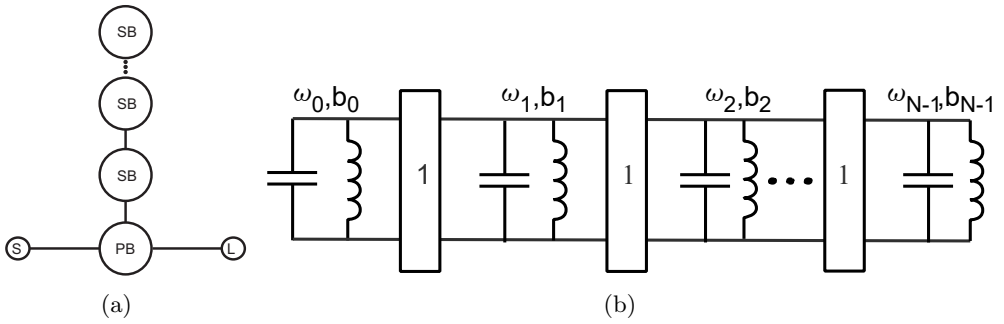

(a) (b)

FIGURE 10 – Représentation schématique d'un résonateur multibande en ligne (a) et circuit LC équivalent issu de la transformation d'une capacité du prototype passe-bas normalisé (b).

Une première méthode d'extraction des pulsations de résonance (ω_k) et des paramètres de pente (b_k, $k \in [0; N-1]$) en fonction des pulsations de coupure basses et hautes est développée sur le même principe que dans le chapitre 3. Cependant, la complexité mathématique associée à cette nouvelle fonction de transformation n'a permis le développement des synthèses que dans les cas tri-bandes et quadri-bandes et non l'obtention d'une méthode générale quel que soit le nombre de bandes.

Une seconde méthode est alors proposée pour contourner cette limitation. Elle est basée sur les techniques d'extraction des paramètres d'un circuit en échelle présentée dans [19]. Cette méthode est détaillée dans ce chapitre et un exemple d'application à un cas tri-bande est également développé. Il faut noter que cette méthode nécessite l'introduction d'une réactance indépendante de la fréquence (FIR pour Frequency-Invariant Reactance) dans le prototype passe-bas normalisé. Ceci permet de rendre cette transformation physiquement réalisable. En pratique, cela revient à produire la réponse présentée sur la Figure 11 dans le domaine passe-bas normalisé.

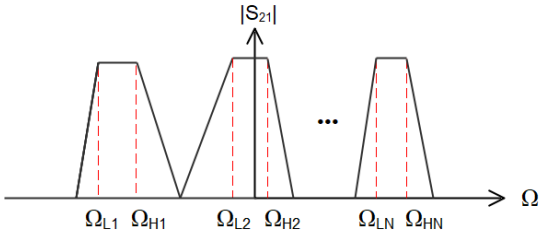

FIGURE 11 – Réponse multibande normalisée obtenue par l'ajout de FIR.

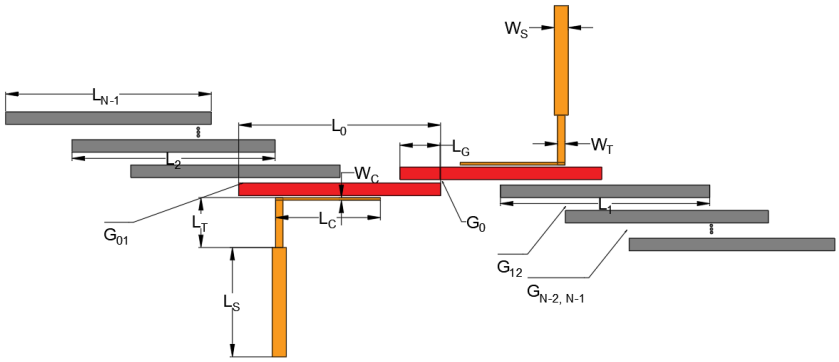

FIGURE 12 – Représentation générale de filtres multibandes basés sur une topologie en ligne et implémentés en lignes couplées (en jaune : les lignes d'accès, en rouge les résonateurs passe-bandes et en gris les résonateurs coupe-bandes).

Plusieurs exemples de filtres multibandes (de 3 à 6 bandes passantes) sont présentés dans ce chapitre pour valider le concept présenté. Cette fois, c'est une structure utilisant uniquement des lignes couplées qui a été privilégiée, cette dernière permettant d'intégrer facilement un grand nombre de résonateurs coupe-bande (et donc de créer un grand nombre de bandes passantes) tout en conservant un circuit relativement compact. Le schéma général d'une telle structure est donné en Figure 12. La Figure 13 présente un exemple de filtre à 6 bandes passantes et les résultats de simulations EM et de mesures associés. Comme pour les autres exemples présentés dans ce chapitre, ces derniers présentent une très bonne corrélation.

Ce chapitre 4 s'achève sur une conclusion qui comme pour le chapitre précédent synthétise l'ensemble des apports majeurs qui y sont développés.

Chapitre 5 : Synthèse directe de filtres passe-bande multibandes basée sur l'association de résonateurs coupe-bandes

Dans ce cinquième chapitre, une méthode rapide de conception de filtres multibandes est proposée. Contrairement à celles présentées dans les chapitres précédents, cette dernière méthode

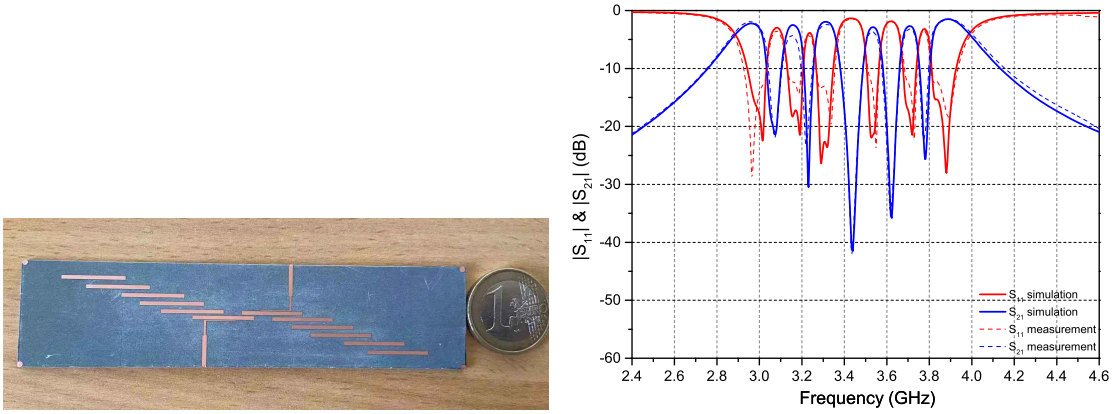

(a) (b)

FIGURE 13 – Photographie d'un filtre à 6 bandes passantes (a) et réponses simulées (lignes continues) et mesurées associées (lignes discontinues) (b).

n'est pas analytique et utilise des phases d'optimisation pour déterminer les paramètres des filtres. Elle impose aussi certaines contraintes (dimension globale, dépendance de certains zéros de transmission, etc.). Cependant, elle permet d'obtenir des filtres multibandes très simplement et très rapidement, les phases d'optimisation étant très courtes.

Le principe est d'associer en étoile à nouveau des résonateurs coupe-bandes mais uniquement coupe-bandes contrairement à la solution proposée au chapitre 3 qui intégrait dans l'étoile un résonateur passe-bande. Un résonateur N bandes basé sur cette association de $N-1$ résonateurs coupe-bandes a donc l'allure présentée sur la Figure 14. La réponse est alors constituée de $N+1$ zéros de transmission. Chaque branche de l'étoile crée indépendamment un zéro de transmission, f_{z1} à F_{zN-1}. A ces $N-1$ zéros, il faut ajouter un premier zéro, f_{z0} à la fréquence nulle et un dernier f_{zN} qui est le premier harmonique de f_{z1} ($f_{zN} = 2f_{z1}$).

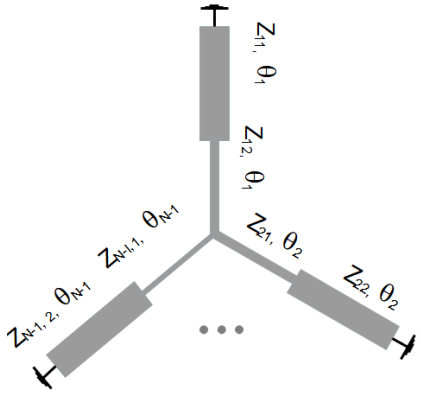

FIGURE 14 – Topologie de résonateurs multibandes basés sur l'association de résonateurs coupe-bandes.

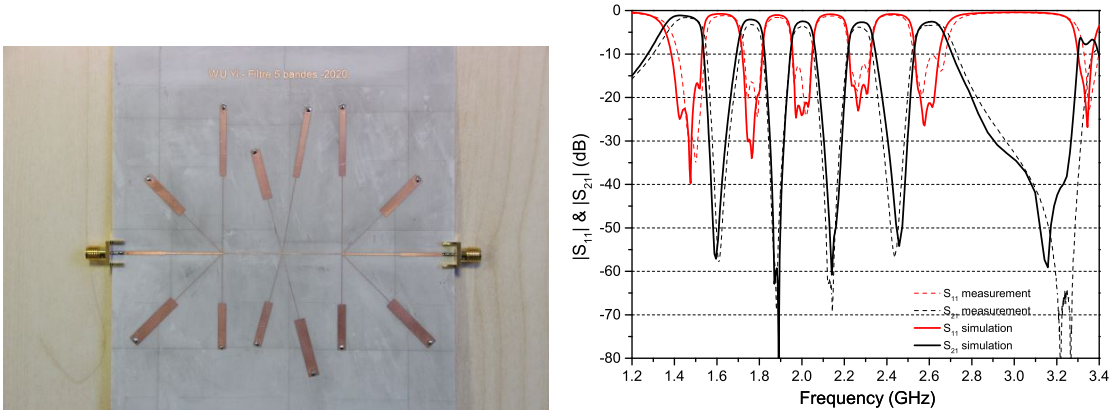

(a) (b)

FIGURE 15 – Photographie du filtre à 5 bandes réalisé basé sur l'association de résonateurs coupe-bandes (a) et ses réponses associées en simulations EM (lignes continues) et en mesures (lignes discontinues) (b).

La démarche de conception est décrite à travers le développement d'un filtre bi-bande. Elle est ensuite appliquée à la réalisation de plusieurs autres filtres multibandes ayant 3, 4 ou 5 bandes passantes. La Figure 15 présente la photographie du filtre à 5 bandes passantes ainsi conçu et ses réponses en fréquence associées.

Avant de se terminer par la traditionnelle conclusion résumant les points qui y sont développés, ce chapitre présente une comparaison des filtres à 4 et 5 bandes qui y sont présentés avec quelques exemples de filtres issus de l'état de l'art.

Chapitre 6 : Conclusion et perspectives

Ce mémoire se termine par une conclusion qui reprend l'ensemble des contributions de cette thèse, à savoir les 3 méthodes de conception de filtres multibandes présentées succinctement dans ce résumé en langue française et détaillées successivement aux chapitres 3, 4 et 5. Vient alors une section prospective ouvrant sur de possibles travaux futurs essentiellement dans la continuité des méthodes analytiques présentées en chapitres 3 et 4. La possibilité de filtres multibandes présentant une structure mixant les topologies en étoile et en ligne est ainsi évoquée. Une seconde perspective intéressante proposée dans ce mémoire ouvre la voie à l'ajout de zéros de transmission supplémentaires aux structures développées ici.

Chapter 1

Introduction

1.1 Motivation

The recent emergence of advanced communication systems with a high degree of versatility has generated strong demand for novel devices with multi-functional performance. Compact, high performance, and lower cost RF/microwave devices are required today. Among these devices, band-pass filters, which allow signal pass-through in a specified band of frequencies, play an important role in RF/microwave communication systems. Filters are key components in radio-frequency transceivers in multiband operations. Their integration is challenging with regard to requirements. In new terminal generations providing several communication standards simultaneously, and especially in mobile terminals, embedded systems or satellites, the footprint of the filtering parts needs to be reduced in order to meet mass and volume requirements of the whole system. Thus, multiband band-pass filters (MBPFs) appear as an attractive solution to select multiple bands with a relatively compact circuit size.

Regarding this important issue, numerous researchers have suggested various synthesis techniques. This leads to numerous significant works created in recent years. Various approaches and technologies for constructing MBPFs of different degrees of complexity have been suggested with various numbers of bands and orders of the filter. However, there are still several obstacles to address when developing MBPFs with more than three pass-bands and high orders in order to fulfill rigorous specifications. In particular one needs to be paid attention to:

— Synthesis and realization of filters with controllable bandwidth exceeding three pass-bands.
— Easy-to-implement topological structure, universal realization method based on various technologies (microstrip, SIW, waveguide, etc.)
— Achievements of multiple pass-bands in a larger frequency range, that is to say, a larger center frequency ratio to be achieved between individual pass-band.

The aim of this thesis is to investigate and develop novel synthesis and designs methods for MBPFs. To address the above-mentioned issues, several chapters are proposed and quickly described in the next section.

1.2 Overview of the thesis

The work presented in this thesis is divided in six chapters, including introduction and conclusion, to which must be added an appendix. The details of each chapter will be given in the following:

Chapter 1 introduces the motivations and objectives in this thesis and presents an overview of the main chapters of this dissertation.

Chapter 2 has two main parts. The first part introduces the basic theories used in the construction of band-pass filters. It contains several essential concepts in filters, which will be used later in this dissertation, such as the definition of S-parameters for two-ports network, the definition of different types of transfer function for various low-pass filters, the frequency transformation for filters from low-pass prototype to high-pass, band-pass and band-stop domain, as well as the electric circuits for band-pass filters employing immittance inverters. The second part deals with the literature review of the existing approaches to design and realize multi-band filter responses in various ways. Four different methods are thus presented to realize MBPFs. In the last part of this chapter, the frequency transformation methods for dual-band and tri-band MBPFs will be introduced and discussed.

Chapter 3 is organized as follows: the theory of a generalized frequency transformation function is developed firstly. A rigorous mathematical analysis process is presented to obtain the generalized mapping function for an arbitrary number of pass-bands in a star-like topology. Several general formulas are obtained for the synthesis of MBPFs. Based on the proposed approach, three examples of MBPFs have been synthesized and experimentally validated with 3, 4 and 5 bands with non-coupled star-like topology, respectively. We also show the potential to extend this method to achieve more than quint-band with multi-layer configurations. In order to further reduce the footprint of the filter and demonstrate the different possibilities of this method, a tri-band and a quad-band MBPF based on coupled structures are developed validated through experiments. In the last part of this chapter, we demonstrate the universality of the frequency transformation method, discussing some other types of approximation function in Discussion. Finally, we show some advantages and disadvantages of the star-like topology.

Chapter 4 is organized in three parts. The first part proposes a new type of transformation function in an in-line topology. Two methods, one based on frequency mapping as previously and the other on a circuit approach, are used to obtain the circuit values. In a second part, four synthesis examples with Chebyshev responses are presented to validate both proposed synthesis methods. In order to illustrate the versatility of this design methodology, these examples are provided with different center frequencies, bandwidths and pass-band numbers. Very compact and good filters responses are achieved for all the fabricated circuits based on this in-line topology. The last part summarizes the advantages and disadvantages of in-line structures.

In chapter 5, we propose an optimization method to quickly design MBPFs based on as-

sociated band-stop resonators (ABSRs), aiming to overcome the shortcomings of the previous frequency transformation methods. We begin our research from the theoretical study of the behavior the ABSRs. 0n the basis of ABSRs, five examples with dual-band to sext-band band-pass filters were studied, simulated, implemented in microstrip technology and measured. In addition, we have made some comparisons between the high-order MBPFs based on ABSRs and recently published works. The advantages and disadvantages of this method are discussed in the last part of this chapter.

Chapter 6 concludes the whole thesis, summing up the contribution of this research and providing some prospects for future works.

An appendix section completes the thesis giving additional equation developments and results not presented in the main part of the dissertation in a sack of clarity.

Chapter 2

Literature review

2.1 Fundamental theory of filters

2.1.1 Fundamental theory of two-port network

In wireless communication systems such as mobile communications, satellite communications, radar, and remote sensing, microwave filters are essential components. They allow a perfect frequency selection and interference suppression and are therefore key components in microwave systems. With the advent of the 5G era, the fast-developing information markets put more stringent requirements on wireless communication systems and related equipment or components. In particular, filters must offer superior performance, compact size, low-cost, and need to be easy-to-integrate radio frequency components. In this chapter, we summarize the well-known and fundamental concepts of filter design principles which are relevant to the theory presented in this dissertation.

Fig. 2.1 shows the layout of a classical two-port network connected with a source associated to its internal impedance (Z_1) and a load impedance (Z_2), where V_1, V_2 and I_1, I_2 are the voltage and current variables at the ports 1 and 2, respectively. The terms a_m , b_m ($m \in [1; 2]$) are wave variables often used as auxiliary variables to deal more easily with transmission / reflection of energy between the two ports. The variables a_m indicate incident waves and b_m indicate reflected waves at port m, respectively. They both can be expressed in terms of voltages and currents as follows:

$$a_m = \frac{1}{2}\left(\frac{V_m}{\sqrt{Z_m}} + \sqrt{Z_m} I_m\right) \tag{2.1}$$

$$b_m = \frac{1}{2}\left(\frac{V_m}{\sqrt{Z_m}} - \sqrt{Z_m} I_m\right) \tag{2.2}$$

For filter synthesis, we mainly focus on the scattering parameters of the two-port network, defined in terms of the wave variables as:

$$S_{11} = \frac{b_1}{a_1} \mid_{a_2=0} \tag{2.3}$$

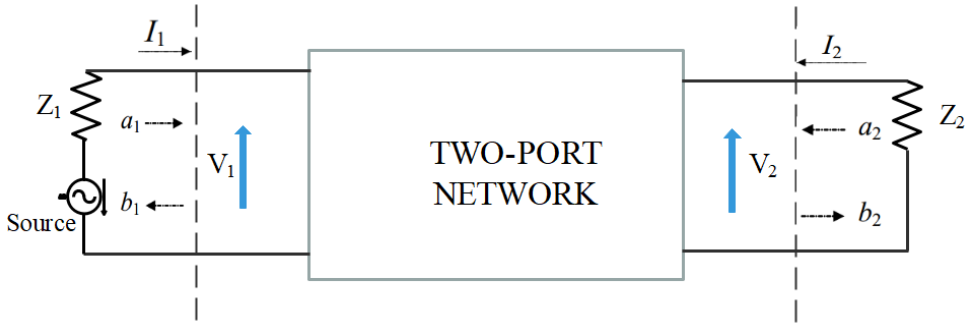

Figure 2.1 – Two-port network showing network variables.

$$S_{12} = \frac{b_1}{a_2} \mid_{a_1=0} \tag{2.4}$$

$$S_{21} = \frac{b_2}{a_1} \mid_{a_2=0} \tag{2.5}$$

$$S_{22} = \frac{b_2}{a_2} \mid_{a_1=0} \tag{2.6}$$

The parameters S_{11} and S_{22} are also called reflection coefficients, whereas S_{12} and S_{21} are transmission coefficients. These are the parameters that can be directly measured at microwave frequencies using vector network analysers. In a common case, S-parameters are complex and they are usually expressed in terms of amplitude and phase. Amplitudes of S-parameters are often used in the logarithmic scale for convenience:

$$L_A = 20 \log |S_{21}| \tag{2.7}$$

$$L_R = 20 \log |S_{11}| \tag{2.8}$$

where L_A denotes the insertion loss between the two ports, and L_R represents the return loss. It is often required to convert S parameter to other types of matrices describing m port systems such as impedance and admittance networks. The relationships between any types of parameters are well-known [20, 21].

A classical and theoretical way to design filters starts with the definition of a normalized low-pass prototype [21]. This definition is made through a transfer function which will give the in-band and out-of-band behaviors of this low-pass prototype [21] before its transformation into a high-pass, band-pass or band-stop denormalized filter. The transfer function of a two-port filter network is a mathematical description of S_{21}. Typically, the transfer function for a lossless

passive filter network is defined as:

$$|S_{21}(j\Omega)|^2 = \frac{1}{1+\epsilon^2 F_n^2(\Omega)} \tag{2.9}$$

where ϵ is a constant defining the in-band ripple, $F_n(\Omega)$ represents a characteristic function, and Ω is a normalized frequency variable in low-pass prototype domain. It has a upper cutoff frequency at $\Omega = 1$ and a lower cut-off frequency at $\Omega = -1$.

$F_n(\Omega)$ represents the approximation function. The filter synthesis consists in choosing the best approximation function according to the filter specifications (in-band and out-band requirements). The most classical ones are Butterworth (maximally flat), Chebyshev and elliptic functions. A Butterworth filter exhibits monotonically rising attenuation. In the near-out-of-band region, the Butterworth filter provides less attenuation than an equivalent Chebyshev or elliptic filter [19]. In practical applications, we prefer the latter two types of filters. In the following, we will give more details about the latter ones.

The Chebyshev response exhibits an equal ripple pass-band and a maximally flat stop-band. The amplitude squared transfer function that describes this type of response is:

$$|S_{21}(j\Omega)| = \frac{1}{1+\epsilon^2 T_n^2(\Omega)} \tag{2.10}$$

where the ripple constant ϵ is related to a given pass-band ripple $L_A r$ (expressed in dB) by:

$$\epsilon = \sqrt{10^{\frac{L_A r}{10}} - 1} \tag{2.11}$$

$T_n(\Omega)$ is a Chebyshev function of the first kind of order n, which is defined as:

$$T_n(\Omega) = \begin{cases} \cos(n\cos^{-1}) & |\Omega| \leq 1 \\ \cosh(n\cosh^{-1}) & |\Omega| \geq 1 \end{cases} \tag{2.12}$$

The elliptic function response provides equal-ripple in both pass-band and stop-band. Its transfer function for this type of response is:

$$|S_{21}(j\Omega)| = \frac{1}{1+\epsilon^2 E_n^2(\Omega)} \tag{2.13}$$

For n is even,

$$E_n(\Omega_i) = M\frac{\prod_{i=1}^{n/2}(\Omega_i^2 - \Omega^2)}{\prod_{i=1}^{n/2}(\Omega_s^2/\Omega_i^2 - \Omega^2)} \tag{2.14}$$

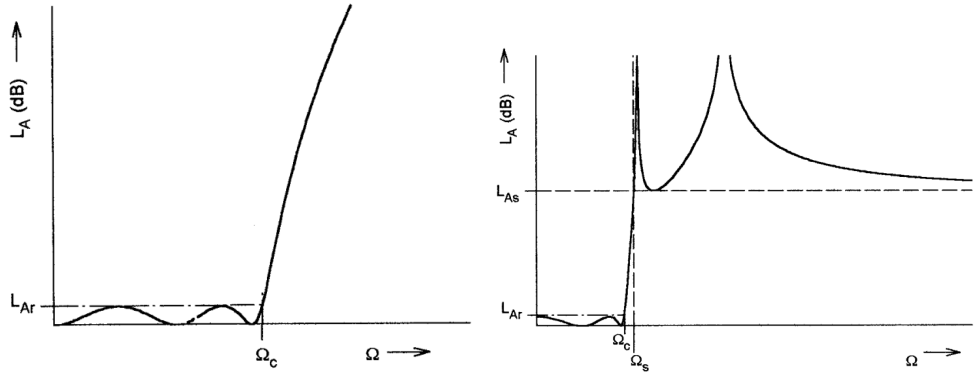

(a) (b) Elliptic function low-pass response

Figure 2.2 – The low-pass fiter responses. (a) Chebyshev low-pass response. (b)Elliptic function low-pass response.

For $n \geq 3$ is odd,

$$E_n(\Omega_i) = N \frac{\Omega \prod_{i=1}^{(n-1)/2} (\Omega_i^2 - \Omega^2)}{\prod_{i=1}^{(n-1)/2} (\Omega_s^2/\Omega_i^2 - \Omega^2)} \tag{2.15}$$

where $\Omega_i (0 < \Omega_i < 1)$ and $\Omega_s > 1$ represent the in-band normalized frequencies and the out-of-band ones. The terms M and N are constants [21]. $E_n(\Omega_i)$ oscillates between ± 1 for $|\Omega_i| \leq 1$, and $E_n(\Omega_i = \pm 1) = 1$.

A key aspect of filter design is to build the relationship between theoretical and mathematical concepts and the actual or equivalent circuit elements for its fabrication. The characteristic polynomials described above for Chebyshev and elliptic lossless low-pass prototype filters are based on lumped circuit elements. The circuit configuration of such a low-pass prototype filter corresponds to a ladder network [21, 19]. The circuit model of the prototype filter provides the link to the physical realization of the filter networks.

The determination of the element values can be obtained from the characteristic polynomial of a desired low-pass prototype filter. In [19] chapters $6 - 8$, the synthesis procedures are presented to determine the element values from characteristic polynomials for any class of filter function like Chebyshev filters or elliptic filters. The prototype ladder-type networks are shown in Fig. 2.3. There are two types of low-pass prototypes, both can have even and odd number of orders. The first one starts with shunt capacitance, and the second starts with inductance. These two circuits with the same order can have same responses.

The two types of low-pass prototype ladder-type networks introduced above, exhibit normalized element values with regard to the source and load impedance/conductance [19]. In practice high-pass, band-pass or band stop filters at any operating frequency may be designed from low-pass filters. Filters with required termination values and cut-off or center frequencies could be derived by impedance and frequency transformation from low-pass prototype filter.

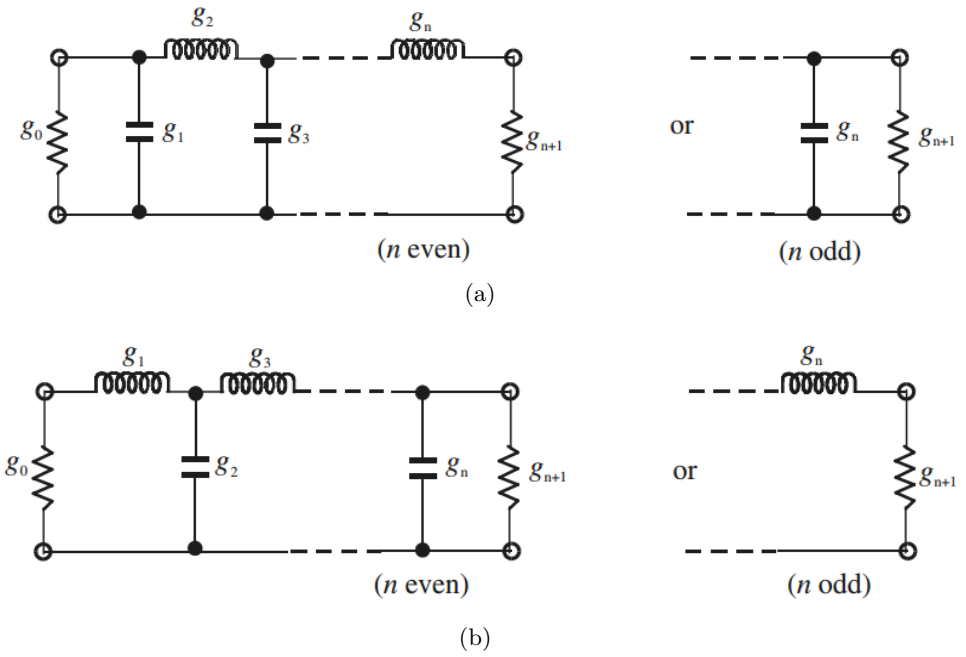

Figure 2.3 – Ladder-type low-pass prototype starting with capacitance (a) or with inductance (b).

The impedance transformation can be done by scaling the normalized generator impedance or conductance. To do so, a scaling factor S_γ is defined as:

$$S_\gamma = \begin{cases} Z_0/g_0 \\ g_{00}/Y_0 \end{cases} \tag{2.16}$$

Here Z_0 and Y_0 are the source (load) impedance or admittance. The scaling factor in the first equation holds for g_0 defined as a resistance whereas the second holds for g_{00} defined as a conductance. Using the scaling factor in (2.16) the inductance L will be scaled as $S_\gamma L$ and the conductance C will be scaled as C/S_γ. The classical low-pass Chebychev circuit in low-pass domain and the lumped element ladder network of low-pass prototype transformed network are presented in Fig. 2.4(a) and Fig. 2.4(b).

2.1.2 Low-pass to other types filters transformation

To transform a low-pass prototype filter with unity cut-off frequency to a low-pass filter with cut-off frequency ω_c, the frequency variable has to be scaled by a factor of $1/\omega_c$, or the cut-off frequency 1 has to be mapped to a realistic cut-off frequency ω_c. The transformation procedure

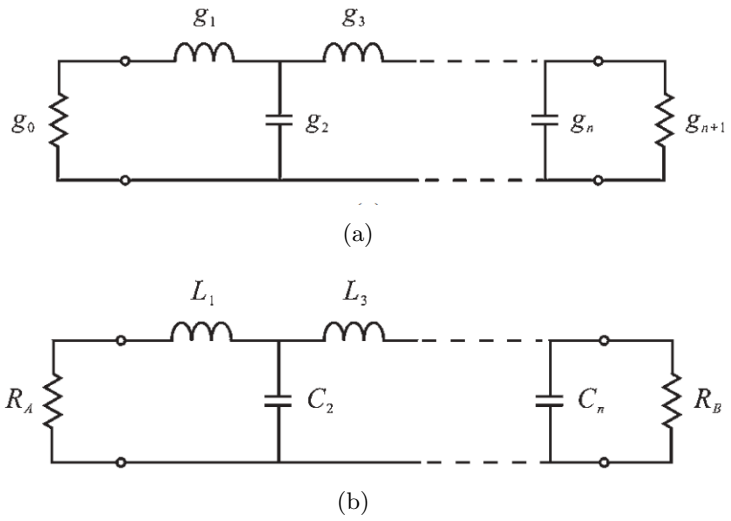

Figure 2.4 – Lumped element ladder network (a) of low-pass prototype network and transformed network (b).

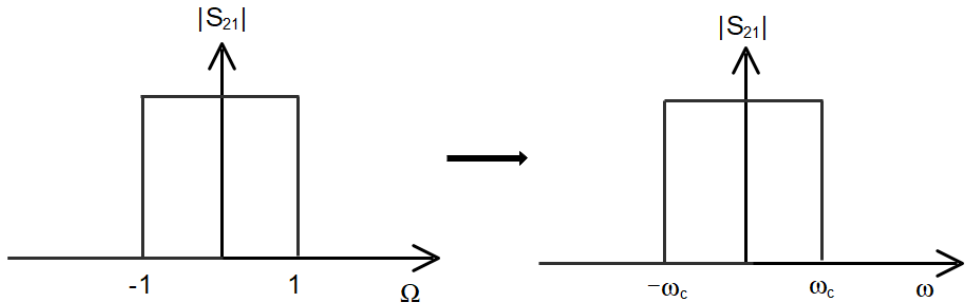

Figure 2.5 – Low-pass with unity cut-off frequency to a low-pass filter with real cut-off frequency.

is achieved by replacing ω_c by ω/ω_c, which is:

$$\Omega \rightarrow \frac{\omega}{\omega_c} \tag{2.17}$$

$$\begin{aligned} L_n &= \frac{S_\gamma g_n}{\omega_c} \\ C_n &= \frac{g_n}{S_\gamma \omega_c} \end{aligned} \tag{2.18}$$

and all capacitance or inductance values should also be scaled as shown in (2.18). The transformation schematic is shown in Fig. 2.5

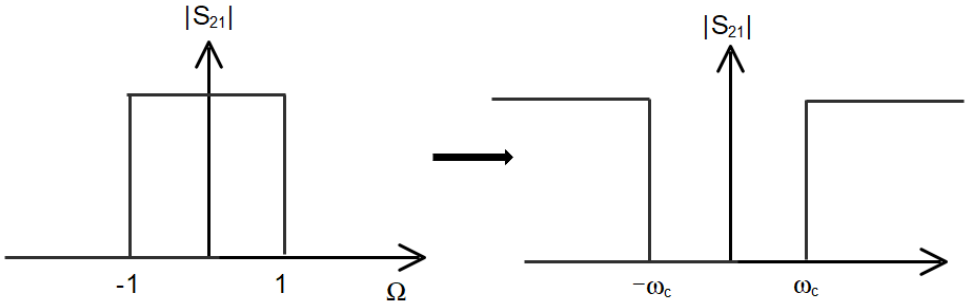

Figure 2.6 – Low-pass with unity cut-off frequency to a high-pass filter with real cut-off frequency.

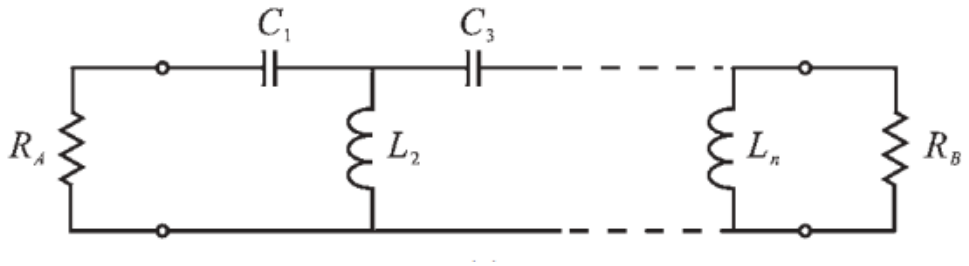

Figure 2.7 – Low-pass to high-pass transformation.

For a low-pass to high-pass frequency transformation, the transformation is as follows:

$$\Omega \rightarrow -\frac{\omega_c}{\omega} \tag{2.19}$$

$$\begin{aligned} L_n &= \frac{S_\gamma}{\omega_c g_n} \\ C_n &= \frac{1}{S_\gamma \omega_c g_n} \end{aligned} \tag{2.20}$$

The transformed circuit is shown in Fig. 2.7.

For a low-pass to band-pass frequency transformation, the principle remains identical. However, instead of using a single cut-off frequency for low-pass to high-pass transformation, two different cut-off frequencies are imposed, ω_1 and ω_2, to define the lower and upper pass-band edges. Then, the transformation is performed by replacing Ω with the following expression:

$$\Omega \rightarrow \frac{1}{FBW}\left(\frac{\omega}{\omega_c} - \frac{\omega_c}{\omega}\right) \tag{2.21}$$

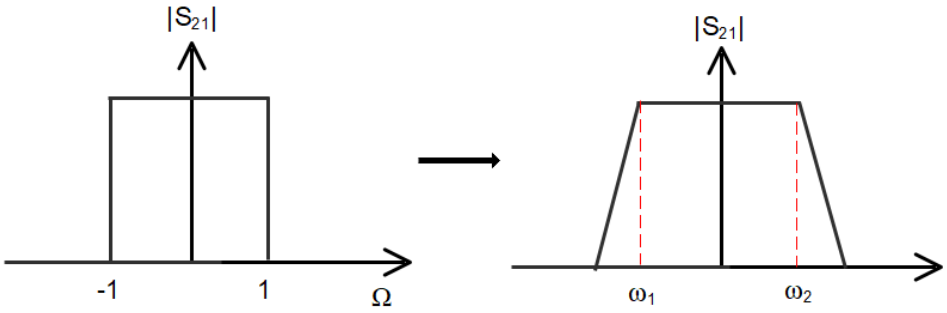

Figure 2.8 – Low-pass to band-pass transformation-circuits transform.

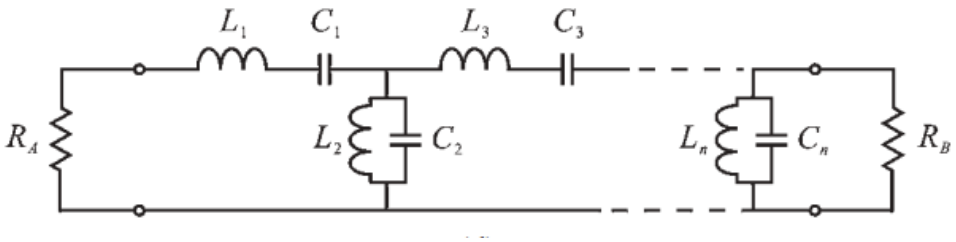

Figure 2.9 – Low-pass to band-pass transformation-circuit transform.

where FBW stands for fractional bandwidth, and is defined as

$$FBW = \frac{\omega_2 - \omega_1}{\omega_c} \tag{2.22}$$

In this equation, ω_c represents the center frequency of the transformed band-pass filter. It can be written as $\omega_c{=}\sqrt{\omega_1\omega_2}$. The series elements in the low-pass prototype filter are transformed to series resonant circuits. At the same time, the shunt elements are converted to parallel resonant circuits. Both types of series and parallel resonant circuits have the same resonant frequency ω_c. The element values in the series resonators can be determined as:

$$\begin{aligned} L_{sn} &= \frac{g_n S_\gamma}{FBW\omega_c} \\ C_{sn} &= \frac{FBW}{S_\gamma \omega_c g_n} \end{aligned} \tag{2.23}$$

and the element values in the shunt resonators can also be determined as:

$$\begin{aligned} L_{pn} &= \frac{FBW S_\gamma}{g_n \omega_c} \\ C_{pn} &= \frac{g_n}{FBW S_\gamma \omega_c} \end{aligned} \tag{2.24}$$

Fig. 2.8 shows the schematic of low-pass to band-pass transformation and Fig. 2.9 presents the

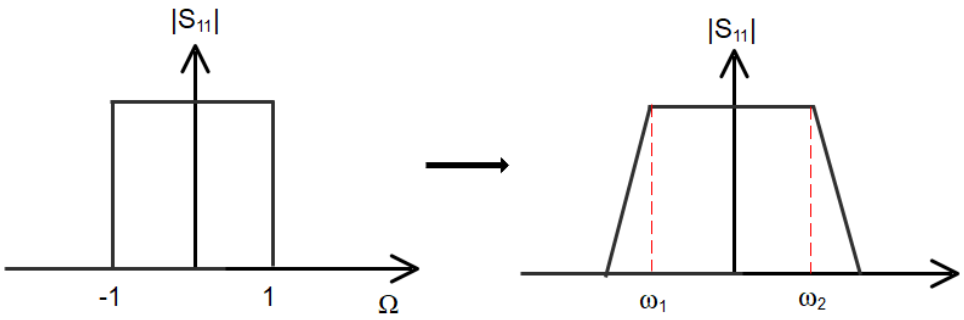

Figure 2.10 – Low-pass to band-stop transformation.

associated circuit transformation.

For a low-pass to band-stop frequency transformation, a similar principle applies. The two frequencies ω_1 and ω_2 are now used to denote the lower and upper stop-band edges. The transformation is done by replacing Ω such as:

$$\Omega \rightarrow -\frac{1}{FBW}\left(\frac{\omega}{\omega_c}-\frac{\omega_c}{\omega}\right)^{-1} \tag{2.25}$$

In this context, FBW stands for the fractional bandwidth of the stop-band, and remains defined as

$$FBW = \frac{\omega_2 - \omega_1}{\omega_c} \tag{2.26}$$

where ω_c corresponds to the center frequency of the transformed band-stop filter. It also can be expressed as $\omega_c{=}\sqrt{\omega_1\omega_2}$. Under this transformation, a series inductive element in the low-pass prototype is transformed to a parallel resonant circuit, which is opposite to that of the low-pass to band-pass transformation:

$$\begin{aligned} L_{sn} &= \frac{FBW\, g_n S_\gamma}{\omega_c} \\ C_{sn} &= \frac{1}{FBW\, S_\gamma \omega_c g_n} \end{aligned} \tag{2.27}$$

Reciprocally, a capacitance shunt element is transformed into a series L-C circuit with the following values:

$$\begin{aligned} L_{pn} &= \frac{S_\gamma}{FBW\, g_n \omega_c} \\ C_{pn} &= \frac{FBW\, g_n}{S_\gamma \omega_c} \end{aligned} \tag{2.28}$$

The transformed schematic and the transformed circuit are shown in Fig. 2.10 and Fig. 2.11,

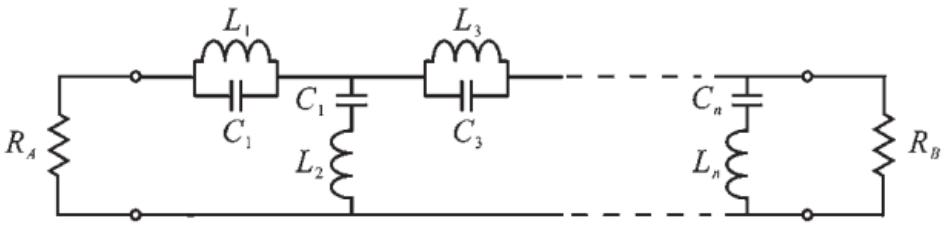

Figure 2.11 – Low-pass to band-stop transformation-circuit transform.

respectively.

2.1.3 Immittance inverters

There are two types of immittance inverter, which are classified as impedance inverter and admittance inverter. An impedance inverter is used to convert a shunt element in a series one and an admittance one to convert a series element to a shunt one. Such a transformation creates a phase shift of $\pm 90^0$ according to topology. The most classical inverter in microwave technology consists of a quarter-wavelength line. An ideal impedance inverter can be regarded as a quarter-wavelength impedance transformer with a normalized characteristic impedance K at all working frequencies. Fig. 2.12 (a) shows a two-port impedance inverter with one port terminated by a load R_b. The input impedance seen from the other port is:

$$Z_a = \frac{K^2}{R_b} \tag{2.29}$$

In a similar way, the admittance inverter can also be regarded as a quarter-wavelength transformer with normalized characteristic admittance of J at all frequencies. As shown in Fig. 2.12 (b), given the load admittance G_b at one port, the input admittance Y_a at the other port writes:

$$Y_a = \frac{J^2}{G_b} \tag{2.30}$$

The immittance inverter is useful in converting a series capacitor/inductor to a shunt inductor/capacitor with a phase shift of $\pm 90^0$ or an odd multiple there of and vice versa. This is its most attractive feature. As illustrated in Fig. 2.9, the ladder network of a band-pass prototype filter is composed of series inductances in cascade with shunt capacitances in an alternate arrangement. Making use of the immittance inverters, the low-pass prototype can be converted to a filter network shown in Fig. 2.13. The converted network consists of either series inductors or shunt capacitors that are connected via immittance inverters. Since the immittance inverters can shift the impedance or admittance levels depending on the values of K (Fig. 2.13(a)) or J parameters (Fig. 2.13(b)), the new element values L_{ai} and C_{ai}, termination resistance R_A

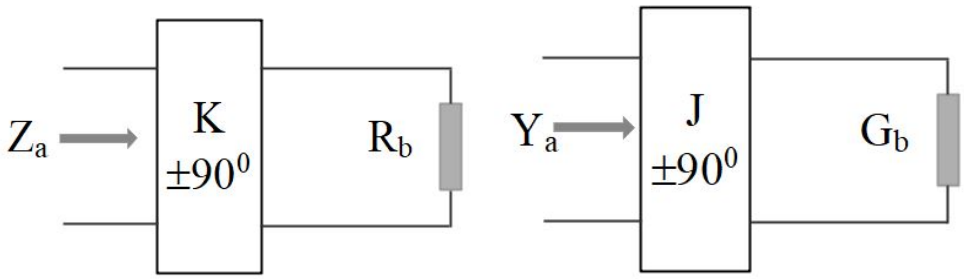

(a) (b)

Figure 2.12 – The schematic of immittance inverters : (a) Impedance inverter, (b) Admittance inverter.

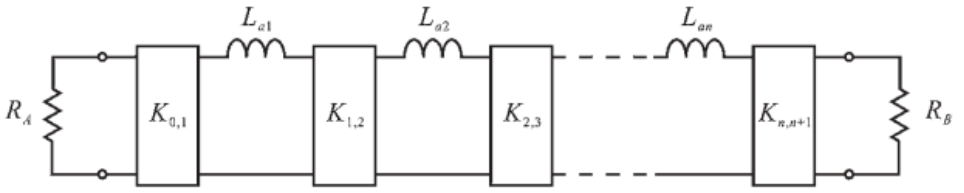

(a)

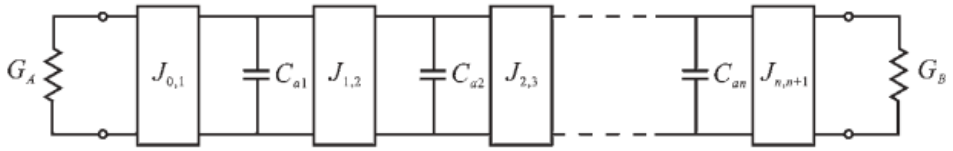

(b)

Figure 2.13 – Low-pass prototype filter with (a) impedance inverter, (b) admittance inverter.

and R_B, as well as the termination conductance G_A and G_B, can be arbitrarily chosen. The g_i parameters are the element values that are derived for a n-order low-pass prototype filter, the values can be referenced in [20]. The design equations for low-pass filters can be expressed as:

$$K_{0,1} = \sqrt{\frac{R_A L_{a1}}{g_0 g_1}} \tag{2.31}$$

$$K_{k,k+1}|_{k=1 \text{ to } n-1} = \sqrt{\frac{L_{ak} L_{a(k+1)}}{g_k g_{k+1}}} \tag{2.32}$$

$$K_{n,n+1} = \sqrt{\frac{L_{an} R_B}{g_n g_{n+1}}} \tag{2.33}$$

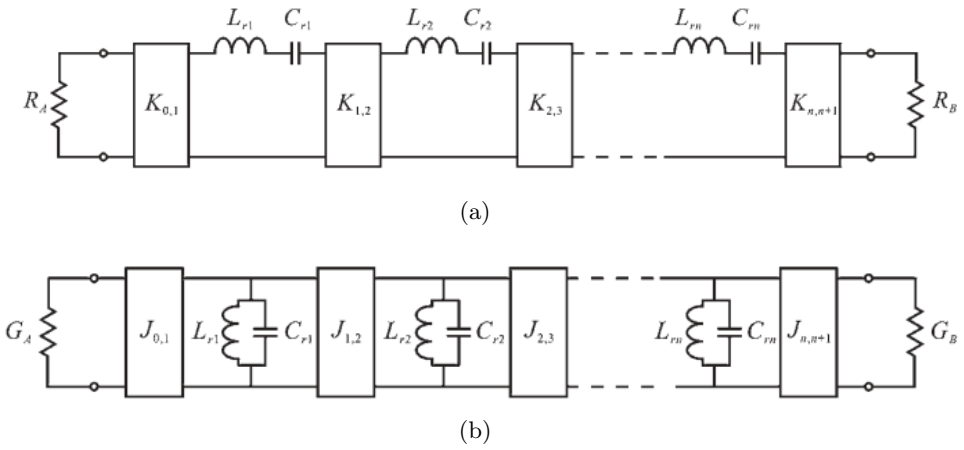

Figure 2.14 – Band-pass prototype filter with (a) impedance inverter, (b) admittance inverter.

$$J_{0,1} = \sqrt{\frac{G_A C_{a1}}{g_0 g_1}} \tag{2.34}$$

$$J_{k,k+1}|_{k=1 \text{ to } n-1} = \sqrt{\frac{C_{ak} C_{a(k+1)}}{g_k g_{k+1}}} \tag{2.35}$$

$$J_{n,n+1} = \sqrt{\frac{C_{an} G_B}{g_n g_{n+1}}} \tag{2.36}$$

With a similar conversion procedure, the band-pass prototype can be converted to a network that consists of only shunt elements connected via admittance inverters, as shown in Fig. 2.14. The transformed bandpass filter and its dual with immittance inverter K (Fig. 2.14(a)) or J (Fig. 2.14(b)), are shown in Fig. 2.14. The design equations for band-pass filters can be expressed as:

$$K_{0,1} = \sqrt{\frac{R_A FBW \omega_0 L_{r1}}{g_0 g_1}} \tag{2.37}$$

$$K_{k,k+1}|_{k=1 \text{ to } n-1} = FBW\omega_0 \sqrt{\frac{L_{rk} L_{r(k+1)}}{g_k g_{k+1}}} \tag{2.38}$$

$$K_{n,n+1} = \sqrt{\frac{FBW\omega_0 L_m R_B}{g_n g_{n+1}}} \tag{2.39}$$

$$J_{0,1} = \sqrt{\frac{G_A FBW \omega_0 C_{r1}}{g_0 g_1}} \tag{2.40}$$

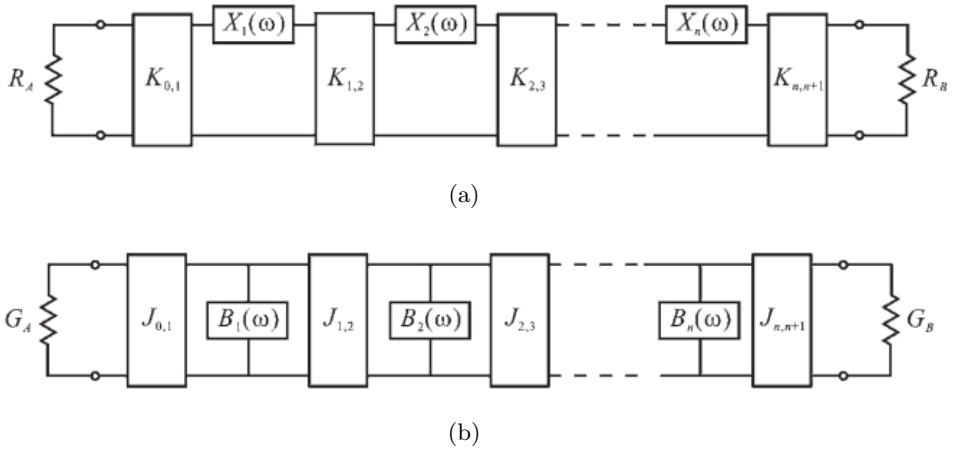

Figure 2.15 – Generalized bandpass filters with (a) impedance inverter, (b) admittance inverter.

$$J_{k,k+1}|_{k=1 \text{ to } n-1} = FBW\omega_0\sqrt{\frac{C_{rk}C_{r(k+1)}}{g_k g_{k+1}}} \tag{2.41}$$

$$J_{n,n+1} = \sqrt{\frac{FBW\omega_0 C_{rn}G_B}{g_n g_{n+1}}} \tag{2.42}$$

Where FBW is the fraction bandwidth , ω is the center frequency of the band-pass filter. The values of L_{rk} and C_{rk}, termination resistance R_A and R_B, as well as the termination conductance G_A and G_B, can also be arbitrarily chosen as for the low-pass case.

The presented two generalized networks are composed of series or shunt lumped resonators and impedance or admittance inverters. In practice, these series or shunt LC resonators can be constructed in various forms, such as transmission line, waveguide or SIW resonators. In this context, resonant frequency ω_0 and slope parameter are usually used to characterize such a resonator regardless of their types. For a series resonator with reactance $X_(\omega)$, the slope parameter is defined as:

$$x = \frac{\omega_0}{2}\frac{dX(\omega)}{d\omega}\bigg|_{\omega=\omega_0} \tag{2.43}$$

For a shunt resonator with susceptance $B_(\omega)$, the susceptance slope parameter is:

$$b = \frac{\omega_0}{2}\frac{dB(\omega)}{d\omega}\bigg|_{\omega=\omega_0} \tag{2.44}$$

$$K_{0,1} = \sqrt{\frac{R_A FBW x_1}{g_0 g_1}} \tag{2.45}$$

$$K_{k,k+1}|_{k=1 \text{ to } n-1} = FBW\sqrt{\frac{x_k x_{k+1}}{g_k g_{k+1}}} \tag{2.46}$$

$$K_{n,n+1} = \sqrt{\frac{FBW x_n R_B}{g_n g_{n+1}}} \tag{2.47}$$

$$J_{0,1} = \sqrt{\frac{G_A FBW b_1}{g_0 g_1}} \tag{2.48}$$

$$J_{k,k+1}|_{k=1 \text{ to } n-1} = FBW\sqrt{\frac{b_k b_{k+1}}{g_k g_{k+1}}} \tag{2.49}$$

$$J_{n,n+1} = \sqrt{\frac{FBW b_n G_B}{g_n g_{n+1}}} \tag{2.50}$$

By generalizing the series and shunt resonators with the specified reactance and susceptance, we can build up a generalized band-pass filter network as shown in Fig. 2.15. The introduction of this network is quiet essential. In the next chapter we make use of a similar method for the synthesis and the design of multiband band-pass filters with star-like topology by frequency transformation method.

2.2 Overview of the topologies and technology for the design of multiband band-pass filters

With the recent rapid development of communication systems, multiband band-pass filters (MBPFs) can support several frequency bands with high-performance and compact size [22], combining single-band filters in a single circuit. In satellite communication systems [1], a multiband filter can be used to transmit several non-contiguous channels to the same geographic region through one beam for high throughput satellite (HTS) system. In this case, only a single high-power amplifier is needed, which simplifies system architecture and reduces DC power consumption. Moreover, MBPFs can work with low noise amplifiers and power amplifiers, receiving and transmitting signals of multiple wireless through a single antenna. The simplification enables designing transponder with an increased number of channels, thus improving the system's efficiency.

The dual-band filter was proposed more than two decades ago [2]. Since then, researchers have proposed various synthesis methods, topologies and technologies to develop dual-band filters. Nevertheless, MBPFs with three or more bands present greater challenges in terms of filtering performance and compactness. This lead to a growing interest in MBPFs in the recent

years. Typically, there are four different ways to design multiband band-pass filters (MBPFs) with different technologies [3].

2.2.1 Design of multiband band-pass filters by connecting band-pass and band-stop filters

A first and simple method for multiband filter design consists in introducing TZs into a single-band filter. One of the first proposed dual-band filters by this method was presented in [4]. It was realized by the series association of a band-pass filter and a band-stop filter. The band-pass and band-stop filters were synthesized and designed separately and optimized to achieve optimum filtering performances. The proposed dual-band filter is presented in Fig. 2.16. The filter is composed of of a band-pass filter on its left part in series with a band-stop filter on its right part. A tri-band filter based on this approach was proposed in [5] using dual- behavior resonator (DBR). This design is shown in Fig. 2.17. The second order filters are realized by cascading two same sections, each one has three open shunt stubs. The proposed structure consists of only band-stop resonators that can create TZs at specified frequencies and pass-bands between two consecutive TZs. By adjusting the length and width of the DBR, the required TZs and slope parameters can be realized. This type of filter seems to have arbitrary pass-bands responses. However, the absence of the slope parameters in the synthesis of equations makes the realization of high-order DBR MBPFs difficult to achieve . Another tri-band configuration was proposed in [6]. In this paper, two same units (a quarter-wavelength transmission line loaded with shunt-open and short-circuited stepped impedance resonators (SIR)) connected with a quarter wavelength transmission line as shown in Fig. 2.18 were used to achieve tri-band responses. Nevertheless, the pass-band region is not easily controlled due to the presence of harmonic frequencies. This structure provides three TZs, two of which are realized by two harmonics frequencies.

2.2.2 Design of multiband band-pass filters by connecting individual band-pass filters

The second method of MBPF design consists in combining several single-band or dual-band filters to obtain a response with two or more bands. A simple dual-band microstrip filter using folded open-loop ring resonators (OLRRs) was first presented in [9] by the combination of two individual filters as shown in Fig. 2.19. Both magnetic and electric coupling structures were implemented to provide high performance pass-band response. The first and second bands of the designed dual-band filter can be easily and accurately shifted to the desired frequency by adjusting the physical dimensions of OLRRs. A planar dual-band band-pass filter based on a novel feed scheme was presented in [10]. The proposed filter employed two sets of resonators operating at several frequencies to generate two pass-bands (resonator 1 and resonator 4 resonating at the first pass-band; resonator 2 and resonator 3 resonating at the second pass-band as

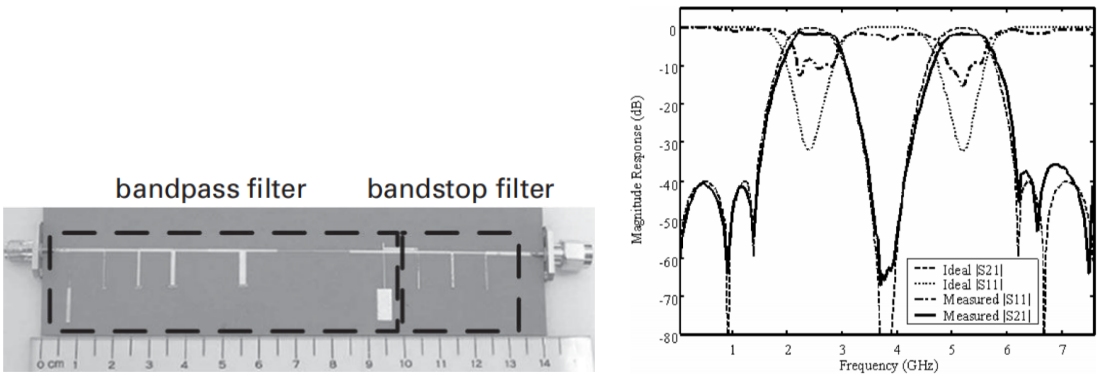

(a) (b)

Figure 2.16 – Schematic view (a) and frequency responses (b) of the dual-band filter proposed in [4].

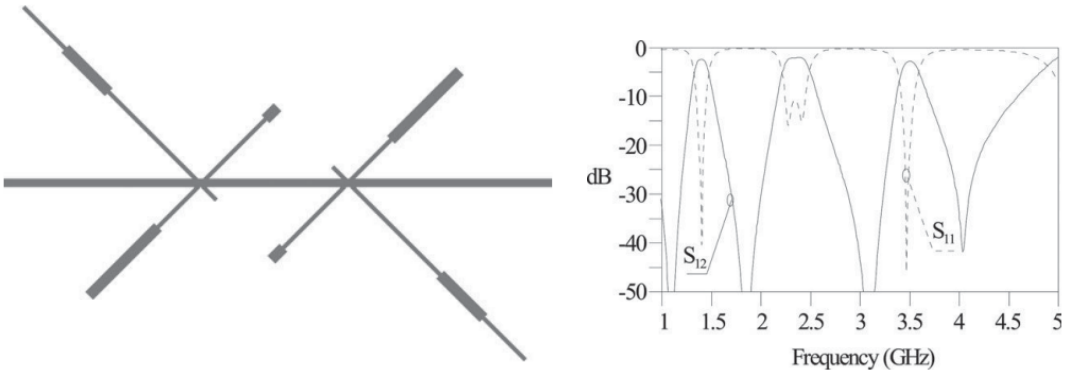

(a) (b)

Figure 2.17 – Schematic view (a) and frequency responses (b) of the dual-band filter proposed in [5].

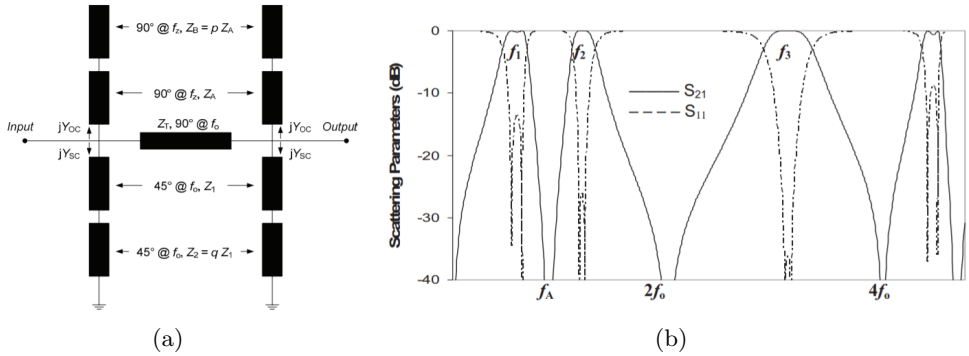

(a) (b)

Figure 2.18 – Schematic view (a) and frequency responses (b) of the tri-band filter proposed in [6].

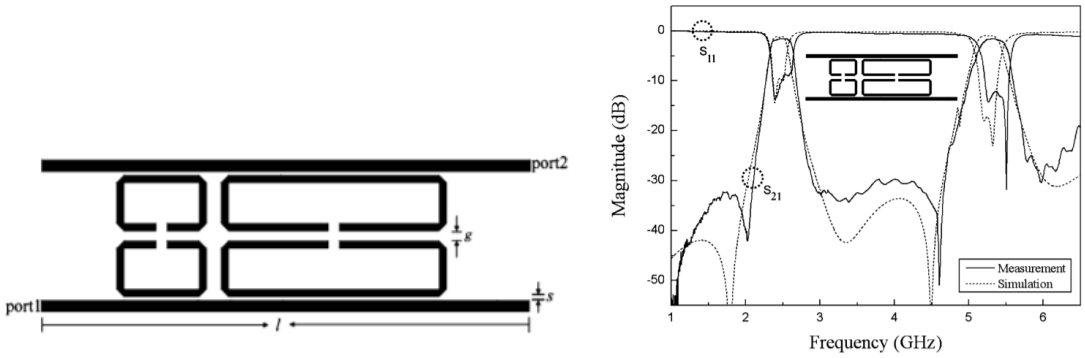

(a) (b)

Figure 2.19 – Schematic view (a) and frequency responses (b) of the dual-band filter proposed in [9].

shown in 2.20(a)). The different feeding scheme provided sufficient degrees of freedom to control the center frequencies and bandwidth of the two pass-bands. The configuration, simulation and measurement are shown in 2.20(a) and 2.20(b), respectively.

2.2.3 Design of multiband band-pass filters by employing multi-mode resonators

The third method to achieve MBPFs relies on multi-mode resonators (MMRs). MMRs are structures that support several different resonant modes whose resonant frequencies are not harmonically related. MMRs can offer more design freedom than single-mode resonators. Also, MMRs support several modes with a single resonator, which is a very attractive feature. It is, therefore, a promising platform for small filtering devices.

For planar microstrip technology, the main types of MMRs are resonators with SIRs and stub-loaded resonators implemented in microstrip technology [11, 23, 12, 24, 25, 26, 27, 13]. In [11], a dual-mode dual-band band-pass filter with two transmission poles in both pass-bands using a single ring resonator was proposed. Two feeding ports are placed along the ring resonator and coupled with the ring via parallel-coupled lines (shown in 2.21(a)), leading to synchronous excitation of two transmission poles in the two pass-bands. Fig. 2.21(a) shows the schematic of the proposed dual-mode dual-band band-pass filter using a single uniform ring resonator. In a similar way, a class of tri-band BPFs with two reflection zeros in each pass-band was proposed in [23] using three pairs of degenerated modes in a ring resonator. However, the band-to-band isolation is not so good. To improve the selectivity of such kinds of filters, Sun [12] proposed a simple microstrip ring-resonator for a novel design of dual-band dual-mode band-pass filter. Good isolation and upper stop-band performance are obtained with the two first-order degenerate modes. Apart from the SIRs, the stub-loaded resonators (SLRs) could be a good candidate to construct MBPFs. Numerous structures have been proposed with a different

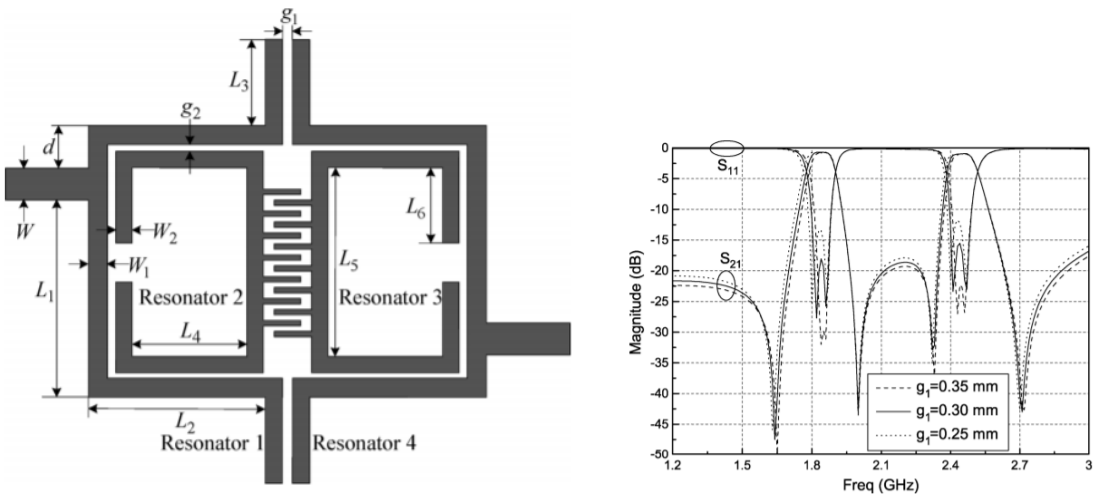

(a) (b)

Figure 2.20 – Schematic view (a) and frequency responses (b) of the dual-band filter proposed in [10].

combination of resonant frequencies [25, 26, 27, 13] for dual-, tri-, or quad-band MBPFs. SLRs structures enable the design of filters with good performance and small dimensions. They have overall similar behavior as SIRs. The difference between SIR and SLRs is that some modes can be controlled independently from the other by a change in the stub length for SLRs structures, providing more flexibility for designing MBPFs.

For multi-mode waveguide resonators, the dual-mode and tri-mode resonators are often used to design MBPFs. In [14, 28], the proposed operating modes in the elliptical cavity were based on TE_{111} mode degeneracy, similar to the cylindrical cavity. The dual resonators are tuned at independent frequencies by the cavity diameter difference along the two elliptical axes. The two orthogonally polarized modes are intrinsically isolated and can be designed to carry two pass-band signals. An example of eight-order dual-band filters with 16 poles based on this kind of dual-mode resonator is shown in 2.22(a). The response of the filter is presented in Fig. 2.22(b). An elliptical cavity triple-mode was also employed to realize a tri-band performance [15]. The operating modes in the elliptical cavity are the degeneration of $TE111_V$, $TE111_H$, and TM_{010} mode. The filter structure is shown in Fig. 2.23(a) with three tri-mode resonators. Fig. 2.23(b) shows the tuned near-band responses of the manufactured filter compared with the simulation responses. For this case, the spurious mode at a higher frequency is relatively close to the pass-band, as shown in Fig. 2.23(c). Unfortunately, the spurious-free window is difficult to expand due to the intrinsic mode distribution of the elliptical cavity.

Substrate-integrated waveguide (SIW) is an up-and-coming platform for designing MBPFs. For MMRs, typically, there are three methods to obtain the multiband responses using SIW

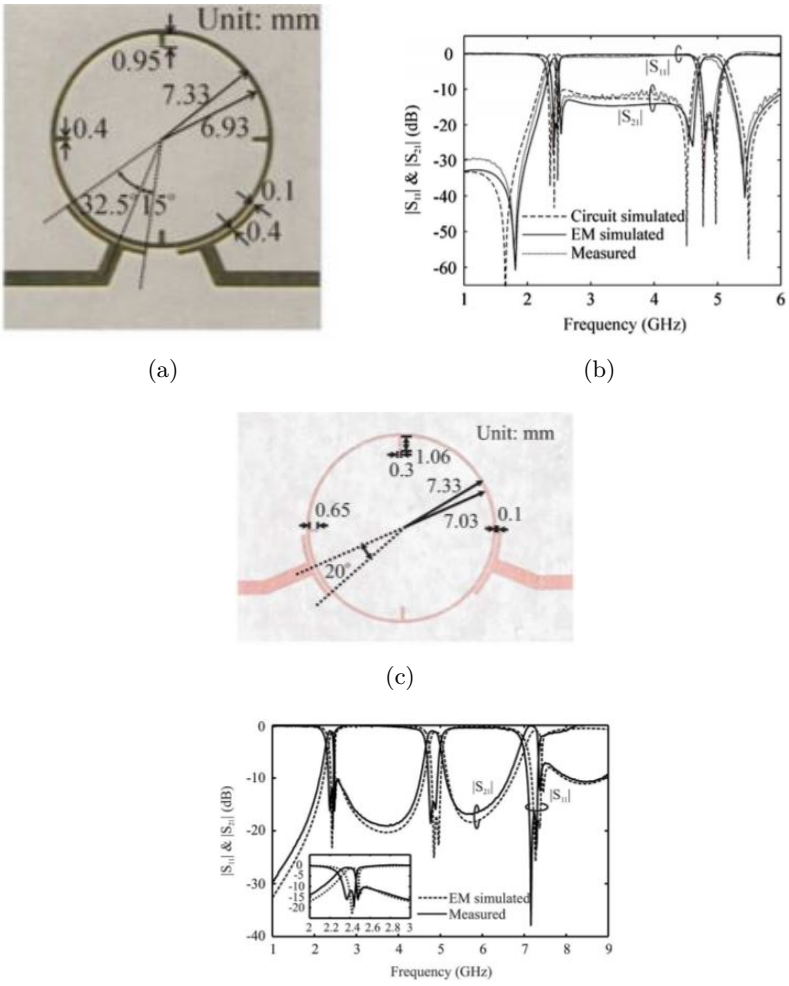

Figure 2.21 – Schematic view (a) and frequency responses (b) of the ring filter proposed dual-band filter in[11]; schematic view (c) and frequency responses (d) of the tri-band filter proposed in[23].

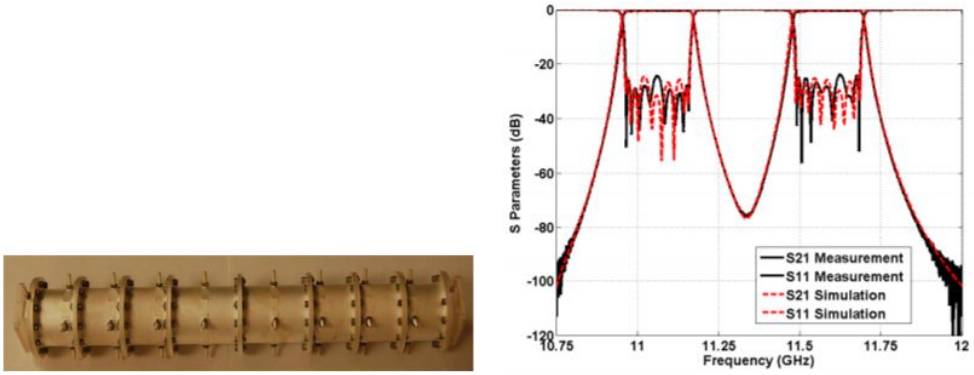

(a) (b)

Figure 2.22 – Figure (a): Photograph of the proposed filter and (b) filter's responses [14].

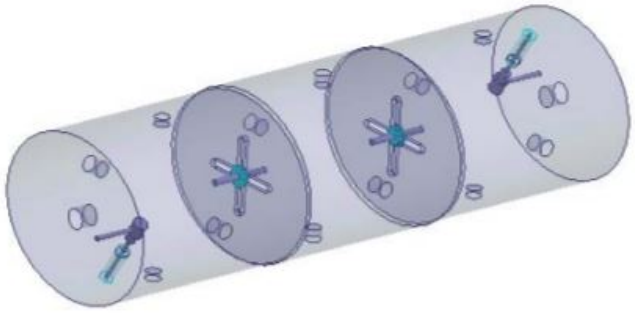

(a)

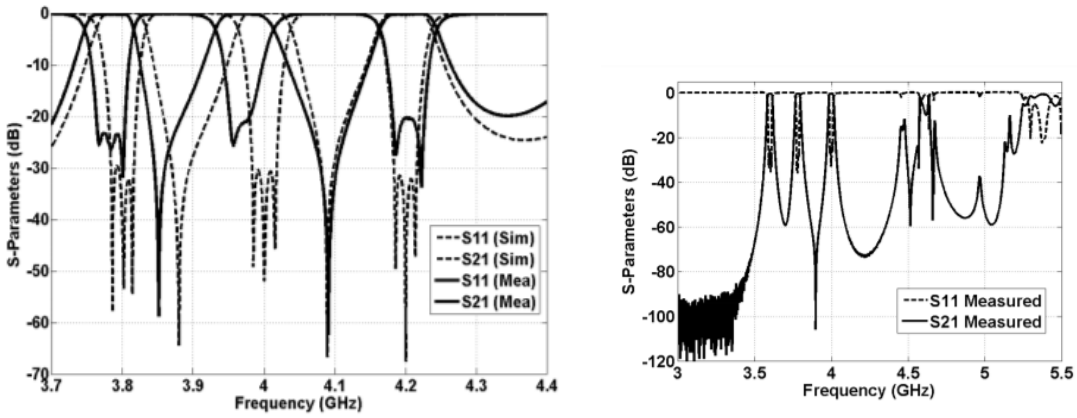

(b) (c)

Figure 2.23 – Layout of elliptical cavity triple-band filter (a); responses of the proposed triple-mode waveguide filter (b). Measurement of elliptical cavity triple-band filter [15]. The harmonic resonant frequencies of elliptical cavity triple-band filter[15] (c).

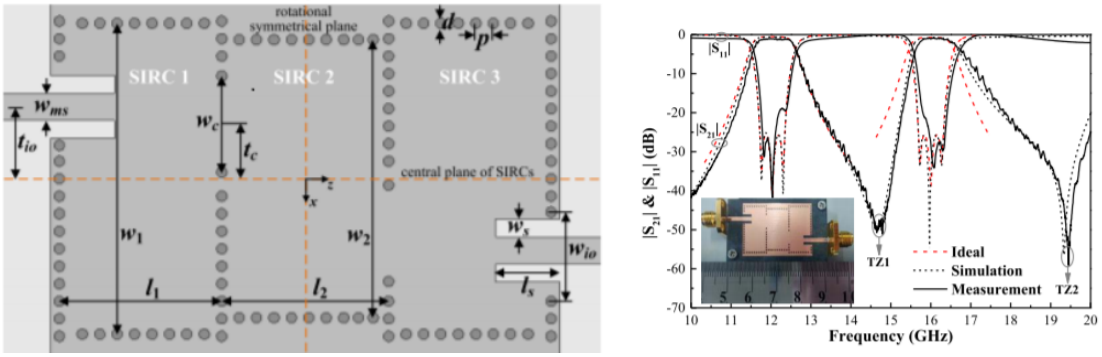

(a) (b)

Figure 2.24 – Schematic view (a) and frequency responses (b) of the dual-band filter proposed in [29].

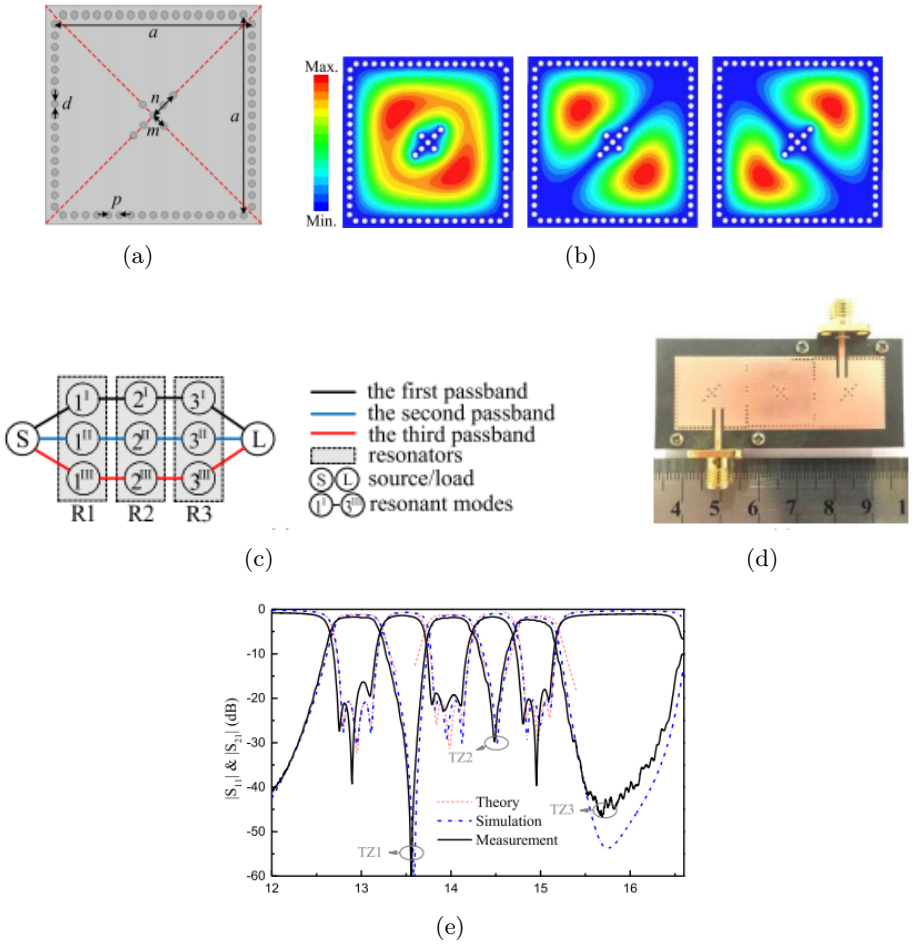

(a) (b) (c) (d) (e)

Figure 2.25 – Configuration (a) and electric field distributions of triple-mode SIW resonators (b) and coupling schematic (c) of the dual-band filter proposed in [30]. The fabricated circuit (d) and filter responses (e).

[29, 31, 32, 30, 33, 34, 35, 36]. The first method is to use a rectangular SIW resonator, which can be regarded as a special rectangular waveguide with negligible thickness. The first two modes are TE101 and TE201 modes. As described in [29], dual-mode dual-band band-pass filters with widely controllable bandwidth occur when TE101 and TE201 modes are excited in SIRC1, SIRC2 and SIRC3 cavities (presented in Fig. 2.24(a)) are exploited. By adjusting the width and length, the two modes can be excited at required frequencies. The coupling window between cavities allows to get the desired coupling coefficients. Layout and filter's response are shown in Fig. 2.24(a) and Fig. 2.24(b) respectively. Similar methods were also reported in [31, 32]. The second method consists in disturbing the guided wave propagation mode in the SIW [30, 33, 34, 35, 36] to adjust the resonance frequencies. Fig. 2.25(b) depicts the configuration of the proposed SIW tri-mode square cavity perturbed by centered cross-shaped metalized via holes in [30]. The perturbations are arranged along the two diagonals of the cavity with the arm length of m and n as shown in 2.25(a). The electric field distributions of the first three modes (mode 1, mode 2, and mode 3) in the perturbed square cavity have been changed as those in 2.25(b). Based on the resonator, a third-order tri-band band-pass filter, synthesized with Chebyshev response and a fourth-order tri-mode band-pass filter, synthesized with quasi-elliptic response have been realized as shown in 2.25(e). In [35], authors proposed slot lines perturbation to design BPFs and the filter occupies a similar area in comparison with conventional two-pole SIW filters but with better frequency selectivity. In [36], an advanced planar SIW tri-band BPF composed of two dual-mode SIW resonators (SIRC1, SIRC4) coupled with two single-mode ones (SIRC2^1, SIRC3^1) were synthesized and designed by the combination of the dual-mode (TE101 and TE201) resonances. This topology can achieve split-type dual-band symmetrical frequency response. The coupling schematic is shown in Fig.2.27(a), the simulation and measurements, in good agreement, are presented in Fig. 2.27(b). Zhou et al. (see Fig. 2.28(a)) also presented a planar SIW quint-band band-pass filter using two dual-mode SIW resonators (SIRC3^{11}, SIRC2^{11}) coupled with six single-mode ones (SIRC1, SIRC2^1, SIRC3^1, SIRC4^1, SIRC5^1, SIRC6) as shown in 2.28(a). The frequencies responses is the split-type tri-band and dual-band [37]. This approach has been shown to be very applicable for the design of filters with more than triple pass-bands.

2.2.4 Design of multiband band-pass filters by advanced methods

The fourth approach employs classical filter design theory, such as filter transfer functions, coupling matrix optimization, and frequency transformations [7, 16, 38, 39, 40, 41, 42, 17]. Typically, this type of theory can be applied to any type of filter based on different topologies and technologies (waveguide resonators, microstrip resonators, dielectric resonators). The optimization methods for the generation of multiband responses will be presented firstly [7, 16, 38]. In [7], authors presented an efficient optimization method for generating multiband characteris-

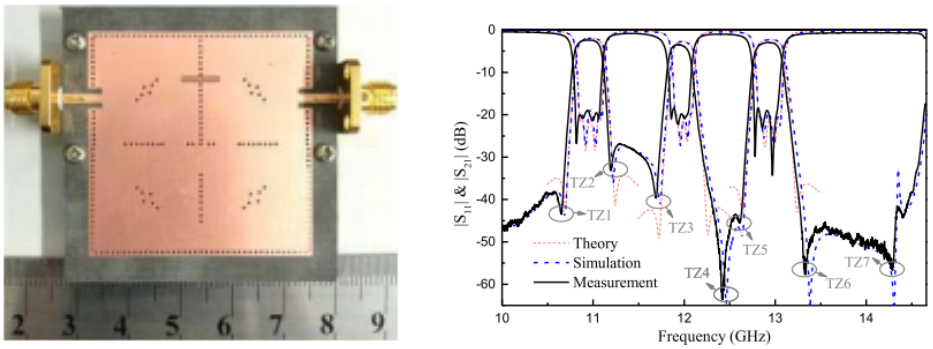

(a) (b)

Figure 2.26 – Photograph (a) and S parameters (b) of the fabricated SIW third-order Quasi-elliptic filtering responses.

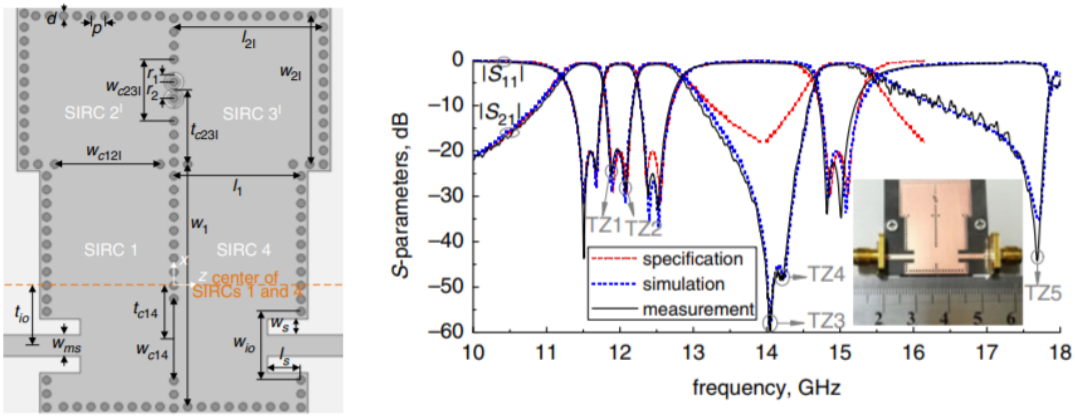

(a) (b)

Figure 2.27 – Schematic view (a) and frequency responses (b) of the tri-band filter proposed in [36].

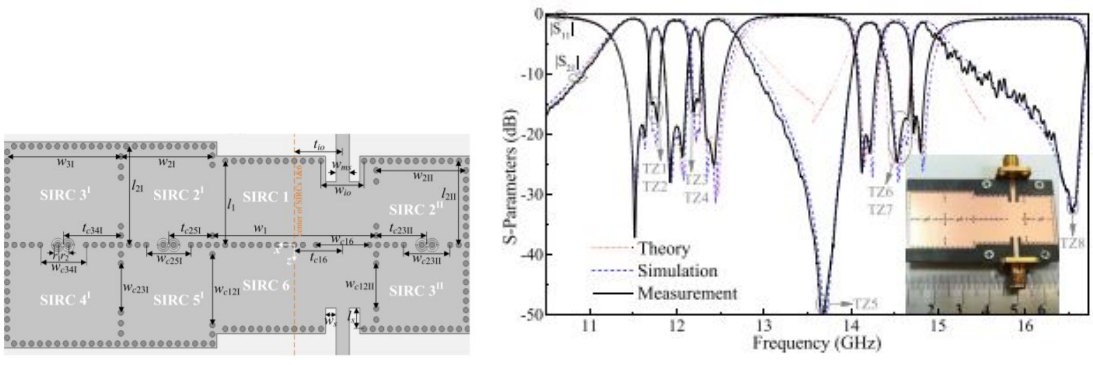

(a) (b)

Figure 2.28 – Schematic view (a) and frequency responses (b) of the quint-band filter proposed in [37].

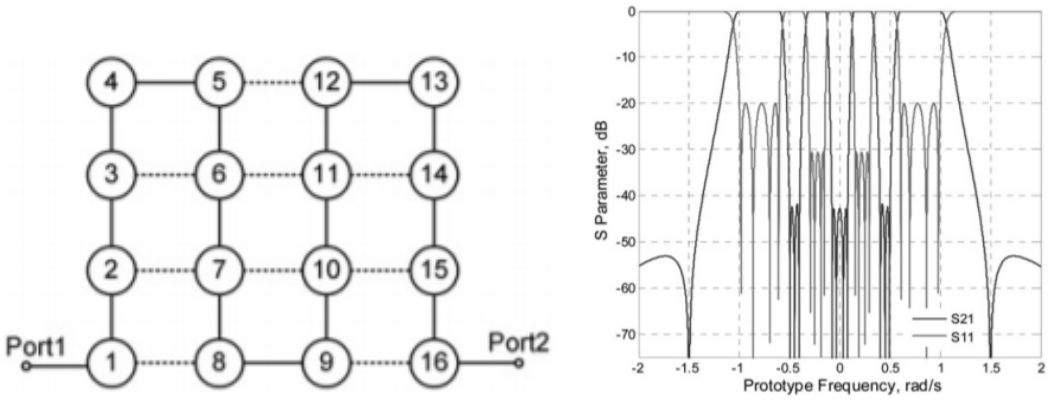

(a) (b)

Figure 2.29 – Multiband coupling schematic (a) and multiband responses based on the approximation algorithm (b) proposed in [16].

tics. The computational part consists of a differential correction-like algorithm proven to be convergent. It also guaranteed the optimality of the response. A similar optimization method was presented in [7] for synthesizing multiband filters with asymmetrical characteristics. The algorithm can also guarantee precise critical specifications in the pass and stop-band. However, a high number of optimization parameters must be optimized and this method requires large computational resources. This technique is therefore impossible to be generalized. In [38, 43, 44], the study presents the design of microwave filters based on the coupling matrix approach. The determination of the matrix was based on a hybrid optimization algorithm[38]. One of the proposed topologies is shown in Fig. 2.29(a) and the response is shown in Fig. 2.29(b). Relying on optimization algorithms is the major drawback of this type of procedure since their convergence is not guaranteed. Computing time is also very sensitive to the initial guess. Moreover, due to the applicability of the method on various filter topologies, optimization methods do not give a unique solution for the coupling matrix.

The second approach presented in this section is based on frequency transformation methods. The first dual-band band-pass filter was proposed in [17], and was realized using classical filter design theory. The proposed procedure allowed the design of symmetrical dual-band filters to have equal return loss, bandwidths and various technologies can implement the filters. A more straightforward method was presented in [45], and applied to dual-band filters with asymmetrical responses. However, the two pass-bands cannot be independently positioned, which is a major drawback. Moreover, this method can not be applied to all filter topologies. In [18], Macchiarella first proposed the frequency transformation method to design dual-band band-pass filter. The

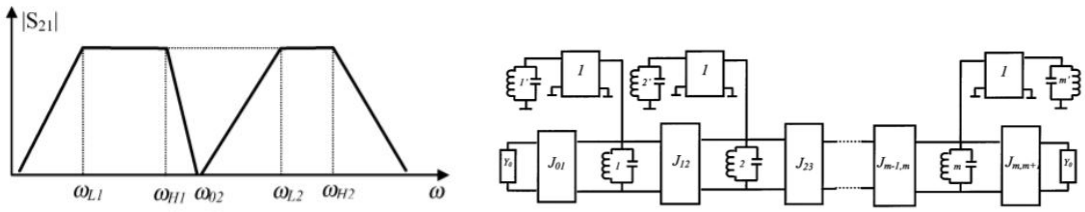

Figure 2.30 – Schematic response (a) for the dual-band filter employing the resonators. Scheme of the dual-band filter (b) obtained with the frequency transformation method [18].

proposed frequency transform function was expressed as,

$$\Omega = T(\omega) = b_0 \left(\frac{\omega}{\omega_0} - \frac{\omega_0}{\omega} \right) - \frac{1}{b_1 \left(\frac{\omega}{\omega_1} - \frac{\omega_1}{\omega} \right)} \tag{2.51}$$

where Ω is the normalized angular frequency. Variables ω_0 and ω_1 represent the self-resonant frequencies of the band-pass and band-stop resonators, respectively, and b_1 and b_2 are the slope parameters of each resonator, respectively. This transformation replaces each single-band resonator in the prototype by a dual-band resonator (one band-pass resonator and one band-stop resonator). By mapping the cut-off frequencies of the two individual bands to the low-pass filter, the transformation function can be written as a function of the input parameters (ω_{L1}, ω_{H1}, ω_{L2}, ω_{H2}) on the one hand. On the other hand, according to the resonant angular frequencies and slope parameters, the transformation equation can be expressed in terms of (b_1, b_2, ω_1, ω_2). By comparing two sets of formulas obtained by the two methods, we can get the values of slope parameters and resonating frequencies. The schematic response for the dual-band filter employing the resonators and the transformed dual-band circuit model are shown in 2.30(a) and 2.30(b), respectively. Various technological solutions can be used to implement the resulting filters. In [18], the dual-band BPF was realized by waveguide resonators. The layout and measurements are shown in Fig. 2.31.

A dual wideband filter design implemented by SIRs, which involved the frequency transformation method, was presented in [46]. Unlike the waveguide configuration, based on SIRs, it is possible to design dual-band band-pass filter in a wide frequency range. This method was also applied for SIW technology and extended to the triple-band case. In [47], the author first presented a dual-band filter with frequency transformation method. As shown in Fig. 2.32(a), resonators 1-3 are band-stop resonators and resonators 4-6 are band-pass resonators. Fig. 2.2 plots the responses of the filter. A tri-band case was also presented in Fig. 2.33(a) with responses in Fig. 2.33(b). Resonators 1-3, 4-6 are band-stop resonators and resonators 7-9 are band-pass resonators. A quad-band SIW filter was also presented by Guo [8], dual-mode dual-layer topol-

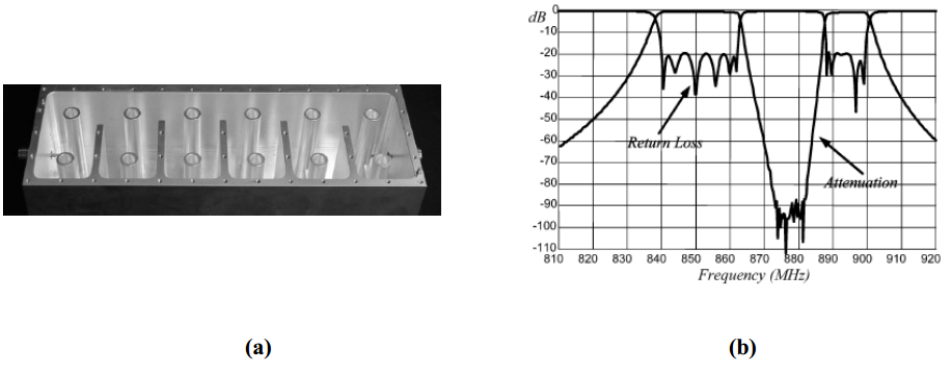

Figure 2.31 – Combine dual-band filter (a) and filter responses (b).

ogy was used to design quad-band SIW filters. But the design was also based on the frequency transformation methods for two individual dual-band transformation. No new synthesis theory was proposed.

In [48], the tri-band filter circuits with cross-coupled configuration have been constructed, microstrip ring resonators are used to realized the filter. The topology and filters' layout are shown in Fig. 2.34(a) and Fig 2.34(b). Also, various authors continued with similar transformations and demonstrated multiband responses, but all the transformation methods were limited with up to three pass-bands [49]. Even though a more general frequency transformation method was presented in [50], while overcoming many drawbacks of other techniques, this method is still not completely general, and the computation of the mapping function is not straightforward.

All in all, two drawbacks limit the application of the existing frequency transformation method. The first one is the lack of comprehensive formulas for filters beyond tri-band. The second one deals with the challenge to implement more than tri-band filters in single-layer planar circuits. Breaking these two limitations will greatly improve the application of the frequency transformation method. Fortunately, we have overcome the above two limitations. This contribution is described in the next chapter.

2.3 Conclusion

This chapter started with the introduction of the basic concepts for microwave filters. Then we gave an overview of the design technology for MBPFs, and presented four different techniques for synthesizing and designing MBPFs, illustrating the advantage and disadvantages of each technique through the presentation of some examples.

As a promising method to synthesis and design MBPFs, in this dissertation, we undertake an in-depth investigation of the frequency transformation method with different topologies. The

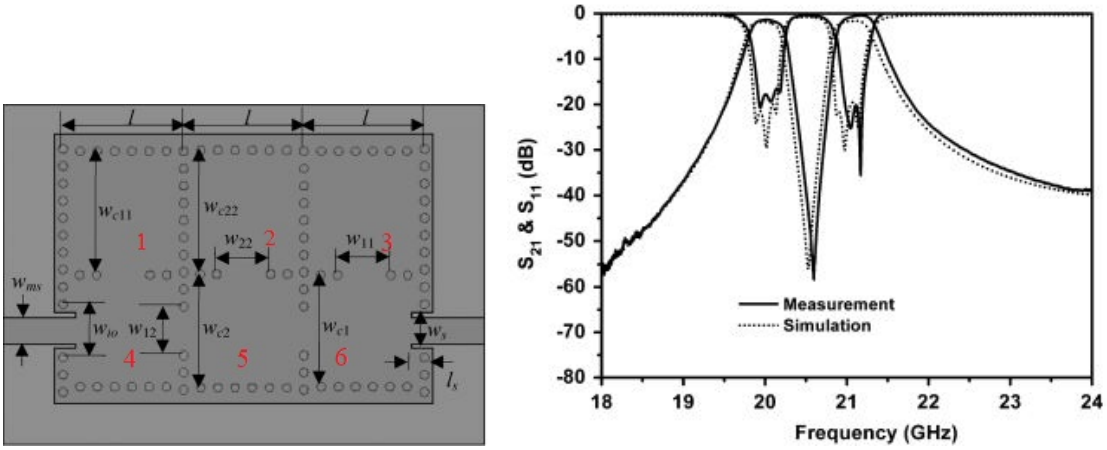

(a) layout of the proposed dual-band SIW filter.

(b) Dual-band SIW filter responses.

Figure 2.32 – Schematic view (a) and frequency responses (b) of the dual-band filter proposed in [47].

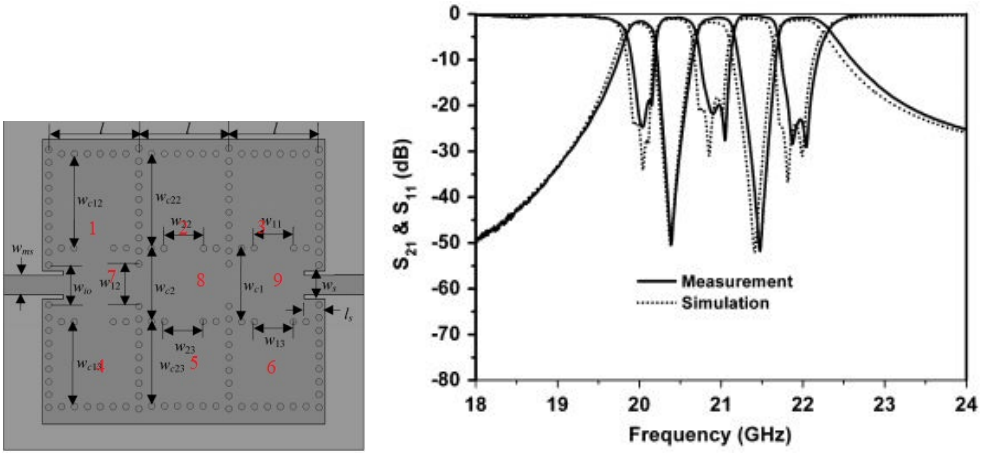

(a)

(b)

Figure 2.33 – Schematic view (a) and frequency responses (b) of the tri-band filter proposed in [47].

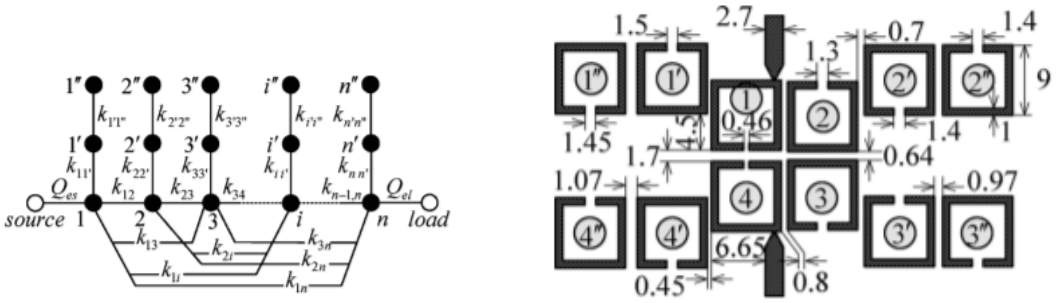

(a) [48] (b)

Figure 2.34 – Topology structure (a); layout of the cross-coupled tri-band filter (b) (1-4 band-pass resonators, the rest are band-stop resonators) [49].

frequency transformation technique offers significant advantage since it can be used to synthesize an arbitrary number of pass-band filters starting from a low-pass prototype filter. Theoretically, this synthesis allows determining analytically all the resonant angular frequencies and slope parameters of all the pass-band filters from the low and high cut-off angular frequencies used as initial specifications whatever the number of bands. However, there is the lack of comprehensive formulas for filters beyond tri-band and for their implementation in single-layer planar circuits.

In next chapter, we will present a generalized frequency transformation method with star-like topology. A rigorous mathematical analysis process is presented to obtain the generalized transform function for arbitrary number of pass-bands. It extends the frequency transformation proposed in [18] to arbitrary number of pass-band. Several examples with non-coupled structures and coupled structures will also be presented to validate the proposed theory.

Chapter 3

Direct synthesis of multiband band-pass filters with frequency transformation methods

3.1 The theory of generalized frequency transformation methods

A generalized frequency transformation function will be proposed here, this transfer function is based on the method proposed in [17] for a dual-band case. In order to show the transformation process, here we start from the well-known low-pass to band-pass frequency transformation equation in a single-band case, the transformation equation can be written as:

$$\Omega = \frac{\omega_0}{FBW}\left(\frac{\omega}{\omega_0} - \frac{\omega_0}{\omega}\right) \tag{3.1}$$

where Ω is the frequency variable for low-pass prototype in normalized frequency domain and ω is the frequency variable in de-normalized frequency domain. ω_0 is the centre frequency of the de-normalized pass-band. FBW is the equal fraction bandwidth of the de-normalized pass-band. Fig. 3.1 gives the demonstration of the process. In this figure, ω_L and ω_H is the lower

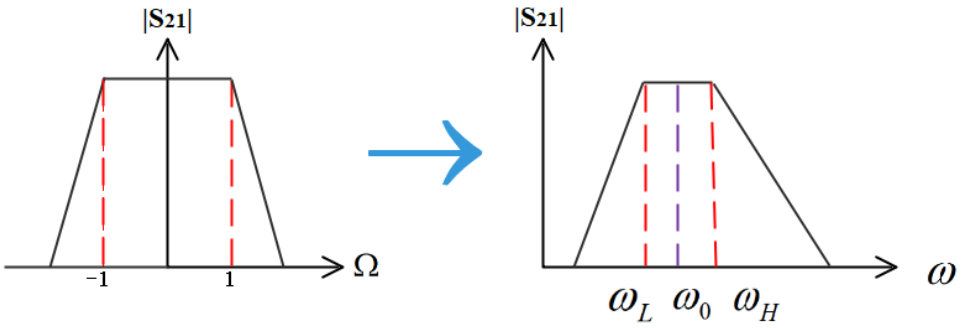

Figure 3.1 – Low-pass to band-pass frequency transformation in a single-band case.

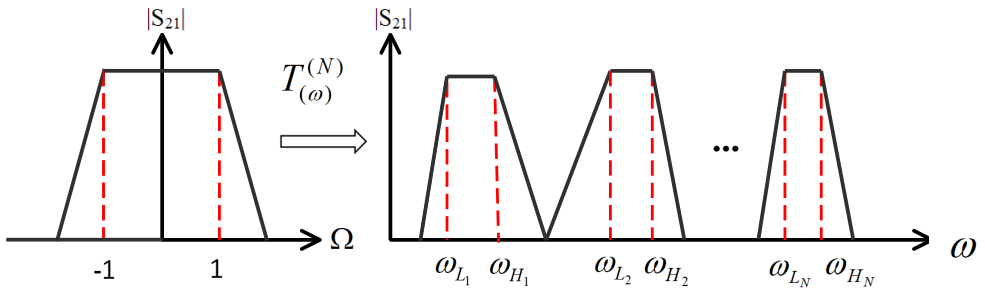

Figure 3.2 – Low-pass to band-pass frequency transformation in a multiband case.

and upper cut-off angular frequencies of the pass-band. For dual-band case, a transmission zero can be introduced in the pass-band to split the single-band band-pass filter to dual-band case, as proposed by Macchiarella [17] in 2005 with rigorous mathematical expressions. The proposed frequency transform function was expressed as:

$$\Omega = T^{(2)}(\omega) = b_0 \left(\frac{\omega}{\omega_0} - \frac{\omega_0}{\omega} \right) - \frac{1}{b_1 \left(\frac{\omega}{\omega_1} - \frac{\omega_1}{\omega} \right)} \tag{3.2}$$

$T^{(2)}(\omega)$ is the transformation function for dual-band cases. ω_0 and b_0 are respectively the resonant angular frequency and the susceptance slope parameter of the wide band-pass resonators, where ω_1 and b_1 are the ones of the stop-band resonators. By mapping all the pass-band edge frequencies to the low-pass domain, this function could be solved perfectly. Then, the coupling values associated with the solved ω_0, b_0, ω_1 and b_1 can be obtained by using the general equations presented in [17].

This enables to perform the filter implementation using various technologies. Based on this initial idea, we extend this method in a more general way. The transformation from a classical low-pass prototype to an N-bands band-pass filter is schematically presented in Fig. 3.2. The general function can be written as below:

$$\begin{aligned} \Omega &= T^{(N)}(\omega) \\ &= b_0 \left(\frac{\omega}{\omega_0} - \frac{\omega_0}{\omega} \right) - \sum_{k=1}^{N-1} \frac{1}{b_k \left(\frac{\omega}{\omega_k} - \frac{\omega_k}{\omega} \right)} \end{aligned} \tag{3.3}$$

$T^{(N)}(\omega)$ is the transformation function, N the number of bands of the MBPF. ω_0 and b_0 are respectively the resonant angular frequency and the susceptance slope parameter of the wide band-pass resonators, while ω_k and b_k ($k \in [1; N-1]$) are the ones of the $N-1$ stop-band resonators.

The goal of the synthesis process is to link the $2N$ output parameters of the transformation

function (the resonant angular frequencies ω_k and the slope parameters b_k, $k \in [1; N-1]$) to the input ones, i.e the low and high cut-off angular frequencies of the N bands (ω_{L_i} and ω_{H_i}, $i \in [1; N]$) as defined in Fig. 3.2.

First, the $U^{(N)}(\omega)$ function as follow:

$$U^{(N)}(\omega) = T^{(N)}(\omega) - 1 \tag{3.4}$$

Substituting equation (3.3) for $T^{(N)}(\omega)$ in (3.4) leads to a new expression $U^{(N)}(\omega)$ consisting in a ratio of two polynomials:

$$U^{(N)}(\omega) = \frac{N(\omega)}{D(\omega)} = \frac{\omega^{2N} + \sum_{p=0}^{2N-1} n_p \omega^p}{\sum_{q=0}^{2N-1} d_q \omega^q} \tag{3.5}$$

where d_q is equal to 0 when q is even and $-n_q$ when q is odd. A first expression of the $2N$ n_p ($p \in [0; 2N-1]$) coefficients is then obtained as functions of the output parameters.

We now assumed that the lower cut-off angular frequencies ω_{L_i} and the upper cut-off angular frequencies ω_{H_i} ($i \in [1; N]$) are mapped to -1 and +1 in the Ω normalized domain respectively. As $T^{(N)}(\omega)$ is an odd function, we then have:

$$T^{(N)}(-\omega_{L_i}) = T^{(N)}(\omega_{H_i}) = 1 \qquad i \in [1; N] \tag{3.6}$$

Therefore, the N high cut-off angular frequencies and the opposite of the N lower cut-off ones are the $2N$ roots of $U^{(N)}(\omega)$. A second expression of the n_p coefficients is thus obtained as functions of the input parameters this time.

So, $2N$ equations (one for each n_p coefficient) link the N resonant angular frequencies, ω_k, and the N slope parameters, b_k ($(k \in [0; N-1])$), to the N low cut-off angular frequencies, ω_{L_i}, and the N high cut-off ones, ω_{H_i} ($i \in [1; N]$). As presented below, an analytical expression can be obtained for each output parameter.

The general expressions of the n_p coefficients ($p \in [0; 2N-1]$) according to the cut-off angular frequencies on the one hand and according to the resonant angular frequencies and slope parameters on the other hand will be presented in the following. In order to simplify the writing of these equations and make the understanding easier, we first introduce specific mathematical expressions in section 3.1.1.

3.1.1 Specific mathematical operators

Let $\mathcal{Z}^{(r\to s)}$ be a set of real numbers z_i with $i \in [r;s]$ ($r \in \mathbb{N}$ and $s \in \mathbb{N}^\star$):

$$\mathcal{Z}^{(r\to s)} = \{z_i\}_{i=r}^{s} \tag{3.7}$$

We then denote $\mathcal{Z}_{\{j\}}^{(r\to s)}$ the same set of real numbers z_i with $i \neq j$ ($(i;j) \in [r;s]$):

$$\begin{aligned} \mathcal{Z}_{\{j\}}^{(r\to s)} &= \{z_i\}_{i=r}^{s} \setminus \{z_j\} \\ &= \{z_r, z_{r+1}, \cdots, z_{j-1}, z_{j+1}, \cdots, z_{s-1}, z_s\} \end{aligned} \tag{3.8}$$

Let $\mathcal{P}_a\left(\mathcal{Z}^{(r\to s)}\right)$ be the sum of all the different products of a elements of $\mathcal{Z}^{(r\to s)}$. As a consequence, $\mathcal{P}_a\left(\mathcal{Z}^{(r\to s)}\right)$ is a sum of $\begin{pmatrix} s-r+1 \\ a \end{pmatrix}$ terms, each of them being a product of a elements of $\mathcal{Z}^{(r\to s)}$. For instance:

$$\begin{aligned} \mathcal{P}_1\left(\mathcal{Z}^{(1\to 3)}\right) &= z_1 + z_2 + z_3 \\ \mathcal{P}_2\left(\mathcal{Z}^{(1\to 3)}\right) &= z_1z_2 + z_1z_3 + z_2z_3 \\ \mathcal{P}_3\left(\mathcal{Z}^{(1\to 3)}\right) &= z_1z_2z_3 \end{aligned}$$

and

$$\mathcal{P}_2\left(\mathcal{Z}_{\{3\}}^{(1\to 4)}\right) = z_1z_2 + z_1z_4 + z_2z_4$$

Finally, we denote:

$$\mathcal{P}_0\left(\mathcal{Z}^{(r\to s)}\right) = 1 \tag{3.9}$$

3.1.2 General synthesis development

As explained just before, the $2N$ n_p coefficients used in (3.5) can be obtained as functions of the frequency transformation input parameters, i.e the cut-off angular frequencies of the N bands. We use here the fact that the N high cut-off angular frequencies ω_{H_i} and the opposite of the low cut-off ones ω_{L_i}, with $i \in [1;N]$, are the zeros of $U^{(N)}(\omega)$. We thus obtain a first system of $2N$ equations (one for each cut-off angular frequency) with $2N$ unknowns (n_p, $p \in [0;2N-1]$).

According to expressions presented in (3.7)-(3.9), we denote $\mathcal{L}^{(1\to N)} = \{\omega_{L_i}\}$ and $\mathcal{H}^{(1\to N)} =$

$\{\omega_{H_i}\}$, $i \in [1; N]$. Solving this first system then leads to:

$$\begin{aligned} n_p &= \sum_{r=0}^{p} (-1)^{N-r} \mathcal{P}_{N-r}\left(\mathcal{H}^{(1\to N)}\right) \mathcal{P}_{N+r-p}\left(\mathcal{L}^{(1\to N)}\right) \\ &\text{for } p \in [0; N-1] \\ &= \sum_{r=p}^{2N} (-1)^{2N-r} \mathcal{P}_{2N-r}\left(\mathcal{H}^{(1\to N)}\right) \mathcal{P}_{r-p}\left(\mathcal{L}^{(1\to N)}\right) \\ &\text{for } p \in [N; 2N-1] \end{aligned} \tag{3.10}$$

We now express the $2N$ n_p coefficients as functions of the frequency transformation output parameters, i.e the resonant angular frequency, ω_0, and the slope parameter, b_0, of the wide band-pass resonator, and the parameters ω_k and b_k ($k \in [1; N-1]$). We recall that these parameters are the resonant angular frequencies and the slope parameters of the stop-band resonators respectively. This is based on the introduction of the expression of $T^{(N)}(\omega)$ from (3.3) in (3.4) which allowed us to obtain the expression of $U^{(N)}(\omega)$ given in (3.5). We thus obtain a second system of $2N$ equations giving each n_p coefficient as a function of the output parameters.

Here, we denote $\mathcal{W}^{(0\to N-1)} = \{\omega_k^2\}$ the set of all the resonant angular frequency squares and $\mathcal{W}^{(1\to N-1)} = \{\omega_k^2\}$ the set of the resonant angular frequency squares of the stop-band resonators only. We distinguish three cases for $p = 0$, p odd and p even, $p \in [0; 2N-1]$.

— For $p = 0$, we have:

$$\begin{aligned} n_0 &= (-1)^N \mathcal{P}_N\left(\mathcal{W}^{(0\to N-1)}\right) \\ &= (-1)^N \prod_{r=0}^{N-1} \omega_r^2 \end{aligned} \tag{3.11}$$

— For p odd, we denote $p = 2q-1$, $q \in [1; N]$. We then have:

$$\begin{aligned} n_p &= n_{2q-1} \\ &= (-1)^{N-q+1} \frac{\omega_0}{b_0} \mathcal{P}_{N-q}\left(\mathcal{W}^{(1\to N-1)}\right) \end{aligned} \tag{3.12}$$

— For p even, we denote $p = 2q$, $q \in [1; N-1]$, and then we obtain:

$$\begin{aligned} n_p &= n_{2q} \\ &= (-1)^{N-q} \left\{ \mathcal{P}_{N-q}\left(\mathcal{W}^{(0\to N-1)}\right) \right. \\ &\left. + \frac{\omega_0}{b_0} \sum_{k=1}^{N-1} \left[\frac{\omega_k}{b_k} \mathcal{P}_{N-q-1}\left(\mathcal{W}_{\{k\}}^{(1\to N-1)}\right) \right] \right\} \end{aligned} \tag{3.13}$$

Equations (3.11) to (3.13) give an expression of the $2N$ n_p as functions of the output parameters of the frequency transformation technique (i.e ω_k and b_k, $k \in [0; N-1]$). In a practical way, we have to reverse this equations system in order to express the output parameters as functions of the $2N$ n_p coefficients, these latter being calculated from the input parameters (ω_{L_i} and ω_{H_i} ($i \in [1; N]$)) using (3.10).

First, using the expressions of n_0, n_1 and n_{2N-1} and whatever the number of bands N, we can easily demonstrate that the resonant frequency ω_0 and the slope parameter b_0 of the wide band-pass filter can be written as:

$$\omega_0 = \sqrt{-\frac{n_0 n_{2N-1}}{n_1}} \tag{3.14}$$

$$b_0 = \sqrt{-\frac{n_0}{n_1 n_{2N-1}}} \tag{3.15}$$

Using (3.12) for all the odd value of p, we can also demonstrate that (as presented in Appendix 7.1) the resonant angular frequencies of the band-stop resonators (ω_k, $k \in [1; N-1]$)) are the $N-1$ positive solutions of (3.16):

$$\sum_{r=0}^{N-1} n_{2r+1} \omega_k^{2r} = 0 \tag{3.16}$$

Once the resonant angular frequencies of the band-stop resonators are determined using (3.16), the remaining unknowns are the slope parameter coefficients b_k, $k \in [1; N-1]$ in (3.13). This equation can also be rewritten as follows:

$$\sum_{k=1}^{N-1} \left[\frac{\omega_k}{b_k} \mathcal{P}_{N-q-1}\left(\mathcal{W}_{\{k\}}^{(1\to N-1)}\right) \right] = \frac{\mathcal{P}_{N-q}\left(\mathcal{W}^{(0\to N-1)}\right) - (-1)^{N-q} n_{2q}}{n_{2N-1}} \tag{3.17}$$

for $q \in [1; N-1]$. Using (3.17) for each value of q, we obtain an $N-1$ linear equations system with $(N-1)$ unknowns (i.e each b_k, or more precisely $1/b_k$). This system can be written as

follows:

$$X_{N-1,N-1}B_{N-1} = A_{N-1} \tag{3.18}$$

where $X_{N-1,N-1}$ is the $(N-1 \times N-1)$ matrix of $x_{q,k}$ coefficients with:

$$x_{q,k} = \omega_k \mathcal{P}_{N-q-1}\left(\mathcal{W}_{\{k\}}^{(1\to N-1)}\right) \tag{3.19}$$

B_{N-1} is the vector of the $N-1$ unknowns:

$$B_{N-1} = \left[\frac{1}{b_1}, \frac{1}{b_2}, \cdots, \frac{1}{b_{N-1}}\right]^t \tag{3.20}$$

and A_{N-1} is the vector of already known coefficients $a_q^{(N)}$:

$$A_{N-1} = [a_1, a_2, \cdots, a_{N-1}]^t \tag{3.21}$$

with

$$a_q = \frac{\mathcal{P}_{N-q}\left(\mathcal{W}^{(0\to N-1)}\right) - (-1)^{N-q}\, n_{2q}}{n_{2N-1}} \tag{3.22}$$

The slope parameters are then determined by inverting the matrix $X_{N-1,N-1}$:

$$B_{N-1} = X_{N-1,N-1}^{-1} A_{N-1} \tag{3.23}$$

$$b_k = \frac{\omega_k \prod\limits_{j=1,j\neq k}^{N-1}\left(\omega_k^2 - \omega_j^2\right)}{\sum\limits_{j=1}^{N-1} Y_j \omega_k^{2j-2}} \tag{3.24}$$

$$Y_j = \frac{n_{2j} - \dfrac{n_0 n_{2j+1}}{n_1} - \dfrac{n_{2j-1}}{n_{2N-1}}}{n_{2N-1}} \tag{3.25}$$

where $k \in [1; N-1]$, $N \geqslant 3$.

3.1.3 Application: the case of tri-bands

To well explain these generalized equations, we proposed here to develop them in a tri-band case. To determine the slope parameters of the tri-band resonators, we first determine the parameters of $X_{2,2}$,

$$X_{2,2} = \begin{Bmatrix} x_{1,1}^{(3)} & x_{1,2}^{(3)} \\ x_{2,1}^{(3)} & x_{2,2}^{(3)} \end{Bmatrix}$$

where

$$x_{1,1}^{(3)} = \omega_1 \mathcal{P}_1\left(\mathcal{W}_{\{1\}}^{(1\to 2)}\right) = \omega_1\omega_2^2 \tag{3.26}$$

$$x_{1,2}^{(3)} = \omega_2 \mathcal{P}_1\left(\mathcal{W}_{\{2\}}^{(1\to 2)}\right) = \omega_2\omega_1^2 \tag{3.27}$$

$$x_{2,1}^{(3)} = \omega_1 \mathcal{P}_0\left(\mathcal{W}_{\{1\}}^{(1\to 2)}\right) = \omega_1 \tag{3.28}$$

$$x_{2,2}^{(3)} = \omega_2 \mathcal{P}_0\left(\mathcal{W}_{\{2\}}^{(1\to 2)}\right) = \omega_2 \tag{3.29}$$

so, the matrix $X_{2,2}$ can be expressed as,

$$a_1^{(3)} = \frac{\mathcal{P}_2\left(\mathcal{W}^{(0\to 2)}\right) - (-1)^2 n_2^{(3)}}{n_5^{(3)}} \tag{3.30}$$

$$a_2^{(3)} = \frac{\mathcal{P}_1\left(\mathcal{W}^{(0\to 2)}\right) - (-1)^1 n_4^{(3)}}{n_5^{(3)}} \tag{3.31}$$

where

$$\mathcal{P}_2\left(\mathcal{W}^{(0\to 2)}\right) = \omega_0^2\omega_1^2 + \omega_0^2\omega_2^2 + \omega_1^2\omega_2^2 \tag{3.32}$$

$$\mathcal{P}_1\left(\mathcal{W}^{(0\to 2)}\right) = \omega_0^2 + \omega_1^2 + \omega_2^2 \tag{3.33}$$

The values of ω_k in terms of n are determined, from (3.14) and the solutions of (3.16). By using these relationships, we can express

$$a_1^{(3)} = -\frac{n_2^{(3)} - \dfrac{n_0^{(3)} n_3^{(3)}}{n_1^{(3)}} - \dfrac{n_1^{(3)}}{n_5^{(3)}}}{n_5^{(3)}} = -Y_1^{(3)} \tag{3.34}$$

$$a_2^{(3)} = \frac{n_4^{(3)} - \dfrac{n_0^{(3)} n_5^{(3)}}{n_1^{(3)}} - \dfrac{n_3^{(3)}}{n_5^{(3)}}}{n_5^{(3)}} = Y_2^{(3)} \tag{3.35}$$

The inverse matrix of $X_{2,2}$ is

$$X_{2,2}^{-1} = \frac{1}{\omega_1\omega_2(\omega_2^2 - \omega_1^2)} \begin{Bmatrix} \omega_2 & -\omega_2\omega_1^2 \\ -\omega_1 & \omega_1\omega_2^2 \end{Bmatrix}$$

$$B_2 = X_{2,2}^{-1} A_2 \tag{3.36}$$

By using (3.36), we can easily get the same results as we already proposed in section 3.1.1 (equations (3.24) and (3.25)).

$$b_1 = \frac{\omega_1(\omega_1^2 - \omega_2^2)}{Y_1^{(3)} + Y_2^{(3)}\omega_1^2} \tag{3.37}$$

$$b_2 = \frac{\omega_2(\omega_2^2 - \omega_1^2)}{Y_1^{(3)} + Y_2^{(3)}\omega_2^2} \tag{3.38}$$

with

$$Y_1^{(3)} = \frac{n_2^{(3)} - \frac{n_0^{(3)} n_3^{(3)}}{n_1^{(3)}} - \frac{n_1^{(3)}}{n_5^{(3)}}}{n_5^{(3)}} \tag{3.39}$$

$$Y_2^{(3)} = \frac{n_4^{(3)} - \frac{n_0^{(3)} n_5^{(3)}}{n_1^{(3)}} - \frac{n_3^{(3)}}{n_5^{(3)}}}{n_5^{(3)}} \tag{3.40}$$

After determination of the resonant frequencies and the slope parameters of the pass-band and stop-band elements of the multiband resonators, we use them to implement multiband filters. We first propose an ideals lump -elements implementation based on a classical ladder structure is composed of series inductances and shunt capacitances, a low-pass prototype filter can be modified to use only parallel capacitances separated by J admittance inverters. Using the generalized frequency transformation technique presented in Section 3.1.1, the i^{th} capacitance, C_i^{LP}, of such a low-pass prototype can be transformed into a multi-band band-pass resonator as shown in Fig. 3.3. The multi-band band-pass resonator then obtained consists in the parallel association of one band-pass resonator $(L_0^{(i)}; C_0^{(i)})$ and $N-1$ band-stop ones $(L_k^{(i)}; C_k^{(i)})$, $k \in [1; N-1]$ whose values are given by the equations below:

$$L_0^{(i)} = \frac{1}{b_0 C_i^{LP} \omega_0} \tag{3.41}$$

$$C_0^{(i)} = \frac{1}{L_0^{(i)} \omega_0^2} \tag{3.42}$$

$$L_k^{(i)} = \frac{b_k}{C_i^{LP} \omega_k} \tag{3.43}$$

$$C_k^{(i)} = \frac{1}{L_k^{(i)} \omega_k^2} \tag{3.44}$$

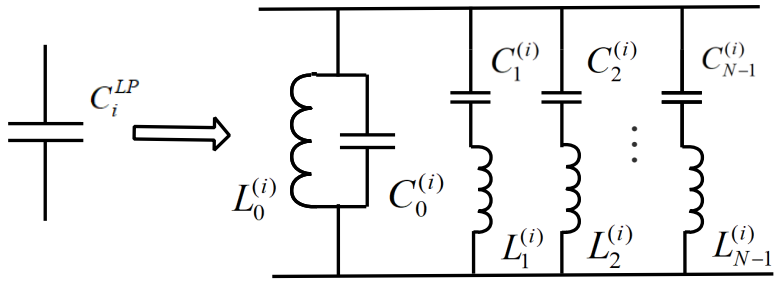

Figure 3.3 – Transformation of a low-pass prototype capacitance into a multi-band band-pass resonator (MBPR).

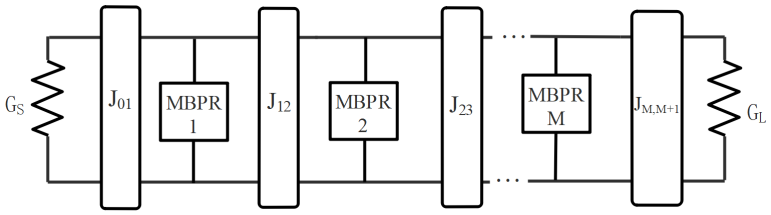

Figure 3.4 – Prototype of the proposed MBPFs-the based wide-band BPF.

A M-order MBPF is then composed of M multi-band band-pass resonator (MBPR) separated by J admittance inverters as shown in Fig. 3.4. The $J_{i,i+1}$ inverters are here defined in a classical way taking into account only the band-pass part of each multi-band band-pass resonator:

$$J_{01} = \sqrt{\frac{G_S \beta_0^{(1)}}{b_0 g_0 g_1}} \tag{3.45}$$

$$J_{i,i+1} = \frac{1}{b_0}\sqrt{\frac{\beta_0^{(i)}\beta_0^{(i+1)}}{g_k g_{k+1}}} \tag{3.46}$$

$$J_{M,M+1} = \sqrt{\frac{G_L \beta_0^{(M)}}{b_0 g_M g_{M+1}}} \tag{3.47}$$

where the g_i coefficients are the low-pass prototype parameters, G_S and G_L are the source load impedances, and $\beta_0^{(i)}{=}\omega_0 C_0^{(i)}$.

In order to use only band-pass resonators, as it was been done in the following, all the stop-band LC-series elements can be transformed in LC-parallel ones using another set of J-inverters. A MBPR then consists only in LC-parallel resonators (see Fig. 3.5), the main one $(L_0^{(i)}, C_0^{(i)})$ being separated from the others $(L_k^{(i)}, C_k^{(i)})$, $k \in [1; N-1]$ and $i \in [1; M]$, by additional J-

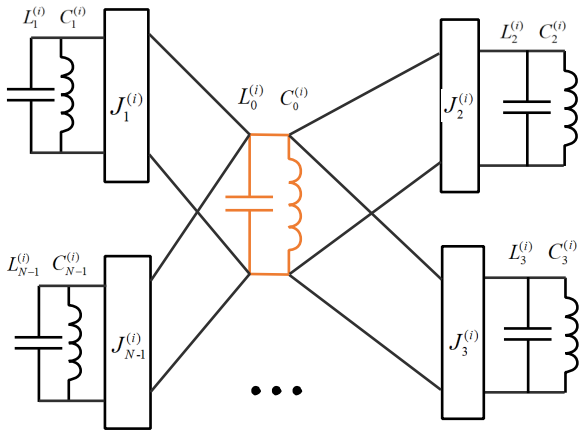

Figure 3.5 – Multiband band-pass resonators (MBPR) with parallel LC resonators.

inverters:

$$J_k^{(i)} = \sqrt{\frac{\beta_0^{(i)}\beta_k^{(i)}}{b_0 b_k}} \tag{3.48}$$

with $\beta_k^{(i)}=\omega_k C_k^{(i)}$.

3.2 Synthesis and experimental validation of the proposed multi-band band-pass filters

For validating the frequency transformation method and the implementation proposed in the previous sections, three examples of multi-band band-pass filters have been synthesized and experimentally validated with 3, 4 and 5 bands respectively. In the first case (tri-band filter), all the output parameters expressions obtained from (3.14) to (3.23) were presented in section 3.1.3. In the two other cases, for the sake of clarity, these expressions are presented in Appendix 7.2.

The three test filters are of order 3 with a Chebyshev approximation and 20 dB pass-band return loss (RL). There are implemented in microstrip technology using a RO4003C Rogers substrate (dielectric constant: $\varepsilon_r = 3.55$, height: $h = 0.508$ mm, dissipation factor: $\tan\delta = 0.0027$) with copper metallization (metal thickness: $t = 17.5$ μm, conductivity: $\sigma = 5.8 \times 10^7$ S.m^{-1}). All multi-band band-pass resonators use a star-like structure connecting N stubs at a same point allowing the implementation of such multi-band filters without a significant increase of the circuit size compared to mono-band one. All prototypes were simulated and optimized using ADS software from Keysight Technologies© and fabricated by laser engraving using a LPKF Protolaser U4.

3.2.1 Tri-band to quint-band band-pass filters

Tri-band band-pass filter

To synthesize a tri-band band-pass filter using the frequency transformation method proposed here, one needs to take $N = 3$ in equations (3.14) to (3.25). We have already obtained these equations in 3.1.3 with details.

The specifications of a tri-band band-pass filter given in terms of low and high cut-off angular frequencies can then be transposed in terms of resonant angular frequencies and slope parameters. As an example, the arbitrary following specifications are proposed:

1. Pass-band 1: 2.00 GHz-2.10 GHz (BW: 100 MHz);
2. Pass-band 2: 2.45 GHz-2.65 GHz (BW: 200 MHz);
3. Pass-band 3: 2.95 GHz-3.20 GHz (BW: 250 MHz);

The resulting resonant frequencies and slope parameters are: $f_0 = \omega_0/2\pi = 2.604$ GHz, $f_1 = \omega_1/2\pi = 2.191$ GHz, $f_2 = \omega_2/2\pi = 2.812$ GHz, $b_0 = 4.735$, $b_1 = 4.277$ and $b_2 = 5.818$. A tri-band third-order band-pass filter is first implemented in an ideal L-C structure (see Fig. 3.4), each resonator following the model of Fig. 3.5. All the resonator components and J-inverters, calculated from equations (3.41) to (3.48), are given in Table 3.1. Note that the three tri-band resonators are identical in order to simplify the microstrip implementation in the next step. This is possible by fixing the three C_i^{LP} components at the same value using an admittance scale factor when introducing the J-inverters in the low-pass prototype. Fig. 3.7(c) shows the frequency response of this filter.

The filter was then implemented in microstrip technology with the substrate characteristics given in the introduction of this section. Each star is made of a tri-band resonator together with its previous and next inverters. A tri-band resonator consists in one band-pass element, i.e a short-circuit stub of length $\lambda/4$ at ω_0, and two stop-band ones consisting of a short-circuit stub of length $\lambda/4$ at ω_1 and ω_2 respectively and separated from the connection point by another quarter-wavelength line at the same respective frequency having the J-inverter role. All lengths and widths of the resonators and the inverters are given in Fig.3.7(a) and Fig.3.7(b). The tri-band filter is 72.1×68.5 mm^2 without taking account for the two 50 Ω access lines.

Fig. 3.7(c) presents the EM-simulated and measured frequency responses of the fabricated tri-band band-pass filter. The correlation between both responses is very good over the entire frequency band. The measured return loss (RL) are 12.3 dB, 14.9 dB and 14.1 dB from the first to the last pass-band and the measured insertion loss (IL) are 1.98 dB, 2.17 dB, and 2.01 dB respectively. The isolation between the three pass-bands reaches 58.1 dB and 57.6 dB.

Quad-band band-pass filter

Table 3.1 – Component values of the ideal L-C triple-band third-order band-pass filter.

Resonators ($i \in [1;3]$)		
$L_0^{(i)} = 1.586$ nH	$L_1^{(i)} = 1.902$ nH	$L_2^{(i)} = 1.603$ nH
$C_0^{(i)} = 2.412$ pF	$C_1^{(i)} = 2.892$ pF	$C_2^{(i)} = 2.355$ pF
$L_3^{(i)} = 1.315$nH		$C_3^{(i)} = 2.211$ pF
$J_1^{(i)} = 0.0078$ S	$J_2^{(i)} = 0.0074$ S	$J_3^{(i)} = 0.0067$ S
Inverters ($J_{i,i+1}$)		
$J_{01} = J_{34} = 0.013$ S		$J_{12} = J_{23} = 0.0074$ S

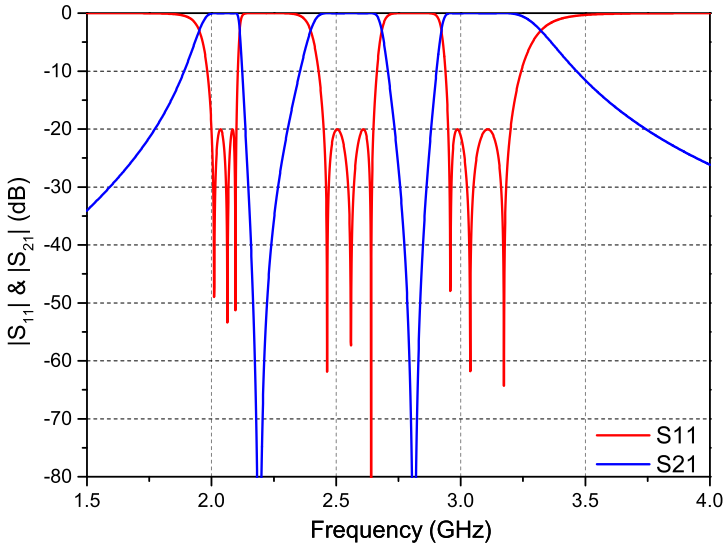

Figure 3.6 – Tri-band filter with ideal responses.

Table 3.2 – Microstrip tri-band third-order band-pass filter: length and width dimensions *(in mm)*.

Resonators		
$L_0 = 17.50$	$L_1 = 18.80$	$L_2 = 14.50$
$W_0 = 0.92$	$W_1 = 3.36$	$W_2 = 3.50$
$L_{J1} = 18.70$		$L_{J2} = 16.50$
$W_{J1} = 0.15$		$W_{J2} = 0.12$
Inverters		
$L_{01} = 17.70$		$L_{12} = 18.34$
$W_{01} = 0.51$		$W_{12} = 0.11$

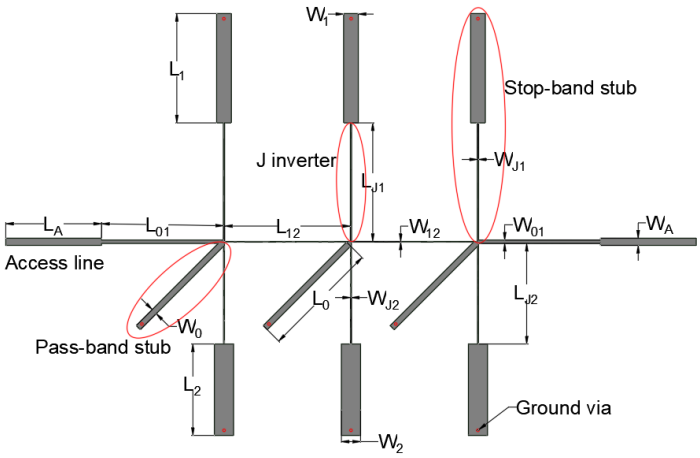

(a)

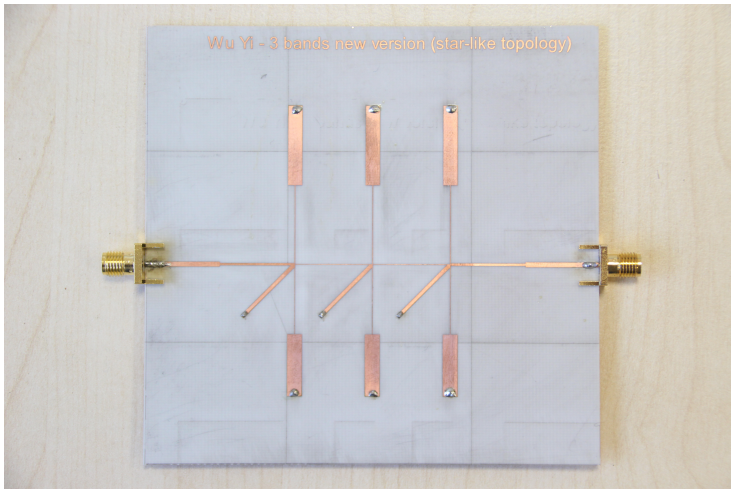

(b) The photo of the fabricated tri-band filter.

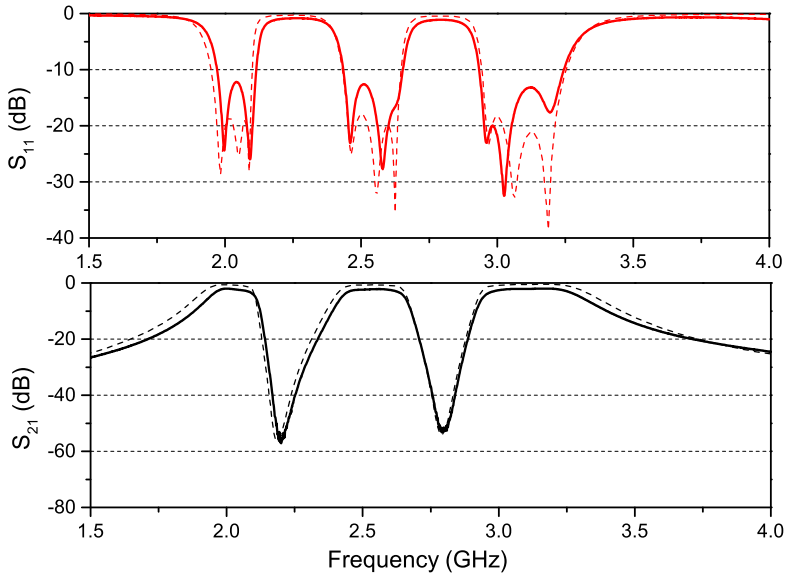

(c)

Figure 3.7 – Layout of the fabricated tri-band band-pass filter (a). The photo of the fabricated tri-band filter (b). EM-simulated (dotted lines) and measured (solid lines) S-parameters of the triple-band band-pass filter (c).

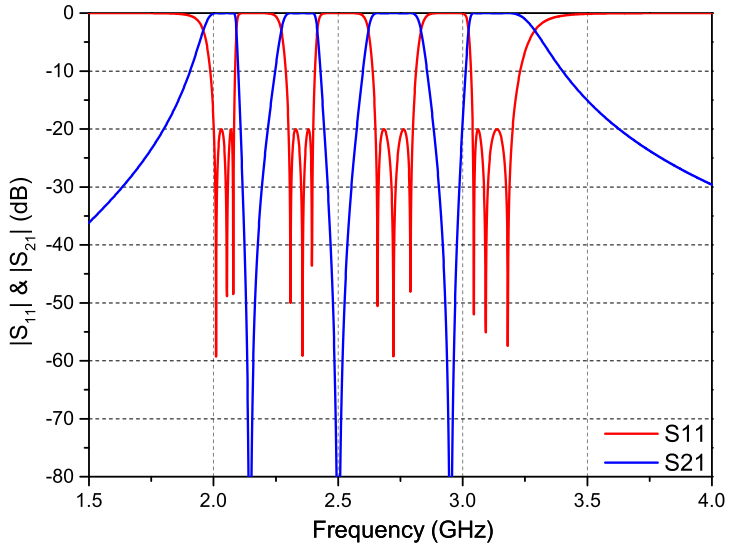

Figure 3.8 – Ideal frequency response of the specified quad-band band-pass filter.

The quad-band MBPFs specifications will be introduced in this part. One should be aware of the fact that there are still few papers paying attention to the high-order quad-band MBPFs, in [8] the author proposed a third-order SIW quad-band BPFs with multilayer technologies and the configuration of the filter as well as the turning process of the filter is not easy to achieved. Until now nearly all the quad-band MBPFs are second-order filters so the out-of-band rejections are typically not so good. Our synthesis method allows a much easier design of quad-band (and beyond) MBPFs with high out-of-band rejections.

In the same way as for the tri-band case, the synthesis of a quad-band band-pass filter using this frequency transformation method starts with the determination of the expression of the resonant angular frequencies and the associated slope parameters as functions of the low and high cut-off frequencies. To do so, one takes $N = 4$ in equations (3.14) to (3.25). The resulting equations are presented in Appendix 7.2 for a sake of clarity.

A first set of specifications are also proposed here as an example to design, fabricate and measure a third-order quad-band band-pass filter. The specifications proposed for this filter show different bandwidths for each band and are the following:

1. Pass-band 1: 2.00 GHz-2.08 GHz (BW: 80 MHz);
2. Pass-band 2: 2.30 GHz-2.40 GHz (BW: 100 MHz);
3. Pass-band 3: 2.65 GHz-2.80 GHz (BW: 150 MHz);
4. Pass-band 4: 3.04 GHz-3.20 GHz (BW: 160 MHz).

The resulting resonant frequencies and slope parameters are: $f_0 = \omega_0/2\pi = 2.573$ GHz, $f_1 = \omega_1/2\pi = 2.146$ GHz, $f_2 = \omega_2/2\pi = 2.501$ GHz, $f_3 = \omega_3/2\pi = 2.951$ GHz, $b_0 = 5.251$,

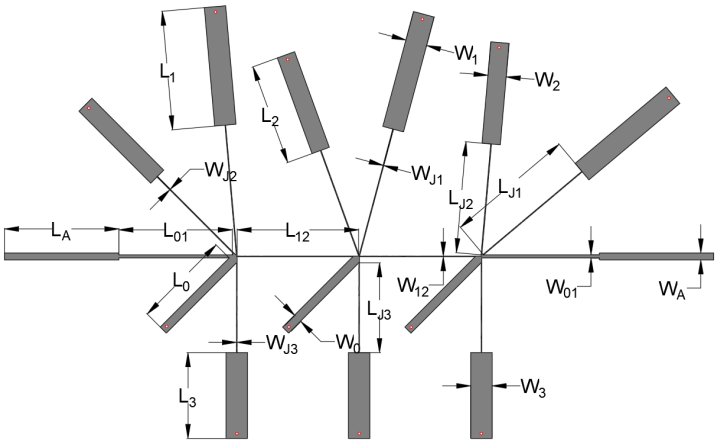

(a)

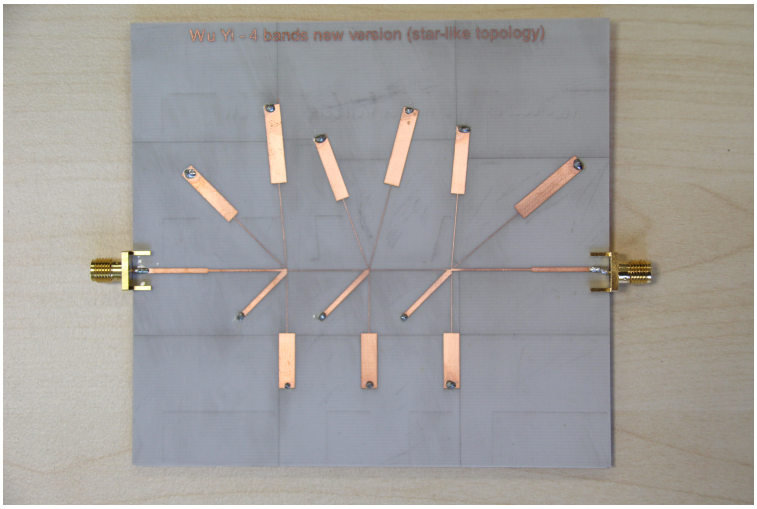

(b)

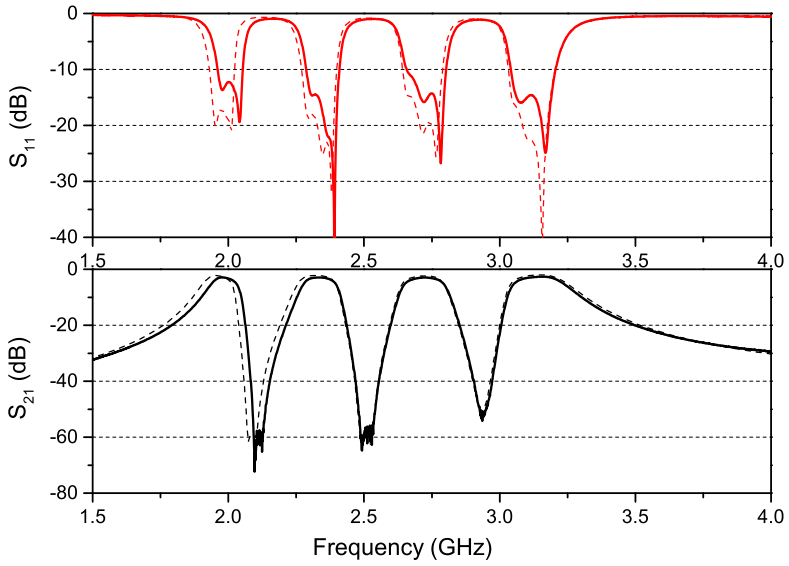

(c)

Figure 3.9 – Layout of the fabricated quad-band band-pass filter (a); the photo of the fabricated quad-band filter (b); EM-simulated (dotted lines) and measured (solid lines) S-parameters of the quad-band band-pass filter (c).

$b_1 = 6.381$, $b_2 = 5.697$ and $b_3 = 8.066$. An ideal L-C structure implementation is then made as in the tri-band case and all the resonators are again fixed identical by taking all the C_i^{LP} equal. All the resonator component values and J-inverter ones are provided in Appendix 7.3 (see table 7.1). As shown in Fig. 3.2.1, the four obtained bands are, as previously, in perfect agreement with the specifications.

This filter is also realized in microstrip technology. Fig. 7.2 presents the layout of the fabricated quad-band band-pass filter. All lengths and lines of resonators and inverters are given in appendix. The quad-band filter is 98.247×70.597 mm^2 without taking into account the two 50 Ω access lines. Fig. 3.9(c) presents the simulated and measured frequency responses of the fabricated quad-band band-pass filter. The picture is also presented in Fig. 3.9(b).

Another quad-band case (see Appendix 7.3) with equal bandwidth was published in [51] and illustrated in Fig. 7.1(a) with a photo shown in Fig. 7.1(b). Good agreement has also achieved between simulation and measurement. Fig. 3.9 presents the EM-simulated and measured frequency responses of the fabricated quad-band band-pass filter. As in the tri-band case, both responses are are in near perfect agreement. The measured RL are 12.1 dB, 14.2 dB, 14.2 dB, 14.3 dB from the first to the fourth pass-band and the measured IL are 2.90 dB, 2.94 dB, 2.95 dB, 2.65 dB respectively. Very good isolation are here again achieved between all the pass-bands.

Quint-band band-pass filter

In the same way as for the two previous cases, one can derive the equations of the resonant angular frequencies and the slope parameters for the quint-band band-pass filters as functions of the low and high cut-off angular frequencies by taking $N = 5$ in (3.14) to (3.23). The resulting equations are presented in Appendix 7.2 for a sake of brevity.

The arbitrary specifications proposed here to design an example of quint-band band-pass filter are:

1. Pass-band 1: 2.00 GHz-2.10 GHz (BW: 100 MHz);
2. Pass-band 2: 2.30 GHz-2.38 GHz (BW: 80 MHz);
3. Pass-band 3: 2.60 GHz-2.69 GHz (BW: 90 MHz);
4. Pass-band 4: 2.88 GHz-2.98 GHz (BW: 100 MHz);
5. Pass-band 5: 3.20 GHz-3.30 GHz (BW: 100 MHz).

They leads to the following resonant frequencies and slope parameters: $f_0 = \omega_0/2\pi = 2.548$ GHz, $f_1 = \omega_1/2\pi = 2.178$ GHz, $f_2 = \omega_2/2\pi = 2.480$ GHz, $f_3 = \omega_3/2\pi = 2.797$ GHz, $f_4 = \omega_4/2\pi = 3.137$ GHz, $b_0 = 5.421$, $b_1 = 6.075$, $b_2 = 5.735$, $b_3 = 8.323$ and $b_4 = 10.050$. An ideal L-C quint-band band-pass filter is also implemented to validate the method. The resonator component and J-inverter values are given in table 3.3 and the frequency responses shown in Fig. 3.11.

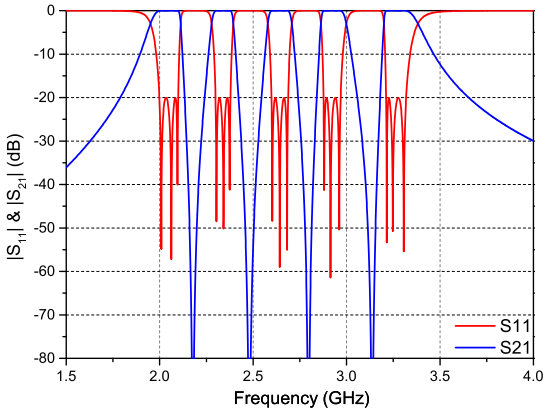

Figure 3.10 – Ideal frequency response of the specified quint-band band-pass filter.

Table 3.3 – Component values of the ideal L-C quint-band third-order band-pass filter.

Resonators ($i \in [1;3]$)		
$L_0^{(i)} = 1.602$ nH	$L_1^{(i)} = 1.874$ nH	$L_2^{(i)} = 1.645$ nH
$L_3^{(i)} = 1.388$ nH		$L_4^{(i)} = 1.241$ nH
$C_0^{(i)} = 2.436$ pF	$C_1^{(i)} = 2.850$ pF	$C_2^{(i)} = 2.502$ pF
$C_3^{(i)} = 2.333$ pF		$C_4^{(i)} = 2.080$ pF
$J_1^{(i)} = 0.0070$ S		$J_2^{(i)} = 0.0072$ S
$J_3^{(i)} = 0.0069$ S		$J_4^{(i)} = 0.0064S$
Inverters ($J_{i,i+1}$)		
$J_{01} = J_{34} = 0.013$ S		$J_{12} = J_{23} = 0.0069$ S

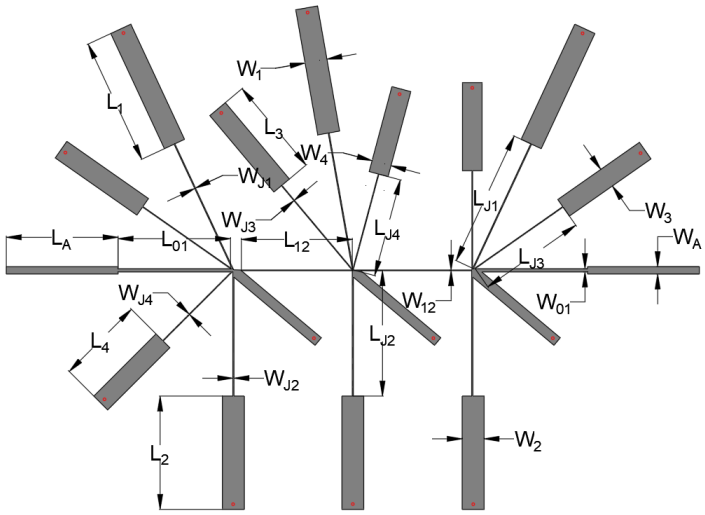

(a)

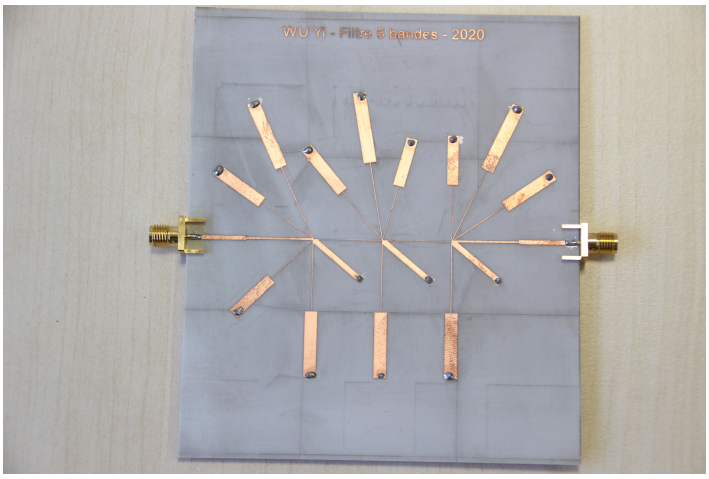

(b)

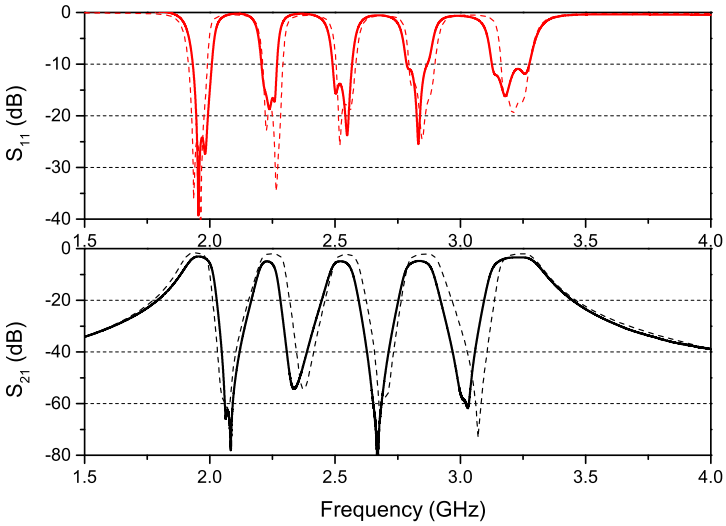

(c)

Figure 3.11 – Layout of the fabricated quint-band band-pass filter (a); the photo of the fabricated quint-band filter (b); EM-simulated (dotted lines) and measured (solid lines) S-parameters of the quint-band band-pass filter (c).

The layout of the quint-band filter is presented in Fig 3.11(a) with its associated dimension in table 3.4. A picture of the fabricated filter, using the same materials as previously, is shown in Fig. 3.11(b). Fig. 3.11(c) presents the simulated and measured frequency responses of the fabricated quint-band band-pass filter. Simulations and measurements are in a good correlation, except a slight frequency shift in the higher transmission zeros. This can be explained by the low-cost technology process which implies in particular that the vias were made by hand. The measured RL are 24.8 dB, 17.5 dB, 13.9 dB, 10.9 dB, 10.8 dB from the first to the fifth band and the measured IL are 3.01 dB, 4.95 dB, 4.98 dB, 4.75 dB, 3.45 dB, respectively. Very good isolation are again achieved between all the pass-bands.

Table 3.4 – Microstrip quint-band third-order band-pass filter: length and width dimensions *(in mm)*.

Resonators			
$L_0 = 17.73$	$L_1 = 19.50$	$L_2 = 17.40$	
$W_0 = 1.55$	$W_1 = 3.44$	$W_2 = 3.36$	
$L_3 = 15.33$		$L_4 = 13.50$	
$W_3 = 3.10$		$W_4 = 3.01$	
$L_{J1} = 21.40$	$L_{J2} = 19.30$	$L_{J3} = 17.05$	$L_{J4} = 15.33$
$W_{J1} = 0.14$	$W_{J2} = 0.17$	$W_{J3} = 0.10$	$W_{J4} = 0.10$
Inverters			
$L_{01} = 17.71$		$L_{12} = 18.34$	
$W_{01} = 0.50$		$W_{12} = 0.11$	

3.2.2 Sixfold-band band-pass filters or beyond

For sixfold-band cases and beyond, it's impossible to determine analytically the resonant frequencies of the stop-band resonators using (3.16) because the degree of this equation. So a numerical resolution of this equation is needed, but only of this one. The direct frequency mapping method presented previously in this chapter is so possible to design multiband band-pass filter with six bands or more.

Nevertheless, the implementation used for the previous examples becomes more and more difficult with the increase of the number of bands. Indeed, as the number of pass-bands increase, all the needed short-ended microstrip branches are difficult to map in a single-layer because two major challenges. The first one is that at the junction of band-pass and band-stop resonators, too many branches will lead to the discontinuity of impedance, thereby affecting the performance of the filter. The second one is the adjacent band-stop resonators will couple with each other, which will affect the stop-band performance.

To cope with these challenges, a multilayer configuration is proposed putting some stubs in another layer. The configuration investigated here is presented in Fig. 3.14 in the case of a sixfold-band filter. The top and bottom layers own the same characteristic $h_1 = h_2 = 0.508$ mm, $\varepsilon_r = 3.55$ and $\tan\delta = 0.004$. Both layers are connected to the ground (centered between

these two conductive layers) by copper vias. They are also linked to each other by copper vias through the common ground. The two substrates are sticked by a prepreg layer ($h_4 = 0.2$ mm, $\varepsilon_r = 3.52$ and $\tan\delta = 0.004$). The diameter of the copper pillar is 0.4 mm. The layouts of the top layer and the bottom layer are shown in Fig. 3.14(a) and Fig. 3.14(b), respectively. The dimensions of the filter are shown in Fig. 7.2 and all the values are available in Appendix (Table. 7.3) in the case of the following arbitrary specifications:

1. Pass-band 1: 2.00 GHz-2.10 GHz (BW: 100 MHz);
2. Pass-band 2: 2.30 GHz-2.38 GHz (BW: 80 MHz);
3. Pass-band 3: 2.58 GHz-2.67 GHz (BW: 90 MHz);
4. Pass-band 4: 2.85 GHz-2.96 GHz (BW: 100 MHz);
5. Pass-band 5: 3.10 GHz-3.22 GHz (BW: 100 MHz);
6. Pass-band 6: 3.50 GHz-3.58 GHz (BW: 100 MHz).

The resonant frequencies numerically determined are $f_0 = 2.645$ GHz, $f_1 = 2.170$ GHz, $f_2 = 2.460$ GHz, $f_3 = 2.755$ GHz, $f_4 = 3.050$ GHz and $f_5 = 3.451$ GHz. The slope parameters are analytically determined and are $b_0 = 4.560$, $b_1 = 6.601$, $b_2 = 6.968$, $b_3 = 9.114$, $b_4 = 15.840$, $b_5 = 12.740$ respectively. The theoretical responses are shown in Fig. 3.12. The simulation results obtained using CST software with the proposed multilayer is plotted in Fig. 3.14(c). We can observe that the return losses are good for all the pass-bands, high rejection level are also achieved for all the stop-bands. However, the insertion losses are relatively large as the frequencies increase. Moreover, the largest insertion loss about 8.1 dB can be observed in the last pass-band. It may because the introduction of via-connectors between the top and bottom layers on the one hand and the emergence of the cavity between the two ground layers on the other hand.

Finally, due to a lack of time to optimize this sixfold-band filter and additional constraints imposed by the prospective manufactured (necessity of two ground metal layers from either side of the prepreg layer), we had chosen not to realize this filter. Nevertheless, even if such a solution needs a relatively important design time, we think it is a very interesting solution in order to develop multiband filters with a high number of bands in planar technologies.

3.3 Extension to other technological configurations

3.3.1 Implementation of star-like multiband filters with coupled structures

In the above sections, we mainly focus on direct synthesis technology for MBPFs with the use of resonators' slope parameters and implementation using stubs in a star-like topology. However, coupled structures are also often used to design MBPFs because of their compact size, high-quality factors and easy-integrated characteristics. The frequency transformation method

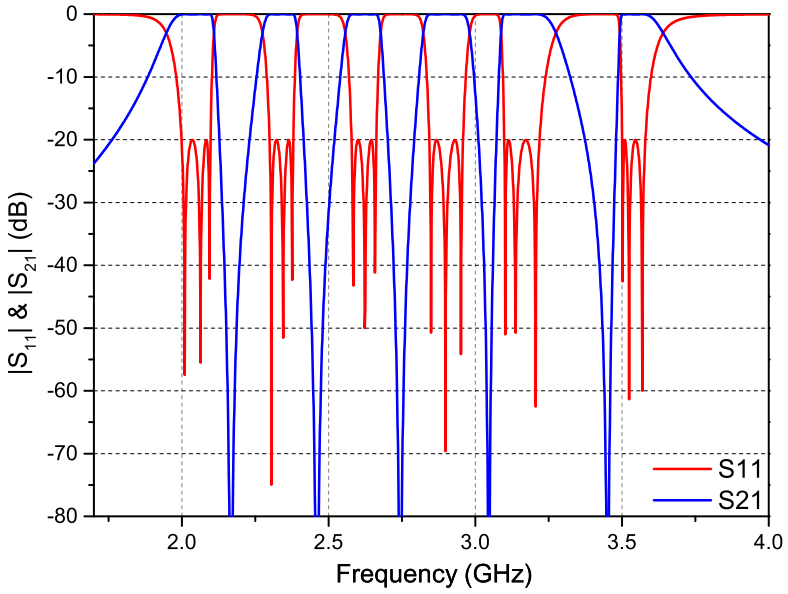

Figure 3.12 – Theoretical responses of the proposed sixfold-band band-pass filter with multilayer configuration.

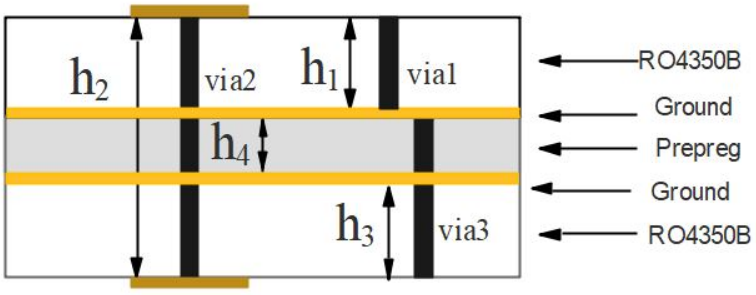

Figure 3.13 – Multilayer PCB layout.

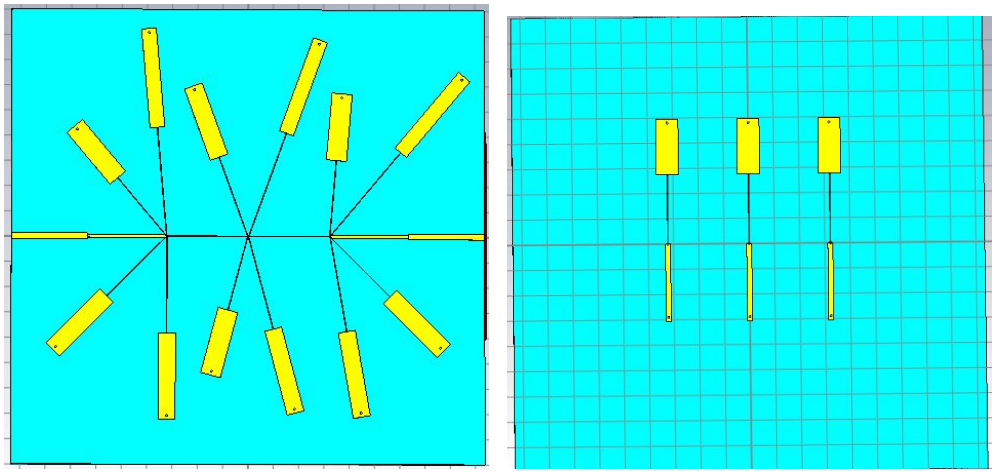

(a) (b)

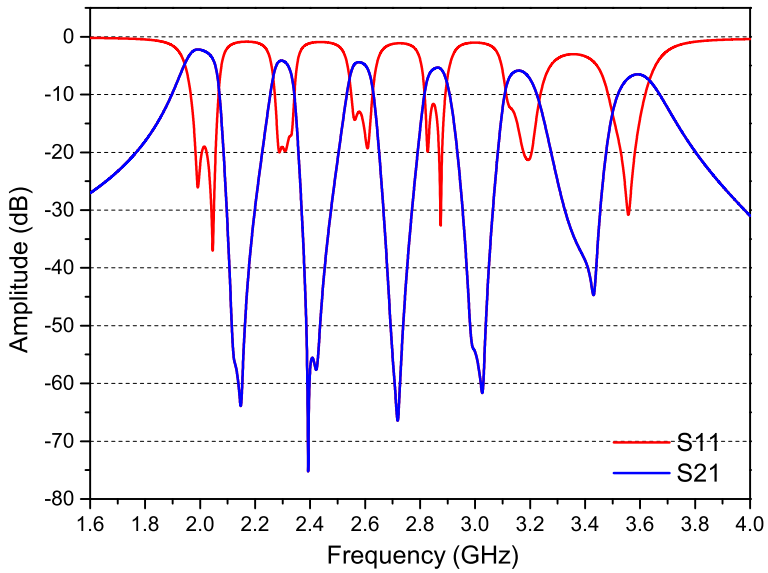

(c)

Figure 3.14 – Layouts and responses of the proposed sixfold-band band-pass filter: on the top layer (a) the first, second, third and fourth band-stop resonators; on the bottom layer (b) the fifth band-stop resonators and the band-pass ones; (c) EM simulated S-parameters.

we propose in this thesis can be applied to these coupled structures using waveguides, microstrip, and other technologies.

To do that, we need to determine the coupling coefficients and the quality factors between the consecutive resonator and/or source or load. For a given network topology, there is an infinite number of combinations of slope parameters and g_i values (the capacitance values in low-pass domain, associated to the chosen approximation function and the return loss level) that can be chosen to achieve the same filtering response if we reduce or expand all coupling coefficients by the same multiple. So, if all the slope parameters in the above-mentioned star-like topology with directly synthesis methods are taken equal to 1, we will have $\beta_0^{(i)} = \beta_k^{(i)} = 1$ with $i\ in[1; M]$ and $k\ in[1; N-1]$ where M is the filter order and N the number of bands. We can also normalize the admittance of source and load $G_s = G_l = 1$. Equations (3.45)-(3.48) are then scaled to:

$$J_{01} = \sqrt{\frac{G_S \beta_0^{(1)}}{b_0 g_0 g_1}} = \sqrt{\frac{1}{b_0 g_0 g_1}} = m_{01}\sqrt{\frac{1}{b_0}} \tag{3.49}$$

$$J_{i,i+1} = \frac{1}{b_0}\sqrt{\frac{\beta_0^{(i)}\beta_0^{(i+1)}}{g_i g_{i+1}}} = \frac{1}{b_0}\sqrt{\frac{1}{g_i g_{i+1}}} = \frac{m_{i,i+1}}{b_0} \tag{3.50}$$

$$J_{M,M+1} = \sqrt{\frac{G_L \beta_0^{(M)}}{b_0 g_M g_{M+1}}} = \sqrt{\frac{1}{b_0 g_M g_{M+1}}} = m_{M,M+1}\sqrt{\frac{1}{b_0}} \tag{3.51}$$

$$J_k^{(i)} = \sqrt{\frac{\beta_0^{(i)}\beta_k^{(i)}}{b_0 b_k}} = \sqrt{\frac{1}{b_0 b_k}} \tag{3.52}$$

where $m_{i,j}$ $(i, j \in [0; M+1])$ are the normalized coupling coefficients in the low-pass domain. The different combinations of parameters result in the same electrical performance for the MBPFs, and this is well proved in [52]. For a filter with a specified return loss level, the g_i values can be looked up in book [20]. For example, for a second order filter with a Chebyshev approximation and 20 dB return loss, $g_0 = 1$, $g_1 = 0.6648$, $g_2 = 0.5445$, $g_3 = 1.2210$, which corresponds to $m_{01} = m_{23} = 1.2264$, $m_{12} = 1.6620$.

We an then define the coupling coefficients between two consecutive band-pass resonators as defined in Fig. 3.3.1 in a triple-band case as:

$$K_{i,i+1} = \frac{m_{i,i+1}}{b_0} \quad \text{with } i \in [1; M-1] \tag{3.53}$$

the last resonator and the load in the other hand are defined from the external at the input and

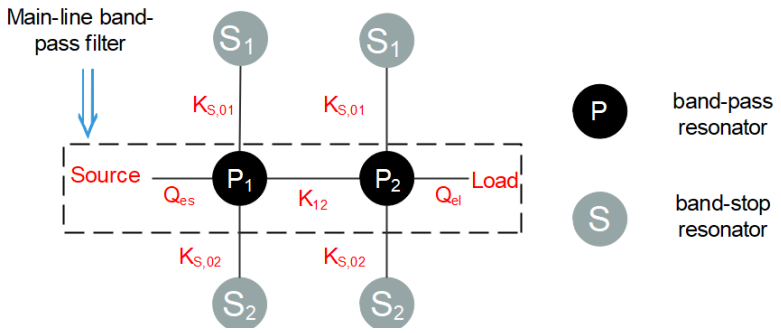

Figure 3.15 – Topology of a coupled-lines star-like multiband filter: case of a triple-band filter.

Q_{el} at the output. They can be expressed as:

$$Q_{es} = b_0 G_s = \frac{b_0}{m_{01}^2} = b_0 g_0 g_1 \tag{3.54}$$

$$Q_{el} = b_0 G_l = \frac{b_0}{m_{M,M+1}^2} = b_0 g_M g_{M+1} \tag{3.55}$$

In the same way, the coupling coefficients inside a multiband resonator between the band-pass resonator and the k^{th} band-stop resonators can be written as:

$$K_{S,0k} = \frac{1}{\sqrt{b_0 b_k}} \quad \text{with } k \in [1; N-1] \tag{3.56}$$

For practical implementation, in this thesis, we only focus on microstrip technology. In order to avoid using too many metalized-vias, we use half-wavelength resonators as band-pass and band-stop resonators, as we use quarter-wavelength resonators with vias previously. For such coupled structures, the coupling coefficients are achieved by adjusting the coupling distance between the resonators while for direct synthesis method the couplings are achieved by quarter-wavelength J inverters. The coupling coefficients can be extracted with EM software. For our cases, all the simulations are implemented with ADS software from Keysight Technologies. The extracted methods are well explained in [20] and [52].

The external quality factors Q_{es} and Q_{el}, which are equal in our case, can be calculated directly by dividing the 3dB bandwidth Δ_f and the centre frequency f_0 as follows (see. Fig. 3.16(a)):

$$Q_{es} = Q_{el} = \frac{f_0}{\Delta_{f_{3dB}}} \tag{3.57}$$

The coupling between two adjacent resonators can be extracted considering them identical

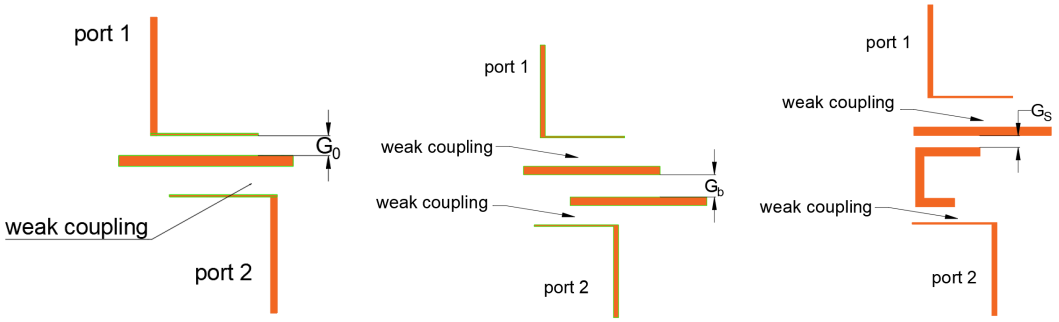

(a) (b) (c)

Figure 3.16 – Arrangements for extracting the coupling coefficients: for extracting the external quality factor (a); for extracting the coupling coefficient between two band-pass resonators (b); for extracting the coupling coefficient between band-pass and band-stop resonators (c).

The coupling coefficient is then:

$$K_{i,i+1} = \frac{f_{i+1}^2 - f_i^2}{f_{i+1}^2 + f_i^2} \tag{3.58}$$

where f_i and f_{i+1} are the resonant frequencies of resonators i and $i+1$ respectively when the two band-pass resonators are coupled (see. Fig. 3.16(b)).

Finally, the coupling coefficient between band-pass and band-stop resonators of a individual multiband resonator can be expressed as:

$$K_{0,k} = \frac{1}{2}\left(\frac{f_{r2}}{f_{r1}} + \frac{f_{r1}}{f_{r2}}\right)\sqrt{\left(\frac{f_{p2}^2 - f_{p1}^2}{f_{p2}^2 + f_{p1}^2}\right) - \left(\frac{f_{r2}^2 - f_{r1}^2}{f_{r2}^2 + f_{r1}^2}\right)} \tag{3.59}$$

where f_{p1} and f_{p2} are the lower and higher resonant frequencies of the two coupled resonators while f_{r1} and f_{r2} are their self-resonant frequencies in each resonant mode without coupling.

Fig. 3.16 shows the layouts of the coupling schematic for extracting the Q factor (a) and the coupling coefficients between two band-pass resonators (b) and between band-pass and band-stop resonators (c). Fig. 3.17 shows the associated S-parameters responses. Once we fix the coupling length (calculated according to the obtained resonant frequencies from the frequency transformation synthesis), we can only change the gaps G_0, G_b and G_S respectively to extract the needed values.

3.3.2 Examples of star-like multiband filters implemented with coupled structures

Two examples of multiband band-pass filters based on a star-like topology and implemented with coupled lines are presented here: a triple- and a quad-band filter. Both initial low-pass

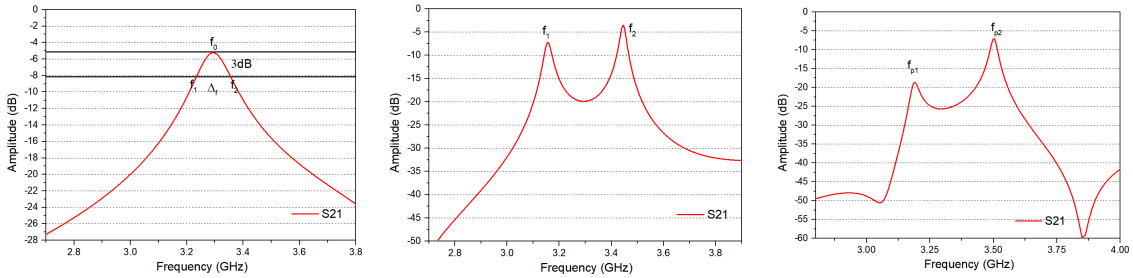

Figure 3.17 – S-parameter responses used for extracting the external quality factor (a), the coupling coefficient between band-pass resonators (b) and the coupling coefficient between band-pass and band-stop resonators (c).

prototypes are chosen as 2$^{\text{nd}}$-order Chebyshev filters with 20 dB return loss. The coupling coefficients are $m_{01} = m_{23} = 1.2264$, $m_{12} = 1.6620$ respectively as determined in the previous section.

For each example, once again, we propose arbitrary specifications in terms of low and high cut-off frequencies and we determine the resonant frequencies and slope parameters using the method proposed in Section 3.1.2. The two multiband band-pass filters were fabricated in microstrip technology on Rogers 6010 substrate with a thickness $h = 1.27$ mm, a relative permittivity $\varepsilon_r = 10.2$ and a loss tangent $\tan\delta = 0.0023$, associated with a double-sided copper layer with a thickness of 18 μm and a conductivity of 5.8×10^7 S.m^{-1}. For each resonator, the band-pass and the band-stop parts were implemented using half-wavelength open-ended stubs resonators with the same line width of 1 mm. All prototypes were simulated and optimized using ADS software from Keysight Technologies©. The fabrication of the circuits were made by laser engraving using a LPKF Protolaser U4.

Example 1: tri-band coupled-lines filter

For this first example of a tri-band filer, the three pass-bands were chosen as follow:

1. Pass-band 1: 3.00 GHz-3.20 GHz (BW: 200 MHz);
2. Pass-band 2: 3.30 GHz-3.40 GHz (BW: 100 MHz);
3. Pass-band 3: 3.50 GHz-3.60 GHz (BW: 100 MHz).

The resulting resonant frequencies and slope parameters are: $f_0 = \omega_0/2\pi = 3.258$ GHz, $f_1 = \omega_1/2\pi = 3.258$ GHz, $f_2 = \omega_2/2\pi = 3.471$ GHz, $b_0 = 8.145$, $b_1 = 25.46$ and $b_2 = 31.69$. The Q factors and coupling coefficients are then Q_{es}=Q_{el}=5.4148, $K_{1,2} = 0.1503$, $K_{01} = 0.06944$, $K_{02} = 0.06224$. The theoretical response of this filter is shown in Fig. 3.18.

Fig. 3.19(a) shows the layout of the fabricated filter with dimension details in Table 4.2. Fig. 3.19(b) is the photography of the circuit. Fig. 3.19(c) presents the simulated and measured

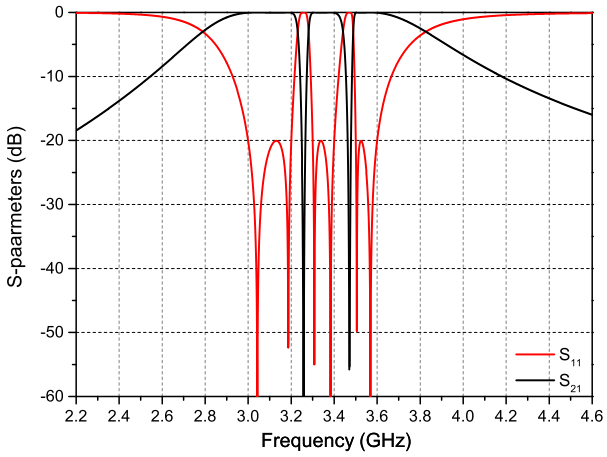

Figure 3.18 – Theoretical responses of the designed tri-band coupled filter.

Table 3.5 – Dimensions of the tri-band band-pass filters implemented with coupled structures.

Symbol	Values (mm)	Symbol	Values (mm)
L_0	3.60	L_g	9.02
L_{01}	7.60	L_{02}	4.60
L_{03}	7.0	L_{11}	3.40
L_{12}	7.00	L_{13}	8.00
L_{14}	2.10	L_{21}	23.40
L_m	3.16	W_{21}	0.12
w_0	0.60	w_g	0.20
w_{s1}	0.16	w_{s2}	0.36
w_{s3}	0.16		

frequency responses of the fabricated tri-band band-pass filter. Simulations and measurements are in a good correlation, except a slight frequency shift of the second transmission zero. This can be explained by the low-cost technology process which could imply some changes in the characteristics of the high permittivity PCB. The measured RL are 15.3 dB, 10.2 dB, 16.4 dB from the first to the third band and the minimum insertion losses are 1.75, 3.86 and 2.03 dB at the center frequencies of each pass-band, respectively. Good isolation (better than 27 dB) are achieved for both stop-bands.

Example 2: quad-band coupled-lines filter

In this second example of quad-band coupled-lines filter, in the same way, we specify arbitrary bandwidths as follow:

1. Pass-band 1: 3.05 GHz-3.12 GHz (BW: 70 MHz);
2. Pass-band 2: 3.22 GHz-3.30 GHz (BW: 80 MHz);

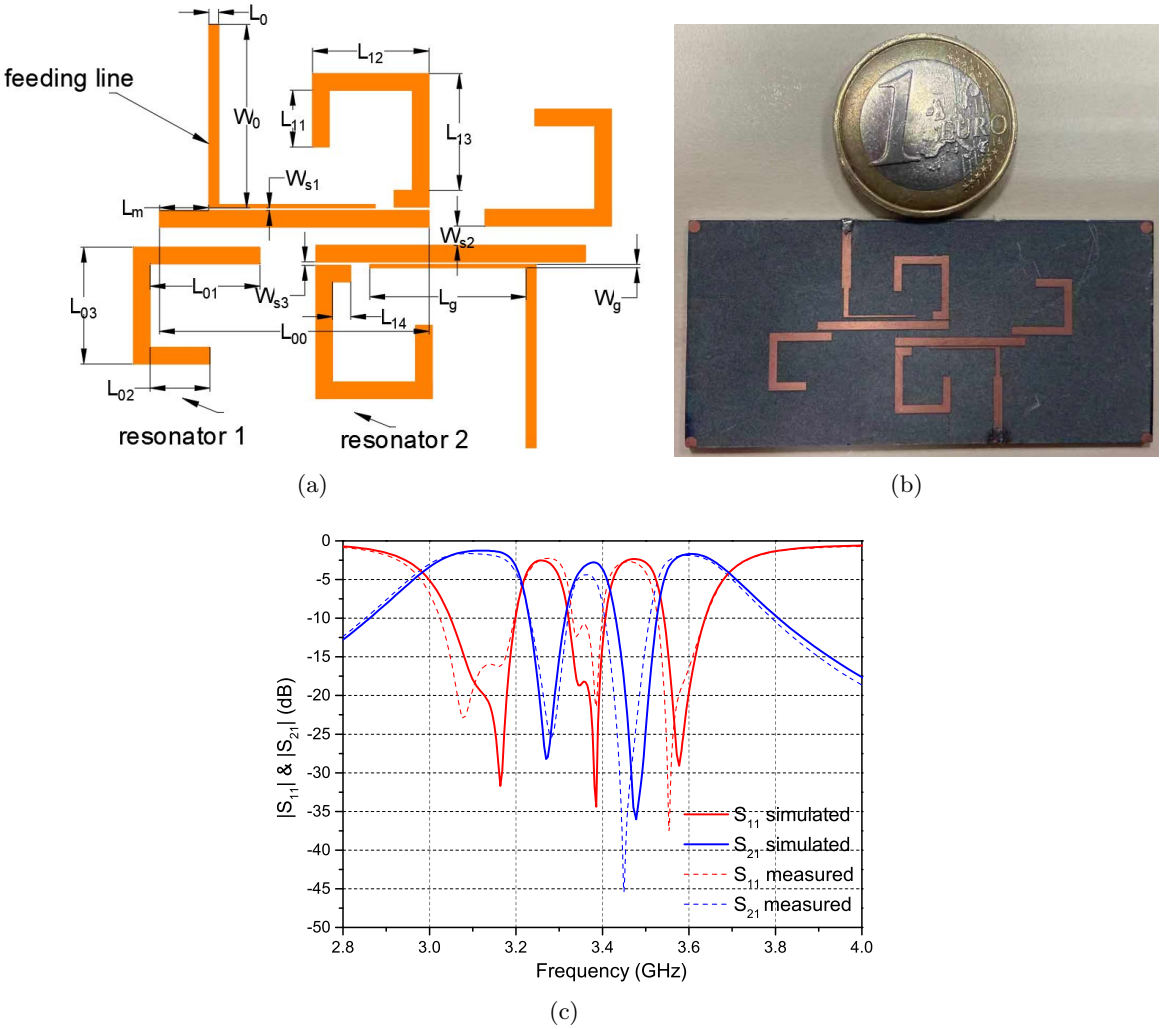

Figure 3.19 – Layout (a) and picture (b) of the fabricated tri-band band-pass filter; associated EM-simulated (solid lines) and measured (dotted lines) S-parameters (c).

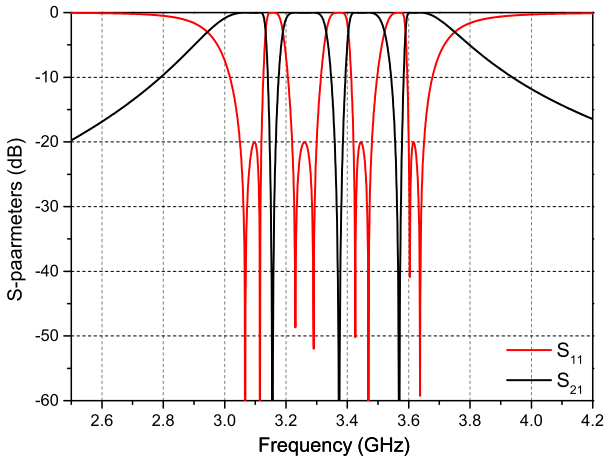

Figure 3.20 – Theoretical responses of the designed quad-band coupled filter.

3. Pass-band 3: 3.42 GHz-3.48 GHz (BW: 60 MHz);
4. Pass-band 4: 3.60 GHz-3.65 GHz (BW: 50 MHz).

The resulting resonant frequencies and slope parameters are: $f_0 = \omega_0/2\pi = 3.310$ GHz, $f_1 = \omega_1/2\pi = 3.156$ GHz, $f_2 = \omega_2/2\pi = 3.373$ GHz, $f_3 = \omega_3/2\pi = 3.569$ GHz, $b_0 = 12.73$, $b_1 = 22.09$, $b_2 = 17.51$ and $b_3 = 22.78$. The Q factors and the coupling coefficients are then Q_{es}=Q_{el}=8.4637, $K_{1,2}$=0.1306, $K_{01} = 0.05963$, $K_{02} = 0.06698$ and $K_{03} = 0.05872$. The theoretical response of this quad-band filter is shown in Fig. 3.20.

The layout of the quad-band filter is presented in Fig. 3.21(a) with its associated dimensions in Table 4.3. A picture of the fabricated filter is shown in Fig. 3.21(b). Fig. 3.21(c) presents its simulated and measured frequency responses. Both are once again in good correlation. The measured RL are 20.0 dB, 15.2 dB, 15.4 dB, 18.3 dB, from the first to the fourth band and the minimum insertion losses in the pass-band are 1.36, 2.18, 2.97 and 1.78 dB, respectively. The isolation is better than 20 dB for all the stop-bands.

3.4 Discussion

As shown in the synthesis process proposed in this chapter, a multiband response could be produced simply by replacing the low-pass resonators of any prototype with the transformed star-like circuits. Each sub-band will become the frequency-translated and bandwidth-scale equivalents of the original prototype. Therefore, if our low-pass filter have transmission zeros (TZs), the multiband version will have additional TZs between each band. For instance, we provide here an example of the synthesis of a multiband elliptic filter with a quint-band response. We consider a 4^{th}-order filter with an elliptic approximation (23 dB RL with normalized TZs at $\pm 2.2j$). The specifications for this example are the followings:

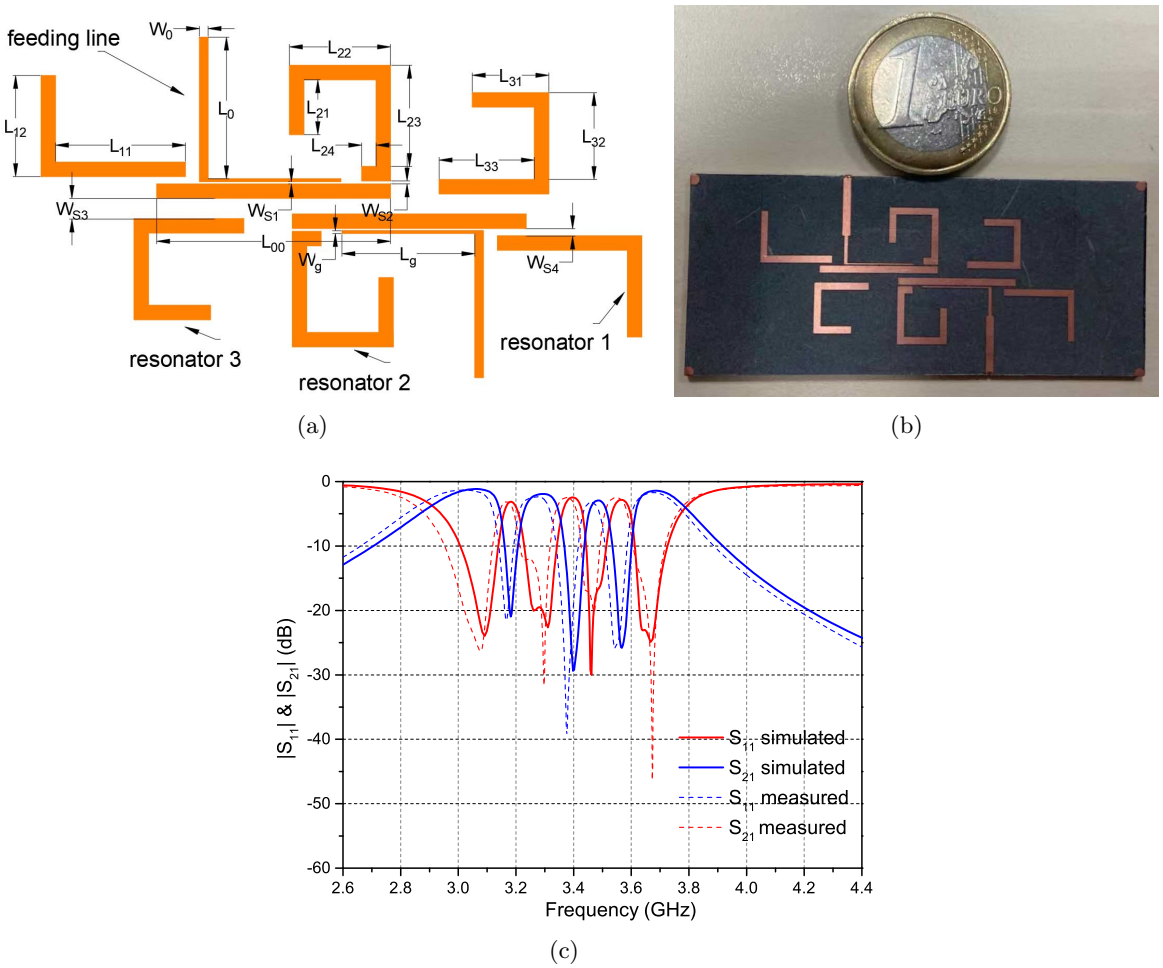

Figure 3.21 – Layout (a) and picture (b) of the fabricated quad-band band-pass filter; associated EM-simulated (solid lines) and measured (dotted lines) S-parameters (c).

Table 3.6 – Dimensions of the quad-band band-pass filters implemented with coupled structures.

Symbol	Values (mm)	Symbol	Values (mm)
L_0	3.00	L_g	9.02
L_{11}	10.0	L_{12}	7.20
L_{21}	5.0	L_{22}	7.0
L_{23}	7.95	L_{24}	1.05
L_{31}	5.25	L_{32}	5.0
L_{33}	6.60	W_0	0.60
w_0	0.20	w_g	0.12
w_{21}	0.12	w_{s1}	0.17
w_{s2}	0.22	w_{s3}	1.39
w_{s3}	1.39	w_{s4}	0.37

1. Pass-band 1: 3.00 GHz-3.10 GHz (BW: 100 MHz);
2. Pass-band 2: 3.30 GHz-3.40 GHz (BW: 100 MHz);
3. Pass-band 3: 3.60 GHz-3.70 GHz (BW: 100 MHz);
4. Pass-band 4: 3.90 GHz-4.00 GHz (BW: 100 MHz);
5. Pass-band 5: 4.20 GHz-4.30 GHz (BW: 100 MHz).

The resonating frequencies and slope parameters can be easily obtained once again using the generalized formulas presented in Section 3.1.2. Fig. 3.22 shows the ideal circuit response for this quint-band elliptic filter. The additional TZs clearly appear on either side of each band as expected. The stop-band region between each pass-band is thus improved.

In addition to the elliptic function filter mentioned above, we also give an example of a Butterworth filter. This type of filter is characterized by the maximally flat response as shown in [20]. Here, we build a tri-band band-pass filter based on Butterworth low-pass prototype filters ($g_0 = g_4 = 1.0$, $g_1 = g_3 = 1.0$, $g_2 = 2.0$) with a classical attenuation L_{Ar} = 3-dB at Ω_c with the following specifications:

1. Pass-band 1: 1100 MHz – 1200MHz (3-dB BW: 100 MHz);
2. Pass-band 2: 1300 MHz – 1400MHz (3-dB BW: 100 MHz);
3. Pass-band 3: 1500 MHz – 1600MHz (3-dB BW: 100 MHz).

The response for the proposed tri-band filter is presented in Fig. 3.4 with a zoom in Fig. 3.4 around 3 dB to well see the cut-off frequencies.

More generally, using our proposed transform function, we always assume that lower cut-off angular frequencies ω_{L_i} and the upper cut-off angular frequencies ω_{H_i} ($i \in [1; N]$) are respectively mapped to -1 and +1 in the Ω low-pass normalized domain, which presents a symmetric behaviour. This implies that only transfer functions that are symmetric in the low-pass domain

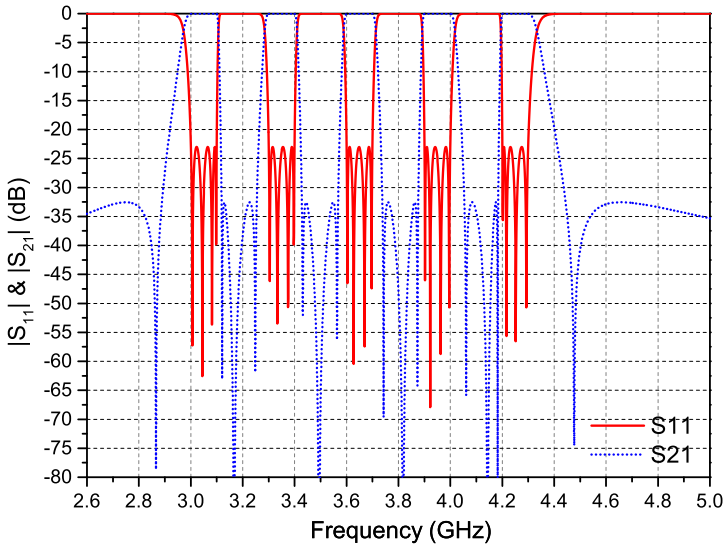

Figure 3.22 – Ideal frequency response of the specified quint-band elliptic band-pass filter.

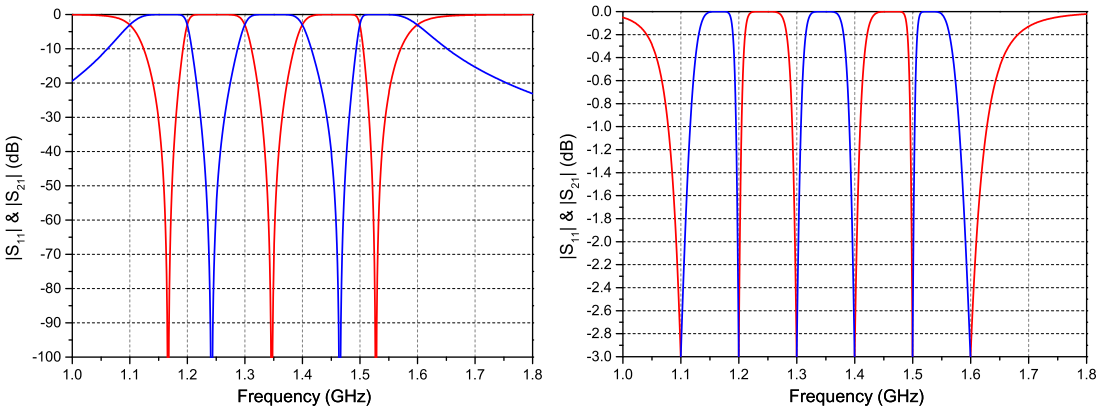

(a) Filter response.

(b) Return loss at Ω_c.

Figure 3.23 – Theoretical response for the tri-band Butterworth band-pass filter (a) and focus on the 3 dB region (b).

can be used in this method. Chebyshev, Butterworth and elliptic filters have all symmetrical structures where the symmetry is defined as $g_0 = g_{n+1}$, $g_1 = g_n$, $g_2 = g_{n-1}$, etc., in low-pass normalized prototypes. There are all therefore compatible with our proposed synthesis method.

For Gaussian low-pass prototype (flat-group-delay), filters with order $n = 1$ are identical to the first-order Butterworth low-pass prototype and can also be synthesized with this method. Gaussian filters with order $n \geq 2$ are structurally asymmetrical as discussed in [20]. It is therefore impossible to synthesize multiband Gaussian filter with this method. Nevertheless, flat group-delay can also be obtained with symmetrical structures using cross-coupling as presented in the case of single-band filters in [53, 54].

3.5 Conclusion

In this chapter, we discuss the synthesis of MBPFs with a generalized frequency transformation methods. A rigorous mathematical analysis process is presented to obtain the generalized transform function for an arbitrary number of pass-bands, extending the frequency transformation proposed in [18] in a dual-band case. Based on this method, tri-, quad-, and quint-band MBPFs with ideal LC circuits are synthesized and realized in microstrip technology with non-coupled structures. Such an implementation leads to a clear synthesis process and requires little optimization. Very good results are achieved between simulation and measurement. Neverthless, for such a star-like topology, it is a challenge work to implement filters with more than five bands. Indeed, on the one hand, the based band-pass filter is difficult to have a very wide-band. As the number of pass-bands increase, each pass-band will become narrow and the insertion loss will be larger and larger. On the other hand, it is difficult to map two many resonators in a single layer PCB because the limited mapping space will introduce unexpected cross-coupling effects between adjacent resonators. To cope with the second issue, multilayer structures were proposed to design MBPFs more than five pass-bands. However, the multilayer structure is also difficult to implement and it will be affected by the connection vias between layers, which may introduce losses in the filters.

To support the generality of this synthesis method, we also discuss the possibility to use coupled structures to realized multiband band-pass filters in a star-like topology. For coupled filters, there are two significant advantages. First of all, there is no need to consider the slope parameters of a single resonator, which makes the design of the filter more flexible. Secondly, due to the tight coupling structure, the miniaturization of the filter is easily to be realized. Two examples related 3 and 4 bands were developed and once again validated experimentally. Nevertheless, the synthesis process is quite time-consuming because there are many cross-coupling between the resonators. Moreover, the proposed technological implementation is difficult to be extended to an higher number of bands.

As we described above, due to the heavy loading of the band-pass resonators especially with an increasing number of bands, this direct frequency transformation method with a star-like topology could be difficult to implement. To solve this problem, a new type of transform function will be proposed in next chapter with an in-line topology.

Chapter 4

Synthesis of multiband band-pass filters with in-line topology

In chapter 3, we have mainly focused on the synthesis of multiband band-pass filter (MBPFs) with a star-like topology. The basic resonator of such a multiband filter is represented again in Fig. 4.1(a). However, as mentioned previously, the implementation of such filters is more and more difficult when the number of bands increases. Indeed, more and more stop-band resonators all connected to the same point are then needed and their mapping in a limited space could be very difficult. If some solutions were proposed at the end of Chapter 3, notably based on multilayer structures, their optimization and fabrication could be quite complex. To solve this problem, in this chapter 4, we propose to use an in-line topology as presented in Fig. 4.1(b). This topology gives more freedom to map all the resonators and enables us to achieve high number of pass-bands. This topology can also be developed starting from the frequency transformation approach but with the transfer function defined as:

$$\Omega = T^{(N)}(\omega) = b_0\left(\frac{\omega}{\omega_0} - \frac{\omega_0}{\omega}\right) - \cfrac{1}{b_1\left(\frac{\omega}{\omega_1} - \frac{\omega_1}{\omega}\right) - \cfrac{1}{b_2\left(\frac{\omega}{\omega_2} - \frac{\omega_2}{\omega}\right) - \cfrac{1}{b_3\left(\frac{\omega}{\omega_3} - \frac{\omega_3}{\omega}\right) \cdots - \cfrac{1}{b_{N-1}\left(\frac{\omega}{\omega_{N-1}} - \frac{\omega_{N-1}}{\omega}\right)}}}}, \tag{4.1}$$

In (4.1), we denote Ω the normalized angular frequency, $T^{(N)}(\omega)$ the proposed transformation function, and ω the de-normalized angular frequency. The parameters ω_0 and b_0 are the resonant angular frequency and the susceptance slope parameter of the band-pass resonators respectively and ω_k and b_k ($k \in [1; N-1]$) the ones of the band-stop resonators. As in the star-like case, these $2N$ parameters define the transformation and the objective of the synthesis process is to link them to the input parameters, i.e, the low cut-off angular frequencies ω_{L_i} and the high cut-off angular frequencies ω_{H_i} ($i \in [1; N]$) of the N bands. Starting from this transformation function, two possible approaches will be presented in Section 4.1 to determine the output parameters. The first one is directly equivalent to the one proposed in Chapter 3 in the case of the star-like topology. The second one is based on a circuit approach. This simple but powerful technique

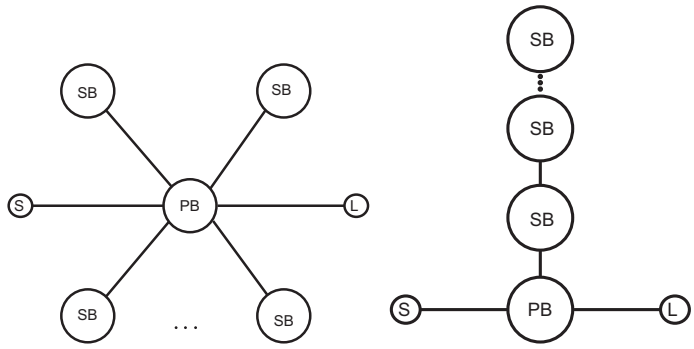

Figure 4.1 – Different topologies for multiband band-pass filter: (a) star-like topology; (b) in-line topology; PB represents pass-band resonator and SB represents stop-band resonator.

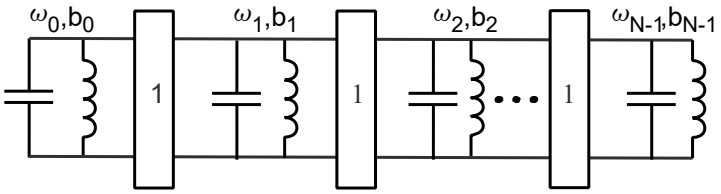

Figure 4.2 – Resulting new equivalent LC circuits with the transformation function of equation (4.1). ω_0, ω_1, ω_2, ω_{N-1} and b_0, b_1, b_2 and b_{N-1} are the resonant angle frequencies and slope parameters, respectively.

easier the synthesise of MBPFs when the number of bands increases.

In terms of equivalent circuit implementation, such a transformation function leads to a multiband band-pass resonator as the one presented in Fig. 4.2. In planar technologies, this can be translated in coupled-lines filters as it will be presented in Section 4.2. Consequently, only the knowledge of the output parameters (ω_k and b_k, $k \in [0; N-1]$) is needed and not the individual value of each capacitance and inductance.

4.1 Extraction of the output parameters

4.1.1 Extracting synthesis parameters with frequency mapping technique

The first technique proposed to synthesize an N-band band-pass filter in an in-line topology follows the same procedure as the one used in the star-like topology case but with the new transformation function given in (4.1). So, in order to obtain the design parameters, we assume once again that the lower cut-off angular frequencies for the N pass-bands ω_{L_i} ($i \in [1; N]$) map to -1 in the normalized domain Ω, while the upper ones, ω_{H_i} ($i \in [1; N]$), map to +1. Because

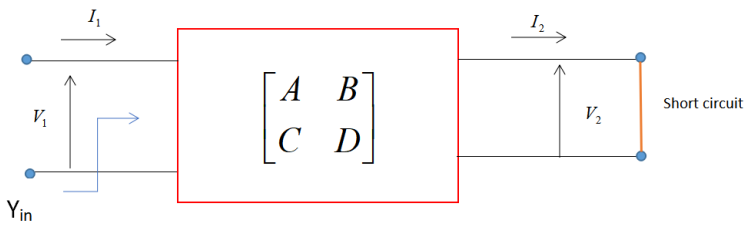

Figure 4.3 – Schematic representation of a single-port Ladder type network.

of the odd symmetry of $T(\omega)$, we obtain

$$T(-\omega_{L_i}) = T(\omega_{H_i}) = 1 \tag{4.2}$$

The high cut-off angular frequencies and the opposite of the low cut-off angular ones are therefore the zeros of the function $G(\omega)$ defined as

$$G(\omega) = T(\omega) - 1 \tag{4.3}$$

Therefore (4.3) can be expressed as

$$G^{(N)}(\omega) = -\frac{\omega^{2N} + n_{2N-1}\omega^{2N-1} + n_{2N-2}\omega^{2N-2} \cdots + n_0}{n_{2N-1}\omega^{2N-1} + n_{2N-3}\omega^{2N-3} \cdots + n_1\omega} \tag{4.4}$$

The n_p coefficients ($p \in [0; 2N-1]$) are then expressed as functions of the output parameters (ω_k and b_k ($k \in [0; N-1]$)). Then, another expression of these parameters is obtained as functions of the input parameters using the fact that these latter are the zeros of $G^{(N)}(\omega)$. These two sets of expressions of the n_p coefficients make possible to link input and output parameters and so to determine the latter according to the first. These two sets of n_p coefficients expressions are presented in Appendix 7.4 for the tri- and quad-band cases.

Therefore, this first method based on a direct frequency mapping is easy-understanding. However, for MBPFs beyond five-bands, it is challenging to obtain analytical synthesis equations, the computer-aided methods will be needed to find the design values. A second and simplest method is therefore proposed in Section 4.1.2.

4.1.2 Extracting synthesis parameters with circuit approach

The second method consists of looking the multiband resonator of Fig. 4.2 as a single-port ladder network. Based on a method presented in [19], it is possible to extract step by step all the parameters defining the transformation, i.e the resonant angular frequencies, ω_k, and the slope parameters, b_k ($k \in [0; N-1]$).

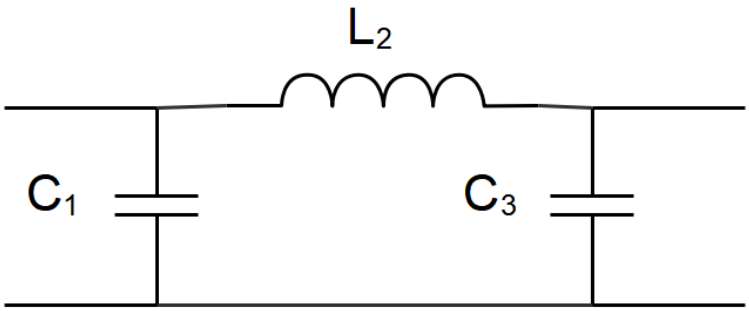

Figure 4.4 – Single port ladder type network-third-order ladder type low-pass network

To introduce this method, we first present some details and properties of a ladder network. The structure of a single-port network is shown in Fig. 4.3. V_1 and V_2 are the voltages of the input and output ports respectively, I_1 and I_2 are the corresponding currents. The variable $s = j\Omega$ is the normalized angular frequency in low-pass domain. Using a classic $[ABCD]$ matrix representation, the following equations can be obtained to link voltages and currents:

$$V_1 = A(s)V_2 + B(s)I_2 \tag{4.5a}$$

$$V_2 = C(s)V_2 + D(s)I_2 \tag{4.5b}$$

Considering a short-circuit on the output port as in Fig. 4.3, $V_2 = 0$ and then:

$$Y_{in} = \frac{I_1}{V_1} = \frac{D(s)}{B(s)} \tag{4.6}$$

In order to show the procedure of the proposed extraction method, let take the simple example of a third-order low-pass network containing only LC elements as shown in Fig. 4.4. We can easily write the ABCD matrix of this low-pass network as:

$$M_{ABCD} = \begin{bmatrix} 1 + s^2 L_2 C_3 & sL_2 \\ s(C_1 + C_3) + s^3 C_1 L_2 C_3 & 1 + s^2 L_2 C_1 \end{bmatrix} \tag{4.7}$$

The input admittance can then be expressed as:

$$Y_{in} = \frac{D(s)}{B(s)} = \frac{1 + s^2 C_1 L_2}{sL_2} \tag{4.8}$$

The first step is to extract the value of C_1, supposing that we insert the short circuit between C_1 and L_2. It means that all the LC elements behind C_1 are connected to the ground. So there is only C_1 in the circuit. In this case, the value of the first component C_1 can be extracted when

$s \to +\infty$ as following:

$$\frac{Y_{in}}{s} = \frac{D(s)}{sB(s)}\bigg|_{s\to+\infty} = \frac{1+s^2C_1L_2}{s^2L_2}\bigg|_{s\to+\infty} = C_1 \tag{4.9}$$

Once we get the values of C_1, two unknown elements of the third-order low-pass network remain, L_2 and C_3. If we premultiply the $[ABCD]$ matrix M_{ABCD} by the inverse of the C_1 $[ABCD]$ matrix, a new $[ABCD]$ matrix with L_2 and C_3 only is obtained:

$$M_{A^1B^1C^1D^1} = \begin{bmatrix} 1 & 0 \\ -sC_1 & 1 \end{bmatrix}\begin{bmatrix} 1+s^2L_2C_3 & sL_2 \\ s(C_1+C_3)+s^3C_1L_2C_3 & 1+s^2L_2C_1 \end{bmatrix} = \begin{bmatrix} 1+s^2L_2C_3 & sL_2 \\ sC_3 & 1 \end{bmatrix} \tag{4.10}$$

The same procedure can be applied here again to extract the value of L_2.

$$sY_{in}^{(1)} = s\frac{D^1(s)}{B^1(s)}\bigg|_{s\to+\infty} = \frac{1}{L_2} \tag{4.11}$$

Up to now, we have got all the values except the value of the last component, C_3. We use the same method by premultiplying $M_{A^1B^1C^1D^1}$ by the inverse $[ABCD]$ matrix of ~~the~~ L_2. So we can get the matrix $M_{A^2B^2C^2D^2}$:

$$M_{A^2B^2C^2D^2} = \begin{bmatrix} 1 & -sL_2 \\ 0 & 1 \end{bmatrix}\begin{bmatrix} 1+s^2L_2C_3 & sL_2 \\ sC_3 & 1 \end{bmatrix} = \begin{bmatrix} 1 & 0 \\ sC_3 & 1 \end{bmatrix} \tag{4.12}$$

This matrix only have one element C_3. We can use the following equation to get the ~~needed~~ value of C_3:

$$\frac{Y_{in}^{(2)}}{s} = \frac{D^2(s)}{sB^2(s)}\bigg|_{s\to+\infty} = C_3 \tag{4.13}$$

We can finally obtain all the values of the ladder network by this method, supposing that we know a priori the value of each individual $[ABCD]$ matrix or at least of each Y_{in}.

As mentioned above, our transformation function leads to the equivalent circuit shown in Fig. 4.2. The ladder network includes here normalized J-inverters but the same technique can still be applied. Indeed, extracting the inverter just inverts the input admittance as it will be shown later on the example of a tri-band resonator.

However, such ladder networks result generally into asymmetric filters. It means that the center frequencies are not always resonating at the pass-band center. Moreover, the stop-band resonant frequencies also deviate from the center resonance frequency of the based wideband BPFs. This implies that the presented immittance polynomials introduced in the above section cannot be implemented with only capacitors or inductors. In order to solve this problem,

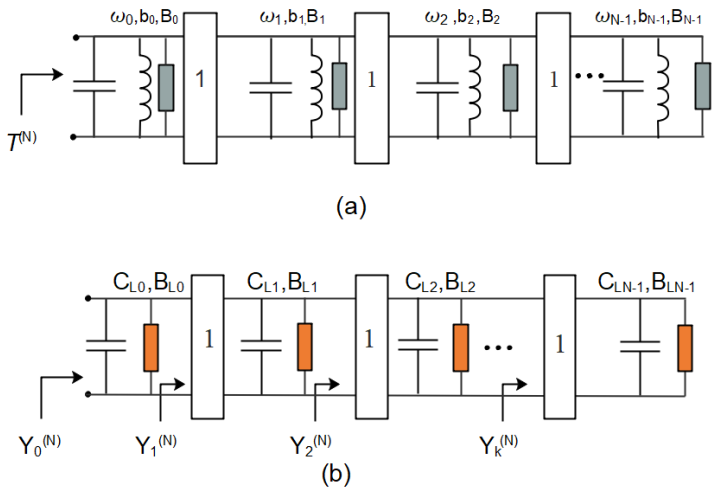

Figure 4.5 – Multiband resonators using FIRs: (a) band-pass; (b) low-pass prototype. B_k and B_{LK} ($k \in [0; N-1]$) are the FIRs in band-pass and low-pass domain.

frequency-invariant reactance elements (FIRs) are introduced to compensate for these frequency offsets as presented in Fig. 4.5(a). The addition of the FIRs at each node makes the transformation function physically realizable.

To simplify the extraction parameters process, this circuit, which corresponds to the multiband band-pass resonator in the de-normalized domain, is normalized to a multiband low-pass ladder network shown in Fig. 4.5(b). At each node level, considering the normalization/de-normalization process, the equivalent admittance can then be written as follow:

$$Y_{BP}(\omega) = jC_k\omega + \frac{1}{jL_k\omega} + jB_k = j\frac{C_{Lk}}{FBW}\left(\frac{\omega}{\omega_{BP}} - \frac{\omega_{BP}}{\omega}\right) + jB_{Lk} \tag{4.14}$$

with:

$$\omega_{BP} = \sqrt{\omega_{L_1}\omega_{H_N}} \tag{4.15}$$

$$FBW = \frac{\omega_{H_N} - \omega_{L_1}}{\omega_{BP}} = \frac{\omega_{H_N} - \omega_{L_1}}{\sqrt{\omega_{L_1}\omega_{H_N}}} \tag{4.16}$$

in the de-normalized band-pass case (Fig. 4.5(a)), ω_{BP} being the center angular frequency of the based whole pass-band and FBW its fractional bandwidth, and

$$Y_{LP}(s) = sC_{Lk} + jB_{Lk} \tag{4.17}$$

in the normalized low-pass one (Fig. 4.5(b)), with $s = j\Omega$ is the normalized frequency variable. The cut-off angular frequencies of each pass-band in the de-normalized domain (ω_{Li} and ω_{Hi}, $i \in [1; N]$) are at the same time transposed in the normalized low-pass domain using the classical

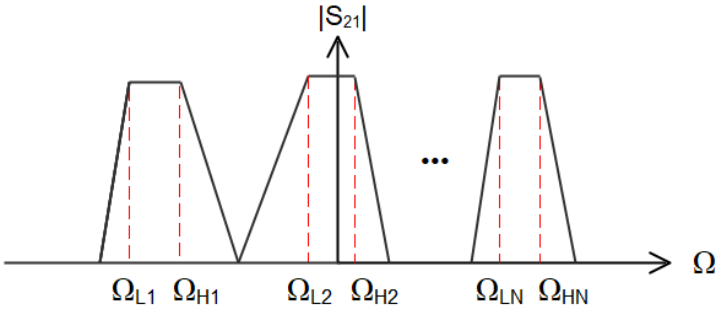

Figure 4.6 – Multiband low-pass prototype using FIR.

transformation between both domain as follow:

$$\Omega_{L_i} = \frac{1}{FBW}\left(\frac{\omega_{L_i}}{\omega_{BP}} - \frac{\omega_{BP}}{\omega_{L_i}}\right) \tag{4.18a}$$

$$\Omega_{H_i} = \frac{1}{FBW}\left(\frac{\omega_{H_i}}{\omega_{BP}} - \frac{\omega_{BP}}{\omega_{H_i}}\right) \tag{4.18b}$$

The behaviour of the ladder network in the low-pass domain is then like the one presented in Fig. 4.6. Note that the sub-bands cut-off angular frequencies then varies inside -1 and 1 with $\Omega_{L_1} = -1$ and $\Omega_{H_N} = 1$. As explained in [19], a specific frequency mapping function, $\Omega'(\Omega)$, is necessary in order to map all the cut-off angular frequencies of the multiband low-pass resonator to -1 or +1 in the normalized cut-off frequencies of a single-band prototype. In fact, in our case, this mapping function is equivalent to the admittance function, $Y_0^{(N)}$, synthesizing the ladder network presented in Fig. 4.5(b). This admittance function is:

$$Y_0^{(N)}(s) = sC_{L0} + jB_{L0} + \cfrac{1}{sC_{L1} + jB_{L1} + \cfrac{1}{sC_{L2} + jB_{L2} + \cdots \cfrac{1}{sC_{LN-1} + jB_{LN-1}}}} \tag{4.19}$$

Equation (4.19) can be rewritten as a ratio of two polynomials in the normalized frequency domain:

$$Y_0^{(N)}(\Omega) = j\frac{U(\Omega)}{V(\Omega)} = j\frac{\Omega^N + u_{N-1}\Omega^{N-1} + u_{N-2}\Omega^{N-2}\cdots + u_0}{v_{N-1}\Omega^{N-1} + v_{N-1}\Omega^{N-2}\cdots + v_0} \tag{4.20}$$

where u_i ($i \in [0; N]$) and v_i, ($i \in [0; N-1]$) are the coefficients of the numerator and denominator respectively.

To determine the value of these coefficients, it is important to note that the mapping function

alternates N times between -1 (for each Ω_{L_i}) and +1 (for each Ω_{H_i}, $i \in [1; N]$). Therefore, $2N$ linear equations are obtained as follow:

$$Y_0^{(N)}(\Omega_{L_i}) = -1 \tag{4.21a}$$

$$Y_0^{(N)}(\Omega_{H_i}) = +1 \tag{4.21b}$$

and the resolution of this equation system gives the numerator and denominator coefficients of $Y_0^N(\Omega)$ whose knowledge is the starting point of the parameters extraction method presented in this section. To apply this method, the following three principles should be keep in mind:

1. The first extracted parameter is always C_{L0}, and then B_{L0}, C_{L1}, B_{L1} until B_{LN-1}.
2. When encountering immittance inverters, it must pre-divided by 1 before extracting the next parameters.
3. When all the values are successfully extracted, all the parameters should be de-normalized to the real frequencies ranges.

Based on these principles and the knowledge of $Y_0^{(N)}(\Omega)$, we can evaluate $C_{L0}^{(N)}$ at $s = j\Omega \to +j\infty$ and then $B_{L0}^{(N)}$ as follow:

$$C_{L0}^{(N)} = \lim_{\Omega\to\infty} \frac{Y_0^{(N)}(\Omega)}{j\Omega} = \frac{1}{v_{N-1}} \tag{4.22a}$$

$$B_{L0}^{(N)} = \frac{1}{j} \lim_{\Omega\to\infty} \left(Y_0^{(N)}(\Omega) - jC_{L0}^{(N)}\Omega\right) = \frac{u_{N-1}}{v_{N-1}} - \frac{v_{N-2}}{v_{N-1}^2} \tag{4.22b}$$

Then, we can continue step-by-step in the same way using the following three equations successively from $k = 0$ to $k = N - 1$.

$$Y_{k+1}^{(N)} = Y_k^{(N)} - jC_{Lk}^{(N)}\Omega - jB_{Lk}^{(N)} \tag{4.23a}$$

$$C_{Lk}^{(N)} = \lim_{\Omega\to\infty} \frac{1}{jY_k^{(N)}\Omega} \tag{4.23b}$$

$$B_{Lk}^{(N)} = \lim_{\Omega\to\infty} \frac{1}{j}\left(\frac{1}{Y_k^{(N)}} - jC_{Lk}^{(N)}\Omega\right) \tag{4.23c}$$

Once all the values are extracted, they should be de-normalized to real frequencies. In our case, in order to prepare an implementation with coupled-lines structures, only the individual resonant angular frequencies, ω_k, and slope parameters, b_k ($k \in [0; N-1]$) of each node are necessary. They can be obtained considering a classical definition of the slope parameter for a shunt resonator for b_k, and the fact that the admittance of the de-normalized node k of the ladder network equals to zero at $\omega = \omega_k$ (see equation (4.14)). So they are given by the following

equations:

$$b_k = \frac{C_{Lk}}{FBW} \tag{4.24}$$

$$\omega_k = \omega_{BP}\left(-\frac{B_{Lk}FBW}{2C_{Lk}} + \sqrt{\left(\frac{B_{Lk}FBW}{2C_{Lk}}\right)^2 + 1}\right) \tag{4.25}$$

Example of application: *a triple-band band-pass resonator*

To make it clear, we propose to develop this method a triple-band band-pass resonator. We arbitrary set the three following bands:

1. Pass-band 1: 2.00 GHz-2.30 GHz (normalized low-pass frequency range: -1,-0.3088);
2. Pass-band 2: 2.40 GHz-2.60 GHz (normalized low-pass frequency range: -0.1000,0.2923);
3. Pass-band 3: 2.85 GHz-3.00 GHz (normalized low-pass frequency range: 0.7448,1).

We first determine the normalized cut-off angular frequencies of each band in the multiband low-pass domain using (4.18a) and (4.18b):

1. Pass-band 1: $\Omega_{L_1} = -1$ and $\Omega_{H_1} = -0.3088$;
2. Pass-band 2: $\Omega_{L_2} = -0.1000$ and $\Omega_{H_2} = 0.2923$;
3. Pass-band 3: $\Omega_{L_3} = 0.7448$ and $\Omega_{H_3} = 1$.

The input admittance of the low-pass ladder network in this triple-band case is:

$$\begin{aligned} Y_0^{(3)}(\Omega) &= j\frac{U(\Omega)}{V(\Omega)} \\ &= j\frac{\Omega^3 + u_2\Omega^2 + u_1\Omega + u_0}{v_2\Omega^2 + v_1\Omega + v_0} \end{aligned} \tag{4.26}$$

By mapping the normalized frequencies to the single-band low-pass domain using equations (4.21a) and (4.21b), we obtain the coefficients of all polynomials. The equation (4.26) can be expressed as:

$$Y_0^{(3)}(\Omega) = j\frac{\Omega^3 - 0.3142\Omega^2 - 0.4130\Omega + 0.0079}{0.6694\Omega^2 - 0.3063\Omega - 0.0824} \tag{4.27}$$

The parameter extraction can start with $C_{L0}^{(3)}$ and $B_{L0}^{(3)}$ using (4.22a) and (4.22b) respectively:

$$C_{L0}^{(3)} = \frac{1}{v_2} = \frac{1}{0.6694} = 1.4938 \tag{4.28a}$$

$$B_{L0}^{(3)} = \frac{u_2}{v_2} - \frac{v_1}{v_2^2} = \frac{-0.3142}{0.6694} + \frac{0.3063}{(0.6694)^2} = 0.2142 \tag{4.28b}$$

Using equations (4.23a) to (4.23c), we then extract step-by-step the other parameters:

$$Y_1^{(3)} = Y_0^{(3)} - jC_{L0}^{(3)}\Omega - jB_{L0}^{(3)} = j\frac{-0.2243\Omega + 0.02553}{0.6694\Omega^2 - 0.3063\Omega - 0.0824} \tag{4.29a}$$

$$C_{L1}^{(3)} = \lim_{\Omega\to\infty} \frac{1}{jY_1^{(3)}\Omega} = \lim_{\Omega\to\infty} \frac{0.6694\Omega^2 - 0.3063\Omega - 0.08237}{(0.2243\Omega - 0.02553)\Omega} = 2.9844 \tag{4.29b}$$

$$B_{L1}^{(3)} = \lim_{\Omega\to\infty} = \frac{\frac{1}{Y_1^{(3)}} - jC_{L1}^{(3)}\Omega}{j} = \lim_{\Omega\to\infty} \frac{-0.2301\Omega - 0.08237}{0.2243\Omega - 0.02553} = -1.0259 \tag{4.29c}$$

$$Y_2^{(3)} = Y_1^{(3)} - jC_{L1}^{(3)}\Omega - jB_{L1}^{(3)} = j\frac{-0.1087}{0.2243\Omega - 0.02553} \tag{4.30a}$$

$$C_{L2}^{(3)} = \lim_{\Omega\to\infty} \frac{1}{jY_2^{(3)}\Omega} = 2.0635 \tag{4.30b}$$

$$B_{L2}^{(3)} = \lim_{\Omega\to\infty} = \frac{\frac{1}{Y_2^{(3)}} - jC_{L2}^{(3)}\Omega}{j} = -0.2349 \tag{4.30c}$$

All the extracted parameters are summarized in Table 4.1. Using (4.24) and (4.25), we can get the slope parameters and resonant frequencies of each part of the multiband band-pass resonator. The slope parameters are $b_0 = 3.660$, $b_1 = 7.307$ and $b_2 = 5.069$ and the resonant frequencies are $f_0 = \omega_0/2\pi = 2.379$ GHz, $f_1 = \omega_1/2\pi = 2.507$ GHz and $f_2 = \omega_2/2\pi = 2.626$ GHz.

Table 4.1 – Extracted parameters for the triple-band case with the second method.

Extracted parameters		
$C_0 = 1.494$ F	$C_1 = 2.9844$ F	$C_2 = 2.0635$ F
$B_0 = 0.2142$	$B_1 = -1.0303$	$B_2 = -0.2349$

Note that the direct mapping technique proposed in Section 4.1.1, using of equations (7.63)-(7.71) presented in Appendix 7.4 gives exactly the same values of the resonant frequencies and the slope parameters than the ones obtained with this circuit approach.

4.2 Implementation method and examples for the proposed multiband band-pass filters

As mentioned in the introduction of this chapter, we have chosen a coupled-lines structure to implement the examples of MBPFs based on the in-line topology presented in the previous section. A general coupling schematic of the proposed in-line MBPFs is shown in Fig. 4.7. The needed parameters of all multiband band-pass resonators are obtained using one of the two methods presented previously. The based main-line band-pass filter (in the black rectangle in Fig. 4.7) can be also designed with different coupling paths with or without cross-coupling. In the examples presented here, no cross-coupling is used but such a solution could be of interest to add new transmission zeros for instance. In the same way, there is no cross-coupling between the band-stop parts of different multiband resonators.

As explained in Section 3.3, the design of coupled-lines structure implies the determination of the coupling coefficients. At the main-line band-pas level, we can use exactly the same formulas than in Section 3.3, that is to say:

$$Q_{es} = \frac{b_0}{m_{01}^2} = b_0 g_0 g_1 \tag{4.31}$$

$$Q_{el} = \frac{b_0}{m_{M,M+1}^2} = b_0 g_M g_{M+1} \tag{4.32}$$

$$K_{i,i+1} = \frac{m_{i,i+1}}{b_0} \quad \text{for } i \in [1; M-1] \tag{4.33}$$

where M is the filter order, $m_{i,i+1} = 1/\sqrt{g_i g_{i+1}}$ and g_i is the approximation coefficient of the i^{th} resonator. As the stop-band parts of each multiband resonator are not all connected to the pass-band cell unlike in the star-like topology but to one another, we need to define the couplings inside an individual multiband resonator (blue oval box in Fig. 4.7, that is to say the coupling between the band-pass cell and the first stop-band one and between two consecutive band-stop ones. This coupling coefficient is:

$$K_{s_{k,k+1}} = \frac{1}{\sqrt{b_k b_{k+1}}} \quad \text{with } k \in [0; N-1] \tag{4.34}$$

We applied this implementation method to the design of four 2^{nd}-order multiband band-pass filters to validate both the two proposed synthesis methods and the implementation technique. Each example was designed with a Chebyshev approximation in order to achieve a return loss level of 20 dB in the pass-band region. Therefore, the low-pass approximation coefficients are selected as $g_0 = 1$, $g_1 = 0.6648$, $g_3 = 0.5445$, $g_3 = 1.2210$, which corresponds to $m_{01} = m_{23} =$

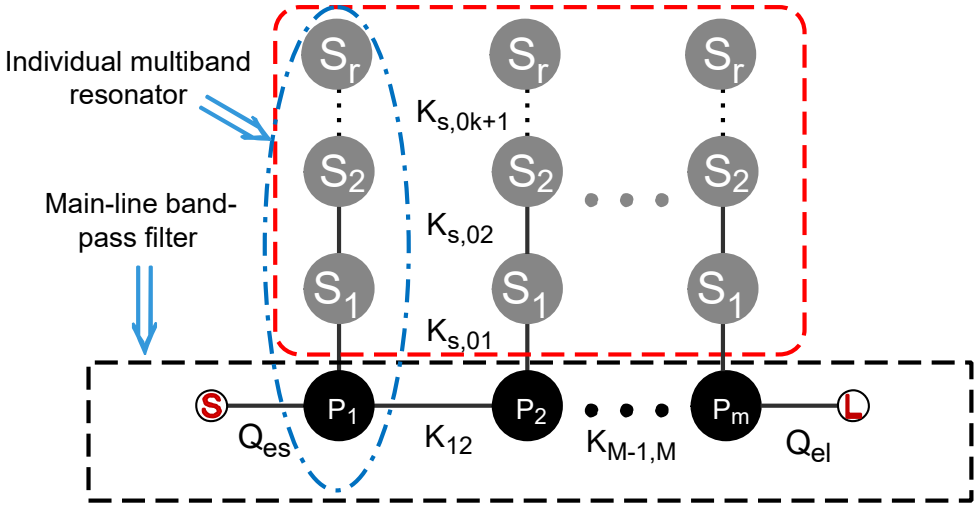

Figure 4.7 – Schematic view of a MBPF filter in in-line topology. The black dots represent the band-pass resonators, the gray dots represent the band-stop resonators. Inside the blue oval box is an individual multiband resonator; inside the black rectangle is the main-line based band-pass path; inside the red rectangular frame are the band-stop cell.

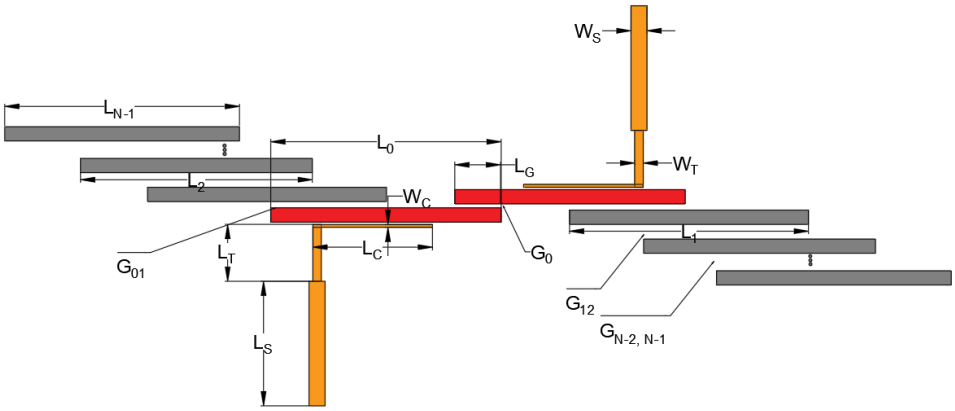

Figure 4.8 – Layout of the MBPFs with coupled-line structure. The yellow microstrip represent the feeding line, the red and gray ones represent the band-pass and band-stop resonators respectively.

1.2264 and $m_{12} = 1.6620$. The choice of identical order and return loss for each example was made for the sake of simplicity in the filter design.

Various technologies could be applied here to implement the four MBPFs. In this work, we have chosen planar microstrip technology because of its simple fabrication process, low-cost integration and compact-size. Fig. 4.8 illustrates a general structure of the proposed MBPFs consisting in multiple half-wavelength parallel-coupled lines. They are arranged in an in-line configuration so that adjacent resonators are parallel to each other. This parallel arrangement can achieve relatively large coupling coefficients for a given spacing between resonators. Correlation between these coupling coefficients and the relative position of two coupled lines were extracted using EM software in the same way as explained in Section 3.3. In Fig. 4.8, the yellow lines denote the feeding line of the MBPF, the red lines represent the band-pass resonators and the gray ones are the band-stop resonators with different resonant frequencies.

All the MBPFs designed in this chapter were fabricated on a RT/Duroid 6010 laminate substrate from Rogers Corporation with a thickness $h = 1.27$ mm, a relative permittivity $\varepsilon_r = 10.2$ and dissipation factor $\tan\delta = 0.0023$, associated with a double-sided copper layer of 17.5 μm thickness and a conductivity of $5.8 \times 10^7 \text{S.m}^{-1}$. For each resonator, the band-pass and the band-stop parts were implemented using half-wavelength lines, open-ended on both side and with the same line width of 1 mm. One thing must be noted is that the effect of even and odd mode characteristic impedances must be taken into account in the resonator implementation. This can be done by adjusting the line length in a small range or more accurately by the even- and odd-mode open-end analysis methods [55].

Example 1: triple-band in-line filter

The first example is a triple-band filter with the arbitrary following specifications:

— Pass-band 1: 3.00 GHz-3.08 GHz (FBW: 80 MHz);

— Pass-band 2: 3.25 GHz-3.38 GHz (FBW: 130 MHz);

— Pass-band 3: 3.60 GHz-3.70 GHz (FBW: 100 MHz).

These specifications given in terms of low and high cut-off angular frequencies can be transposed in terms of resonant frequencies and slope parameters using one of the two extracting parameters methods proposed in Sections 4.1.1 and 4.1.2. As explained at the end of the Section 4.1.2, the two methods give exactly the same results. In this example, the resulting resonant frequencies and slope parameters are $f_0 = \omega_0/2\pi = 3.327$ GHz, $f_1 = \omega_1/2\pi = 3.346$ GHz, $f_2 = \omega_2/2\pi = 3.303$ GHz and $b_0 = 10.73$, $b_1 = 5.507$ GHz, $b_2 = 13.32$ GHz respectively. The theoretical response of the triple-band filter is presented in Fig. 4.9. One should keep in mind that the sub-bands have the same in-band response as the main band-pass filter. In other words, all sub-bands have the same return loss level as the main band-pass filter would have without

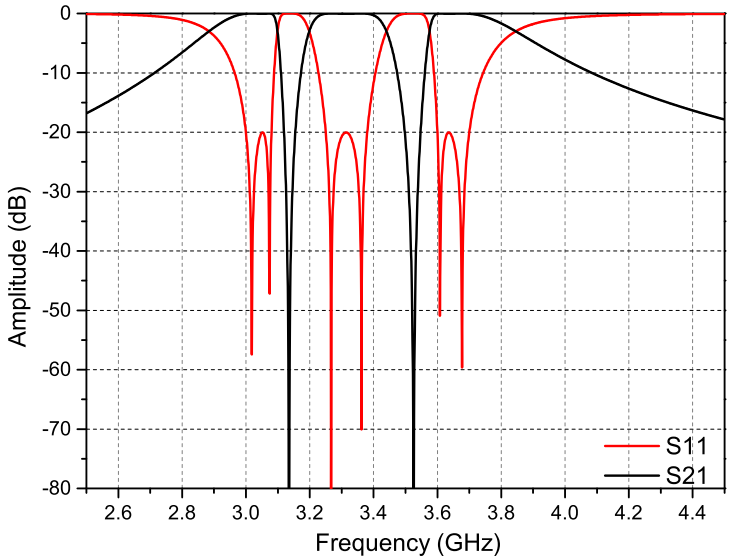

Figure 4.9 – Triple-band theoretical responses

Table 4.2 – Dimension of the triple-band band-pass filters with coupled structures.

Symbol	Values (mm)	Symbol	Values (mm)
L_s	8.45	W_s	1.16
L_t	3.60	W_t	0.60
L_c	8.90	W_c	0.20
L_g	3.27	L_0	16.50
L_1	16.45	L_2	16.58
G_0	0.36	G_c	0.18
G_{01}	1.62	G_{12}	0.73

the stop-band resonators (20 dB here).

The filter has been successfully implemented in coupled-lines microstrip technology with the substrate characteristics given above. A picture of the fabricated triple-band band-pass filter is shown in Fig. 4.10(a). The dimensions of the filter are presented in Table 4.2. The dimension symbols refer to those used in Fig. 4.8. The total size of the prototype is about $2.06\lambda_g \times 0.254\lambda_g$ (71.1×9.35 mm^2) without considering the 50 Ω access lines, λ_g is the guided wavelength of the center frequency of the filter.

Fig. 4.10(b) presents the EM-simulated and measured frequency responses of the fabricated triple-band band-pass filter. The correlation between both responses is very good for all the pass-bands. The measured insertion losses (ILs) are 1.92 dB, 1.23 dB and 1.37 dB from the first to the last pass-band and the measured return losses (RLs) are better than 12.1 dB, 15.3 dB, and 18.2 dB successively. We can also observe good band-to-band isolation between each pass-band (29.1 dB between the first and second pass-band, 38.9 dB between the second and the third).

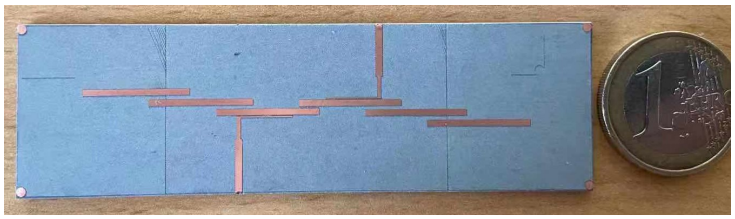

(a)

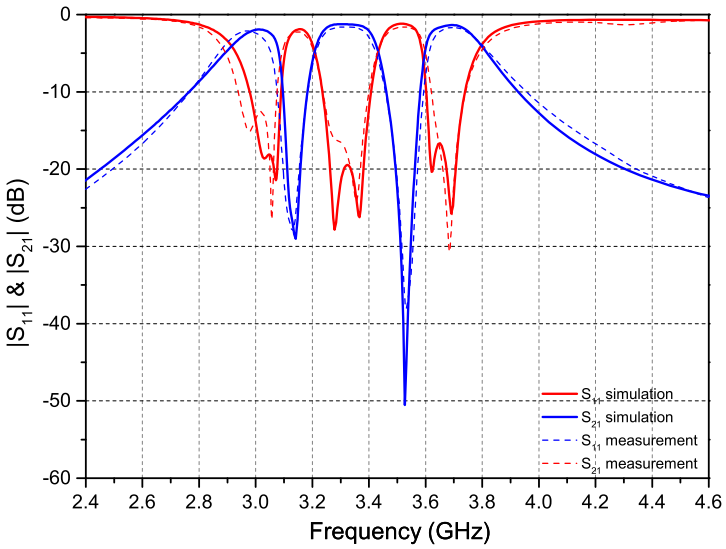

(b)

Figure 4.10 – Picture of the fabricated triple-band filter (a); associated EM-simulated (solid lines) and measured (dotted lines) S-parameters (b).

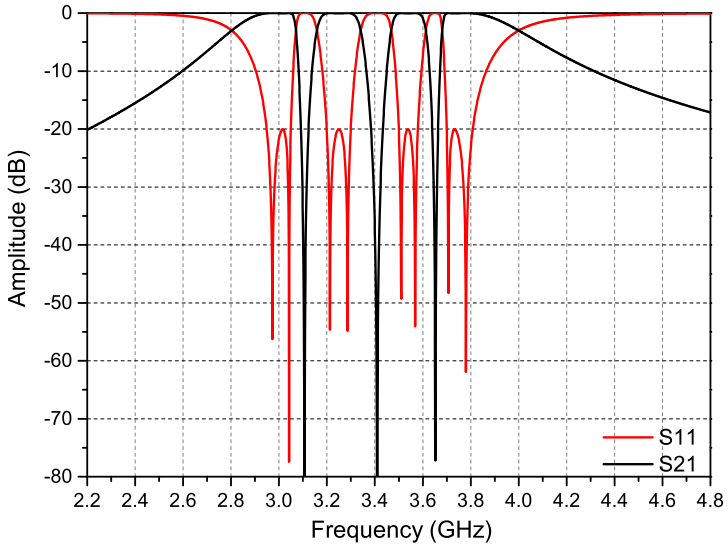

Figure 4.11 – Quad-band theoretical responses.

Example 2: quad-band in-line filter

With a similar synthesis method as for the triple-band case, the synthesis of a quad-band band-pass filter using the in-line topology is now proposed. Once again, both extracting methods can be used equivalently to obtain the output parameters, i.e the resonant angular frequencies and slope parameters.

Arbitrary specifications are also proposed here as an example to design, fabricate and measure a second-order quad-band band-pass filter. They show different bandwidths for each band and are the following:

— Pass-band 1: 2.95 GHz-3.05 GHz (FBW: 100 MHz);
— Pass-band 2: 3.20 GHz-3.30 GHz (FBW: 100 MHz);
— Pass-band 3: 3.50 GHz-3.58 GHz (FBW: 80 MHz);
— Pass-band 4: 3.70 GHz-3.81 GHz (FBW: 110 MHz).

Using one of the two extracting methods, the multiband resonator parameters are $f_0 = \omega_0/2\pi =$ 3.346 GHz, $f_1 = \omega_1/2\pi = 3.357$ GHz, $f_2 = \omega_2/2\pi = 3.336$ GHz, $f_3 = \omega_3/2\pi = 3.454$ GHz and $b_0 = 8.587$, $b_1 = 4.399$, $b_2 = 15.91$, $b_3 = 5.795$. The theoretical response of this quad-band filter is shown in Fig. 4.11.

The coupled-lines quad-band filter was also implemented in the same topology and technology as the previous one. A photography of the fabricated filter is shown in Fig. 4.12(a) and its dimensions are given in Table 4.3. The total size of this circuit is $2.74\lambda_g \times 0.294\lambda_g$ (91×9.83 mm^2). Its EM-simulated (solid lines) and measured (dotted lines) S-parameters are shown in Fig. 4.12(b). Both are, once again, in good correlation. The measured ILs are 1.56 dB, 2.38

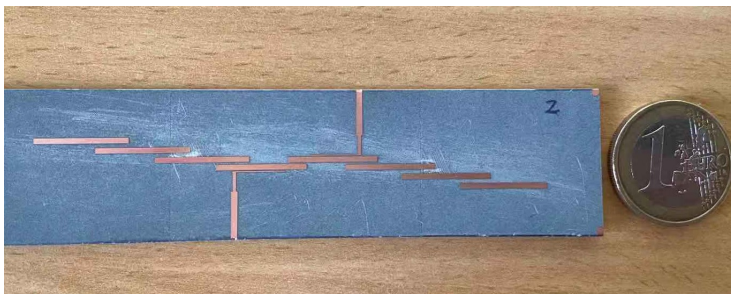

(a)

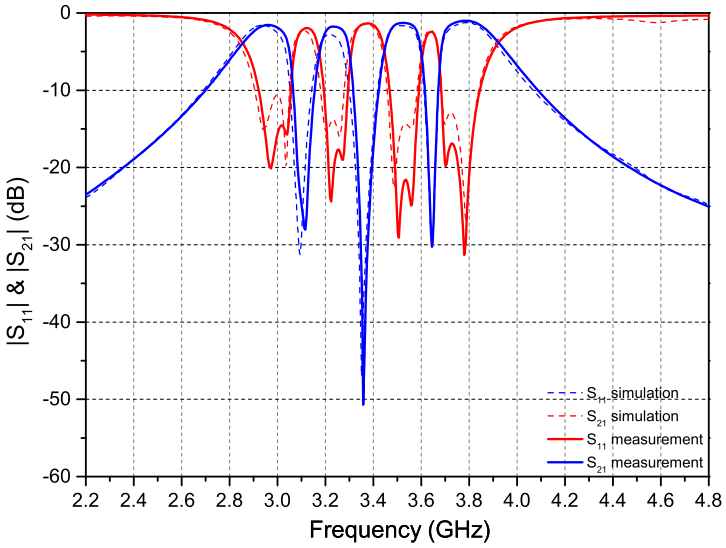

(b)

Figure 4.12 – Picture of the fabricated quad-band filter (a); associated EM-simulated (solid lines) and measured (dotted lines) S-parameters.

dB, 1.63 dB, 1.28 dB from the first to the fourth band and the measured RLs are better than 10.8 dB, 13.9 dB, 14.5 dB and 12.9 dB, successively. Good isolation (31.1 dB between the first and the second pass-band, 46.7 dB between the second and the third one, and 29.1 dB between the third and the fourth one) are again achieved between all the pass-bands.

Example 3: quint-band in-line filter

The third example is a quint-band band-pass filter. As explained before, for 5 bands or more, only the second extracting method based on the circuit approach (see Section 4.1.2 can be used to obtain the output parameters from the cut-off frequencies. These latters are arbitrary chosen as follows for this example:

— Pass-band 1: 2.92 GHz-3.00 GHz (FBW: 80 MHz);

Table 4.3 – Dimension of the quad-band band-pass filters with coupled structures.

Symbol	Values (mm)	Symbol	Values (mm)
L_s	8.45	W_s	1.17
L_t	3.60	W_t	0.60
L_c	9.30	W_c	0.20
L_g	3.31	L_0	16.20
L_1	16.50	L_2	16.30
G_0	0.26	G_c	0.19
G_{01}	0.45	G_{12}	0.78
L_3	16.02	G_{23}	0.79

— Pass-band 2: 3.15 GHz-3.21 GHz (FBW: 60 MHz);
— Pass-band 3: 3.40 GHz-3.45 GHz (FBW: 50 MHz);
— Pass-band 4: 3.60 GHz-3.66 GHz (FBW: 60 MHz);
— Pass-band 5: 3.80 GHz-3.90 GHz (FBW: 100 MHz).

The application of the second extraction method leads to the output parameters given in Table 4.4.

Table 4.4 – Intermediate and output parameters obtained using the second extraction method in the case of a quint-band filter.

extracted parameters					
k	0	1	2	3	4
C_{Lk} (F)	2.7678	0.7855	5.7743	0.9166	14.4515
B_{Lk}	-0.08034	0.028625	-0.0092	-0.02111	-2.109
b_k	9.531	2.705	19.884	3.1564	42.877
f_k (GHz)	3.3889	3.3568	3.3754	3.3859	3.3459

As for the two previous examples, theoretical responses of the quint-band filter are first presented in Fig. 4.13. They correspond once again perfectly to the specifications. The filter was fabricated using the same coupled-lines structure and the same materials characteristics. A picture of the fabricated filter is presented in Fig. 4.14(a). Its dimensions are summarized in Table 4.5. The total size of the circuit is $2.50\lambda_g \times 0.311\lambda_g$ (86.9×10.82 mm^2).

Fig. 4.14(b) illustrates the measured and simulation results. EM simulations and measurements are in good agreements. The measured ILs are 1.96 dB, 4.45 dB, 3.08 dB, 3.21 dB and 1.60 dB from the first to the fifth pass-band. The measured RLs are better than 12.1 dB, 12.5 dB, 19.1 dB, 18.2 dB, and 15.8 dB, successively. The measured isolation between two consecutive bands are 33.2 dB, 52.2 dB, 40.2 dB, 29.7 dB from the first stop-band to the last one.

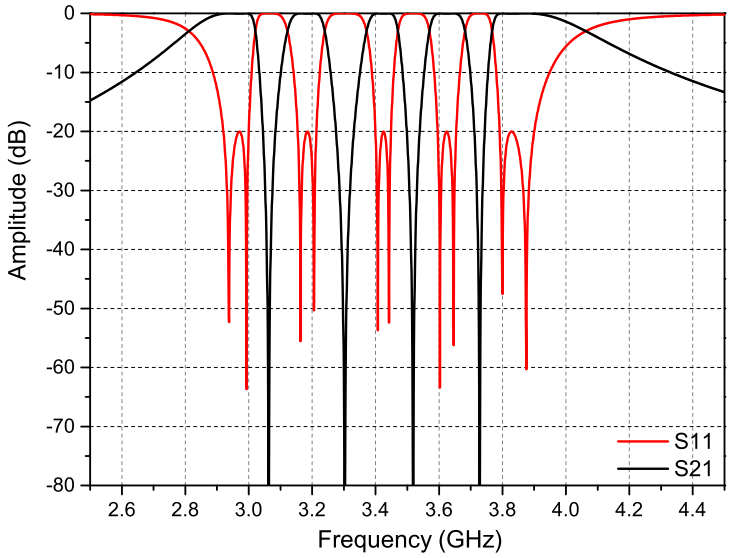

Figure 4.13 – Quint-bands theoretical responses.

Table 4.5 – Dimension of the quint-band band-pass filters with coupled structures.

Symbol	Values (mm)	Symbol	Values (mm)
L_s	8.35	W_s	1.16
L_t	4.00	W_t	0.60
L_c	8.40	W_c	0.20
L_g	3.27	L_0	16.20
L_1	16.20	L_2	16.65
G_0	0.27	G_c	0.17
G_{01}	0.43	G_{12}	0.98
L_3	16.52	G_{23}	1.22
L_4	16.01	G_{34}	1.08

Example 4: sixfold-band in-line filter

The last example to show the effectiveness of the proposed strategy is a sixfold-band band-pass filter. The proposed specifications are here:

— Pass-band 1: 2.95 GHz-3.00 GHz (FBW: 50 MHz);
— Pass-band 2: 3.12 GHz-3.16 GHz (FBW: 40 MHz);
— Pass-band 3: 3.30 GHz-3.35 GHz (FBW: 50 MHz);
— Pass-band 4: 3.50 GHz-3.54 GHz (FBW: 40 MHz);
— Pass-band 5: 3.70 GHz-3.78 GHz (FBW: 80 MHz);
— Pass-band 6: 3.88 GHz-3.95 GHz (FBW: 70 MHz).

The output parameters corresponding to these specifications can be obtained using the same

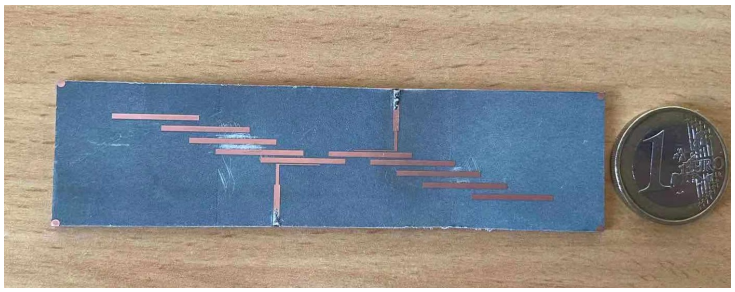

(a)

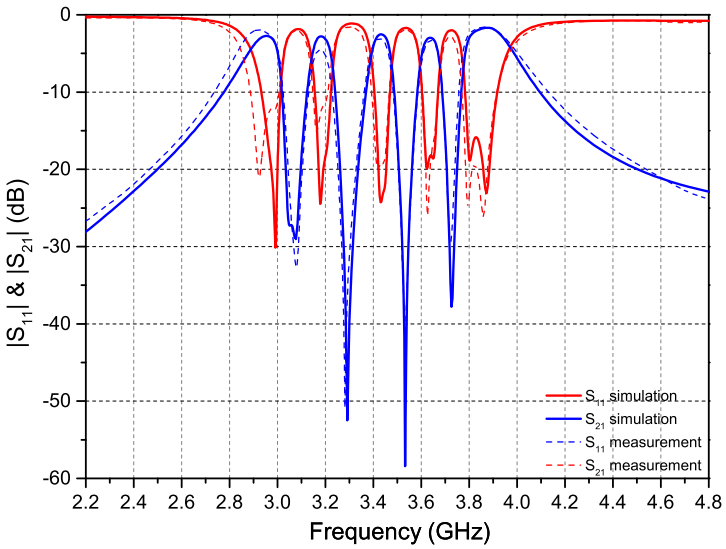

(b)

Figure 4.14 – Picture of the fabricated quint-band filter (a); associated EM-simulated (solid lines) and measured (dotted lines) S-parameters (b).

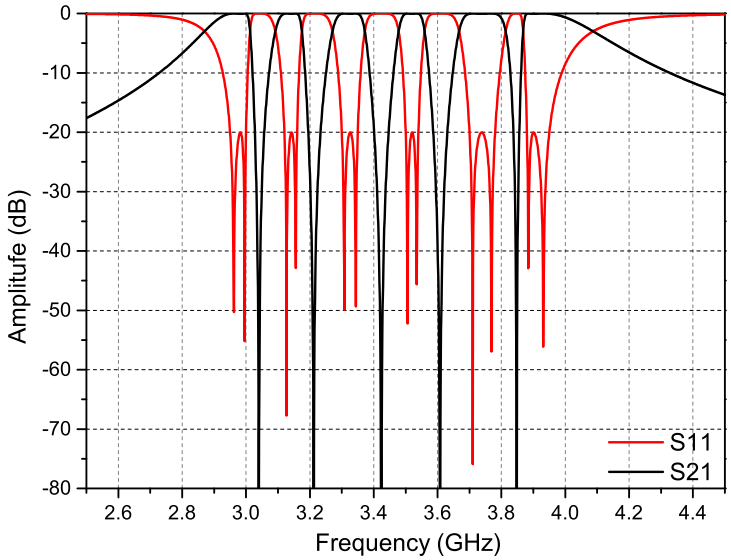

Figure 4.15 – Sixfold-band theoretical responses.

procedure as for the quint-band case. There are summarized with the intermediate values in Table 4.6.

Table 4.6 – Intermediate and output parameters obtained using the second extraction method in the case of a sixfold-band filter.

extracted parameters						
k	0	1	2	3	4	5
C_{Lk} (F)	3.0613	0.7681	5.3182	0.7720	6.3236	1.5054
B_{Lk}	-0.2161	0.05360	0.2083	-0.08435	0.08414	-0.03183
b_k	10.45	2.622	18.154	2.6352	21.586	5.1388
f_k (GHz)	3.4491	3.3789	3.3941	3.4687	3.4070	3.4242

As for the previous examples, we present successively the theoretical responses (see Fig. 4.15), a picture of the fabricated filter (see Fig. 4.16(a)), and its dimensions (see Table 4.7). The filter is fabricated with the same characteristics as the previous ones and its total size is about $2.90\lambda_g \times 0.347\lambda_g$ (91.2×10.9 mm^2).

Fig. 4.16(b) gives the simulated and measured results, which show good agreement. Small inconsistency between both results for the second pass-band mainly comes from the practical implementation and testing. The measured ILs within the six channels are 1.97 dB, 4.18 dB, 2.28 dB, 3.46 dB, 3.03 dB, 1.56 dB from the first to the sixth pass-band, respectively. The measured RLs within the six channels are better 12.0 dB, 11.9 dB, 15.1 dB, 13.2 dB, 13.9 dB. The isolation between two consecutive bands is better than 21.1 dB, 24.4 dB, 41.5 dB, 33.6 dB, 21.7 dB for the five stop-band, respectively.

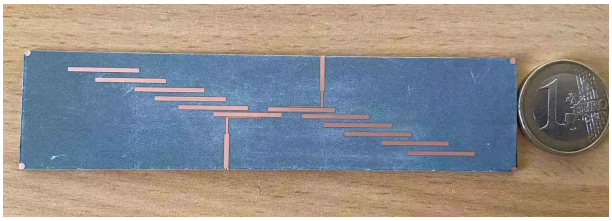

(a)

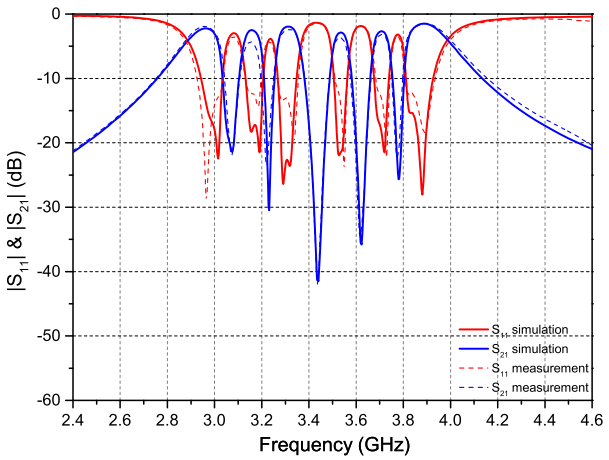

(b)

Figure 4.16 – Picture of the fabricated sext-band filter (a). EM-simulated (solid lines) and measured (dotted lines) S-parameters of the sixfold-band band-pass filter (b).

Table 4.7 – Dimension of the sext-band band-pass filters with coupled structures

Symbol	Values (mm)	Symbol	Values (mm)
L_s	8.30	W_t	1.16
L_t	4.00	W_t	0.60
L_c	8.70	W_c	0.20
L_g	3.22	L_0	16.21
L_1	16.40	L_2	16.35
G_0	0.37	G_c	0.15
G_{01}	0.44	G_{12}	1.03
L_3	16.00	G_{23}	1.08
L_4	16.20	G_{34}	0.75
L_5	16.21	G_{45}	1.56

4.3 Conclusion

The main topic of this chapter is the introduction of a class of multiband band-pass filters in an in-line topology. Two synthesis methods are proposed and used here to extract the synthesis parameters. The first one is a universal way to obtain the needed parameters. It is in the same way as the one proposed in Chapter 3 and can be used with any transformation functions for different implementation topologies such as star-like, in-line and also mixed topology. The second method can only be implemented for in-line topology. Note that for a mixed topology, one can use coupling matrix rotations to achieve a specific topology initially based on star-like or in-line topology.

In this chapter, the filter implementation of the few examples in an in-line topology have been achieved using microstrip technology. It allow to synthesize MBPFs with a relative wide-band bandwidth. We can also use waveguide or SIW technology to make these filters, but it may be a challenging work to have a wide-band and a high number of pass-bands. Also, MBPFs based on in-line topology may have difficulties for optimization procedure, since the coupling coefficients are related between different band-stop resonators.

In the next and last chapter, the concept of associated band-stop resonators (ABSRs) will be presented. Based on ABSRs, several high numbers pass-band filters with wide-band performance will also be demonstrated.

Chapter 5

Directly synthesis of multiband filters with associated band-stop resonators

In chapter 3 and chapter 4, we mainly focused on the frequency transformation methods to design MBPFs. These method are based on strict mathematical analysis and provide a mapping relationship between theory and implementation circuits. However, frequency transformation method have two significant disadvantages. The first disadvantage is that the TZs between the individual pass-bands are not controllable. In other words, the TZs are not independent. Another disadvantage is that the bandwidth of each pass-band cannot be too wide, because the synthesis of this type of filter is based on synthesis methods. In this chapter, we will introduce a novel method to design MBPFs based on optimization approach, which can solve the above two problems to some extent allowing to design MBPFs with controllable in-band transmission zeros (TZs) and relative large individual pass-bands.

The proposed design method is based on the parallel association of $N-1$ band-stop stepped-impedance stubs to form a N pass-bands resonator. We show that such a simple design principle allows the accurate control of TZs positions. The principle and theory of such filters based on associated band-stop resonators (ABSRs) are exposed and their efficiency is shown through synthesis, design, simulation and measurement. In order to demonstrate the effectiveness and advantages of ABSRs, we provide dual-, tri-, quad-, and quint-band 3^{rd} filter examples in the next several sections with both theory study and microstrip implementation.

5.1 Theory of proposed associated band-pass resonators

The structure of the proposed MBPF based on ABSRs is shown in Fig. 5.1. A multi-band resonator is composed of $N-1$ short-ended stepped-impedance stubs in a star-like implementation (Fig. 5.2). Unlike the star-like resonators proposed in Chapter 3, the ABSRs do not include the shunt-connected stubs for band-pass. For simplicity, we assume that the electrical length of each part of a branch i ($i \in [1; N-1]$) of the ABSRs equals to $\lambda/4$ (or $\theta_i = \pi/2$) at its

resonant frequency f_{zi}, which corresponds to a transmission zero. The behavior of the parallel association of the $N-1$ branches can then be written in term of total input admittance, Y_{tot}, as:

$$Y_{tot} = \sum_{i=1}^{N-1} Y_i = j \sum_{i=1}^{N-1} \frac{(Z_{i2} tan(\frac{f}{f_{zi}}\frac{\pi}{2}) - Z_{i1}) \cot(\frac{f}{f_{zi}}\frac{\pi}{2})}{Z_{i1}(Z_{i1}+Z_{i2})} \tag{5.1}$$

where Y_i denotes the input characteristic admittance of the branch i, f is the working frequency, and Z_{i1} and Z_{i2} are the characteristic impedances of the first and the second parts of the i^{th} short-ended stub ($i \in [1; N-1]$), respectively.

It is easy to find that the TZs are obtained when $f = f_{zi}$. In this condition, the input admittance goes to infinity and each TZ f_{zi} determines the length of its associated branch i independently of others. We will also use two additional TZs, the first one at the origin ($f_{z0} = 0$ Hz) and the last, called f_{z_N}, which is the first harmonic of f_{z1} ($f_{z_N} = 2f_{z1}$). Of course, these two additional TZs cannot be fixed independently but they participate in the creation of the first and last bands respectively. One reflection zero can be obtained between two consecutive TZs leading to a total of N pass-bands. These reflection zeros appear when $Y_{tot} = 0$. One should notice that (5.1) is non-linear. As a consequence, the equation bound to the slope parameters is also non-linear. In order to simplify the filter conception, an optimization is performed to determine the characteristic impedance Z_{i1} and Z_{i2} according to the pass-band specifications and considering that the first impedance needs to be as high as possible and that the second one must be relatively low to obtain narrow rejected bands between each pass-band. From the knowledge of the transmission and reflection zeros and the characteristic impedance pairs of each stepped-impedance stub, the slope parameters of each pass-band can then be determined from:

$$\begin{aligned} b(\omega) &= \frac{\omega}{2} Im\left(\frac{\partial Y_{tot}}{\partial \omega}\right)|_{\omega=\omega_r} \\ &= \frac{\pi}{4} \sum_{i=1}^{N-1} \frac{f}{f_{zi}} \frac{1}{(Z_{i1}+Z_{i2})} \left(\csc^2(\frac{\pi}{2}\frac{f}{f_{zi}}) + \frac{Z_{i2}}{Z_{i1}} \sec^2(\frac{\pi}{2}\frac{f}{f_{zi}})\right) \end{aligned} \tag{5.2}$$

A classical ladder-type topology is used to design the MBPF by associating different ABSRs as presented in Fig. 5.1. The ABSRs are separated with admittance inverters, J_{kl} with $k \in [0, M-1]$ and $l \in [1; M]$, M being the filter order. One interesting feature should be pointed out here: as shown in (5.2), there are several combinations of impedances and TZs that can achieve the same slope parameters. This allows us to have more degrees of freedom to optimize the MBPF. In examples presented hereafter, however, we deal only with three identical ABSRs to design each third-order multi-band band-pass filters for the sake of simplicity. A general schematic view of the proposed third-order multi-band filter is given in Fig. 5.3.

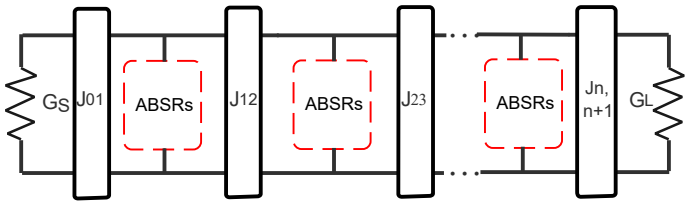

Figure 5.1 – Proposed MBPFs with associated band-stop resonators.

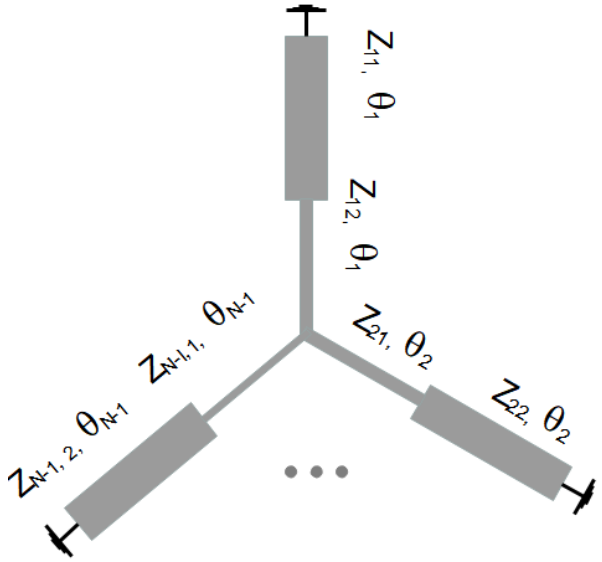

Figure 5.2 – ABSRs: multiband resonators with star topology.

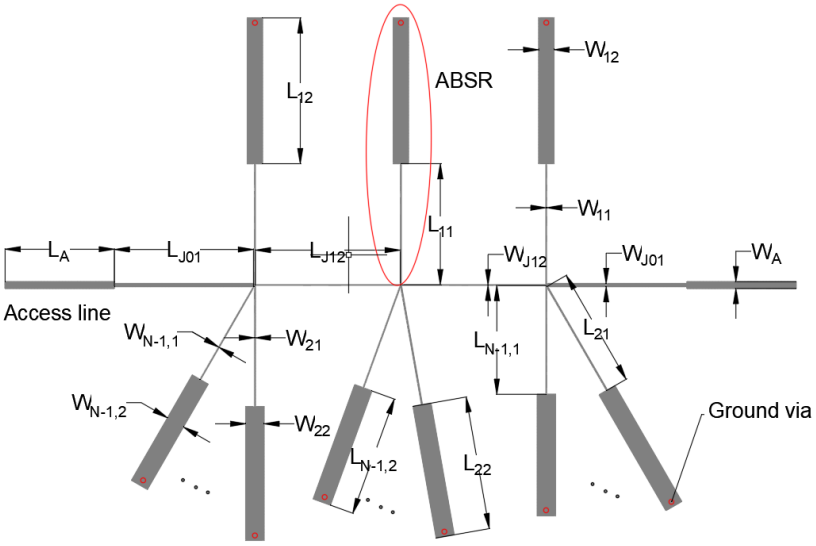

Figure 5.3 – Dimension of the proposed third-order MBPFs.

5.2 Some examples based on the proposed ABSRs

5.2.1 Dual-band band-pass filter

To validate our proposed synthesis method, a dual-band 3^{rd}-order Chebyshev band-pass filter is first presented here. First of all, according to the two specified pass-bands, we fix $f_{z1} = 2.3$ GHz, which will separate the two bands. Also, There are TZs at $f_{z2} = 0$ and the first harmonic frequency $f_{z3} = 4.6$ GHz, we so have three TZs. It's a great advantage of our ABSRs, because we can both utilize the two resonant frequencies instead of using three band-stop resonators to produce two pass-bands, as achieved with DBRs [56]. It greatly reduces the dimension of the circuits. Another characteristic of the ABSRs is that we know the first harmonic frequency f_{z2} is two times the first stop-band frequency. The two pass-bands are located in the frequencies ranges from DC to f_{z1} and from f_{z1} to f_{z2}, respectively. Thus, a quiet large bandwidth be achieved and we can make full use of the frequency range to build more pass-bands. However, there are also some drawbacks for the proposed ABSRs. First, the resonating frequency of each pass-band are related to each other, optimization methods need to be used when specified pass-band location are required. Second, the harmonic frequency can not be controlled, it may influence the behavior of the last pass-band. Third, we can only have symmetrical responses due to the uncontrollable TZs in DC and first harmonic frequency. For dual-band case, we can calculate the resonant frequencies of each pass-bands according to (5.1) with $N = 2$. They are obtained by solving the following equation:

$$\frac{1}{Z_{11}(Z_{11}+Z_{12})}\left(Z_{12}\tan(\frac{f_r}{f_{z1}}\frac{\pi}{2}) - Z_{11}\cot(\frac{f_r}{f_{z1}}\frac{\pi}{2})\right) = 0 \tag{5.3}$$

The two resonant frequencies can be expressed as:

$$f_{r1} = \frac{2}{\pi}f_{z1}\arctan\left(\sqrt{\frac{Z_{11}}{Z_{12}}}\right) \tag{5.4}$$

and,

$$f_{r2} = \pi - \frac{2}{\pi}f_{z1}\arctan\left(\sqrt{\frac{Z_{11}}{Z_{12}}}\right) \tag{5.5}$$

The determination of the resonant frequencies requires the knowledge of the characteristic impedance pairs of each branch of the multi-band band-pass resonators. They are selected according to the specification in an optimization process, in order to be sure that the resonant frequencies are located in the ranges of each individual pass-band. In practice, impedance values and resonant frequencies are therefore determined simultaneously. As a dual-band example, we arbitrary set the following specifications as:

1. Pass-band 1: 1.59 GHz-2.07 GHz (BW: 480 MHz);

Table 5.1 – Dimensions of the dual-band band-pass filters with ABSR.

Symbol	Values (mm)	Symbol	Values (mm)
L_{J01}	20.13	W_{J01}	0.51
L_{J02}	20.85	W_{J02}	0.13
L_{11}	20.7	W_{11}	0.17
L_{12}	19.0	W_{12}	2.20

2. Pass-band 2: 2.52 GHz-3.00 GHz (BW: 480 MHz);

To determine values of the elements according to the specified bandwidths, the following steps can be implemented:

1. Determination of the TZ, here $f_{z1} = 2.30$ GHz. This step fixes the electrical length of each branch of the ABSR. We also deduce that $f_{z2} = f_{z1}$ =4.6 GHz.

2. Selection of the impedance pairs of each stepped-impedance stub forming the multiband resonator according to the bandwidth specification. These values imply that $f_{r1} = 1.60$ GHz, $f_{r2} = 3.0$ GHz.

3. To get a certain order, the multiband resonators are separated by admittance inverters, whose values J_{01} and J_{12}, are determined using an optimization process considering the pass-band ripple and each pass-band bandwidth. For this case the values are with $J_{01} = J_{34} = 0.0129\ \Omega$ and $J_{12} = J_{23} = 0.0072\ \Omega$ and so the impedance of the quarter-wavelength lines used to implement them are $Z_{J01} = Z_{J34} = 77.72\ \Omega$ and $Z_{J12} = Z_{J23} = 138.89\ \Omega$.

4. The concept can easily be used to design a filter with a high band-pass number. Different to examples, starting here with a tri-band filter, are proposed in this section and the following ones.

Fig. 5.4(a) presents the response of a single ABSR and Fig. 5.4(b) plots the responses of 3^{rd} filter. As expected, the two resonant frequencies are related to $f_{r1} = 1.60$ GHz, $f_{r2} = 3.0$ GHz. Fig. 5.5(a) shows the fabricated filter. Fig. 5.5(b) plots the EM simulation and measurement results. The filter was implemented in microstrip technology with a RO4003C Rogers substrate (dielectric constant: $\varepsilon_r = 3.55$, height: $h = 0.508$ mm, dissipation factor: $\tan\delta = 0.0027$) with copper metallization (metal width: $t = 17.5\ \mu$m, conductivity: $\sigma = 5.8 \times 10^7$ S.m^{-1}). Result shows good filter response in both band-pass and excellent measured band isolation (about 60 dB) in the stop-band. The return losses (RLs) for the first pass-band and second pass-band are better than 18.3 dB and 13.3 dB. The insertion losses (ILs) for the first pass-band is 1.26 dB and 1.99 dB for the second pass-band at center frequency. The fabricated filter's dimension are detailed in Table 5.1. The overall size of the filter is 81.96×39.7 mm^2 without taking into account the two 50 Ω access lines.

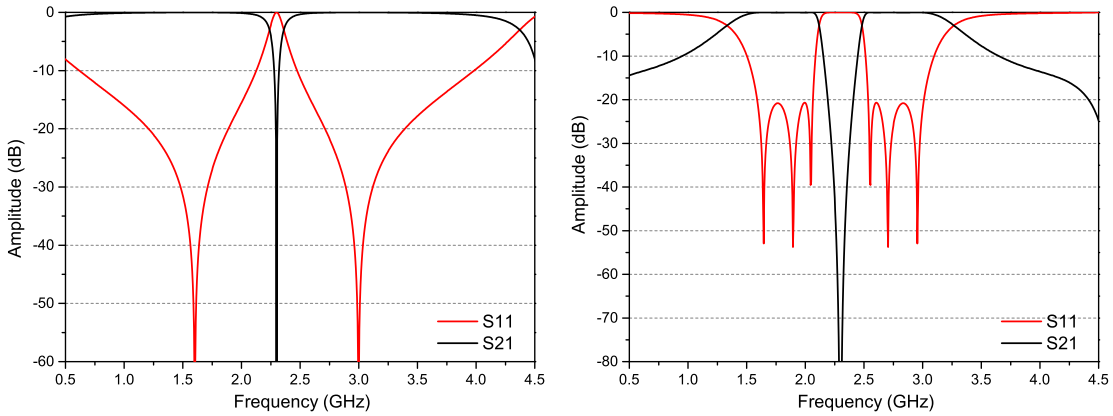

(a) (b)

Figure 5.4 – Frequency responses of an individual dual-band ABSR(a) and of the Dual-band filter based on this ABSR (b).

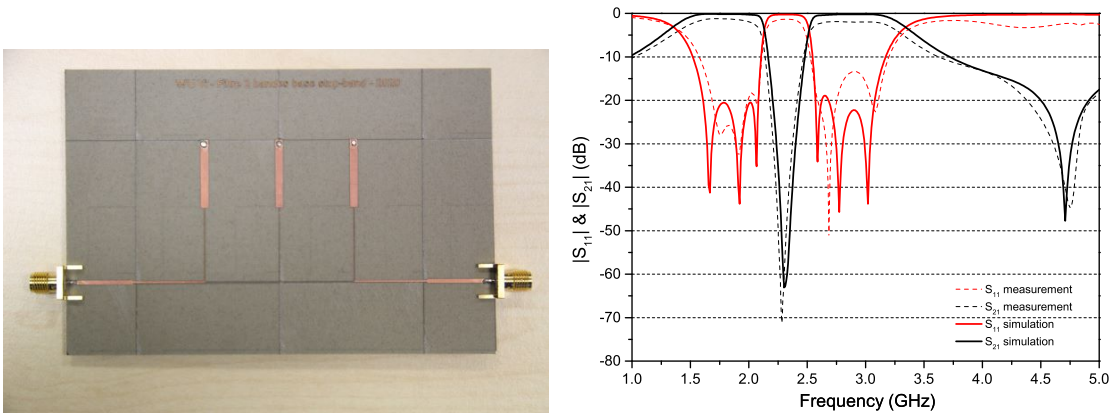

(a) (b)

Figure 5.5 – Photography of the fabricated ABSR-based dual-band filter (a) and its EM-simulated (solid lines) and measured(dotted lines) S-parameters (b).

5.2.2 Tri-band band-pass filter

A 3^{rd}-order tri-band band-pass filter with its implementation in microstrip technology is thus proposed as a second example in this section. By using our proposed ABSRs, there is no great challenge to design such MBPFs. The arbitrary pass-band frequencies specifications we have chosen to design this example are defined as follow:

1. Pass-band 1: 2.34 GHz-2.77 GHz (BW: 430 MHz);
2. Pass-band 2: 3.29 GHz-3.59 GHz (BW: 300 MHz);
3. Pass-band 3: 4.28 GHz-4.61 GHz (BW: 330 MHz).

Following the same process as in the dual-band case, we first fix the TZs at $f_{z1} = 3$ GHz and $f_{z2} = 4$ GHz, we thus have $f_{z3} = 2f_{z1} = 6$ GHz. Then, we select the impedance of each branche in order that the resonant frequencies are related to their respective band, the latter being determined taking $Y_{tot} = 0$ in (5.2) with N =3.

$$\sum_{i=1}^{2} \frac{1}{Z_{i1}(Z_{i1} + Z_{i2})} \left(Z_{i2} \tan(\frac{f_r}{f_i}\frac{\pi}{2}) - Z_{i1} \cot(\frac{f_r}{f_i}\frac{\pi}{2}) \right) = 0 \tag{5.6}$$

By solving the equation, the three resonant frequencies are located at 2.361 GHz, 3.419 GHz, and 4.616 GHz respectively with the choosen stubs impedance: $Z_{11} = 133.3\ \Omega$, $Z_{12} = 35.7\ \Omega$, $Z_{21} = 125.0\ \Omega$, $Z_{22} = 33.3\ \Omega$. With the same design procedures presented in the dual-band case, the inverters' values are selected as $Z_{J01} = Z_{J34} = 73.3\ \Omega$, $Z_{J12} = Z_{J23} = 128.2\ \Omega$.

The filter ideal responses are shown in Fig. 5.6 with a maximum matching level of about 20 dB. It is interesting to note that this type of filters has a quasi-equal ripple characteristic in the pass-bands region. In other words, the ripple is not strictly flat in all pass-bands, but it has little influence on the performance of the filter. Simulation and measurement results are presented in Fig. 5.7(b) with the circuit board presented in Fig. 5.7(a). The simulation shows good filter response in each pass-band and excellent band isolation (about 58.6 dB between the first and second pass-band, 50.1 dB between the second and third pass-band). The measured RLs from the first to the third pass-band are better than 18.2 dB, 14.0 dB and 10.7 dB respectively. Owing to the limited accuracy of the etching process, we have chosen suitable values to avoid too narrow (less than 0.1 mm) or too wide (more than 4 mm) line width. The level of the ILs in the fabricated filter slightly deviates from the desired values. The measured ILs for each pass-band is 2.51 dB, 3.33 dB and 3.53 dB. The fabricated filter's dimension is shown in Table 5.2. The overall size of the filter is 54.2×53.4 mm^2 without taking into account the two 50 Ω access lines.

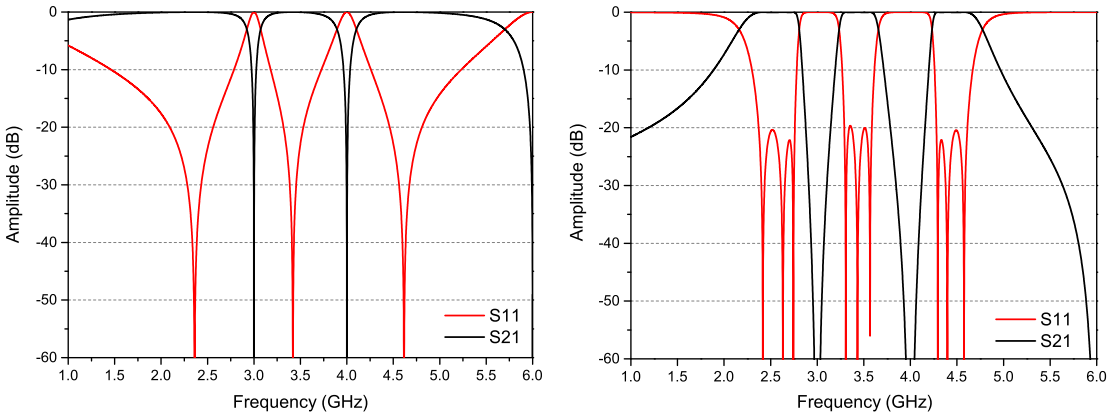

(a) (b)

Figure 5.6 – Frequency responses of an individual tri-band ABSR(a) and of the tri-band filter based on this ABSR (b).

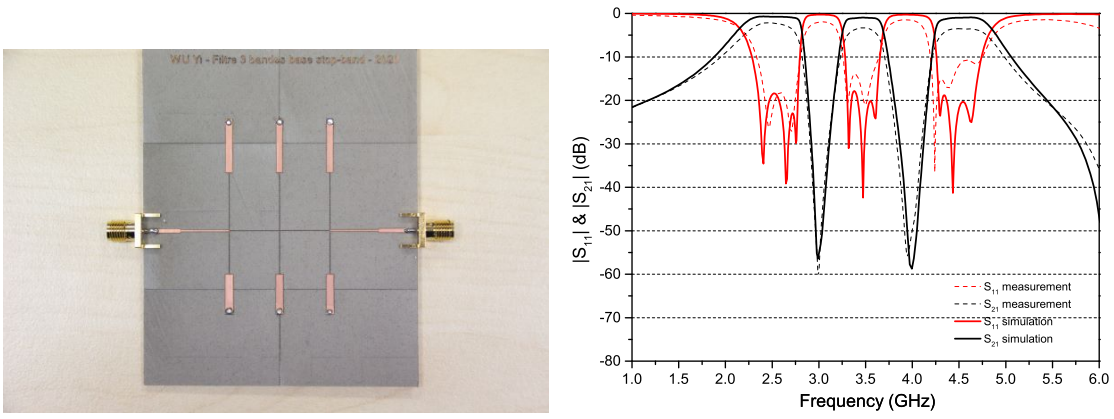

(a) (b)

Figure 5.7 – The fabricated tri-band circuit (a) and its EM-simulated (solid lines) and measured(dotted lines) S-parameters (b).

Table 5.2 – Dimensions of the tri-band band-pass filters with ABSR.

Symbol	Values (mm)	Symbol	Values (mm)
L_{J01}	13.3	W_{J01}	0.50
L_{J02}	20.8	W_{J02}	0.10
L_{11}	11.91	W_{11}	0.12
L_{12}	15.94	W_{12}	1.95
L_{21}	14.66	W_{21}	0.14
L_{22}	10.92	W_{22}	2.25

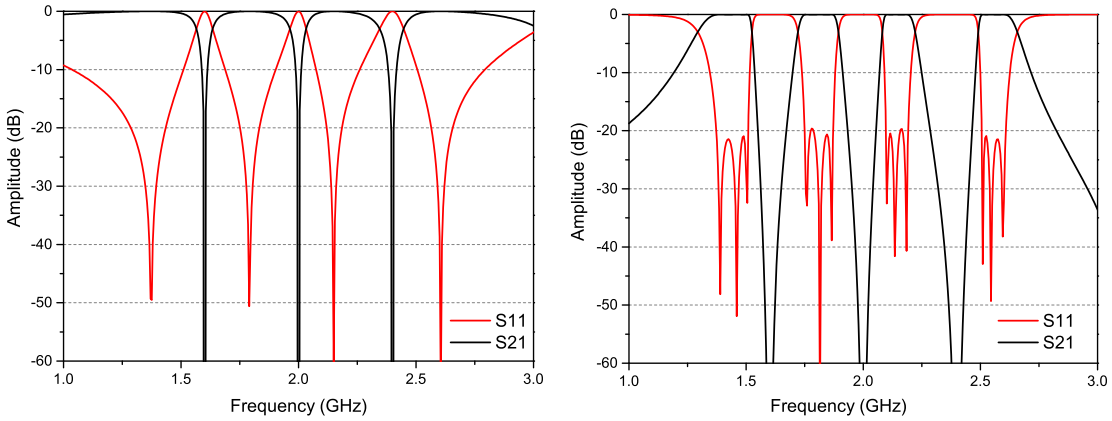

(a) (b)

Figure 5.8 – Quad-band Star-like Resonators S parameters (a); idea responses of the quad-band bandpass filter (b).

5.2.3 Quad-band band-pass filter

A 3^{rd}-order quad-band band-pass filter and its implementation in microstrip technology are proposed in this section as another example. There are only few implementation examples for third-order quad-band MBPFs whatever the technology in the literature. Using our proposed ABSRs topology, there is here again no specific challenge to design such MBPFs. The arbitrary pass-band frequencies specifications we have chosen to design this example are defined as follows:

1. Pass-band 1: 1.38 GHz-1.51 GHz (BW: 130 MHz);
2. Pass-band 2: 1.75 GHz-1.85 GHz (BW: 100 MHz);
3. Pass-band 3: 2.10 GHz-2.18 GHz (BW: 80 MHz);
4. Pass-band 4: 2.50 GHz-2.59 GHz (BW: 90 MHz).

Firstly, we choose the three TZs at $f_{z1} = 1.60$ GHz, $f_{z2} = 2.0$ GHz and $f_{z3} = 2.4$ GHz respectively. We so have $f_{z4} = 2f_{z1} = 3.20$ GHz. The impedance values of the ABSRs are then chosen following the same procedure and constraints as in the tri-band case. For this

Table 5.3 – Dimensions of the quad-band band-pass filters with ABSR.

Symbol	Values (mm)	Symbol	Values (mm)
L_{J01}	23.15	W_{J01}	0.55
L_{J02}	24.0	W_{J02}	0.13
L_{11}	29.90	W_{11}	0.12
L_{12}	27.20	W_{12}	2.50
L_{21}	23.40	W_{21}	0.12
L_{22}	21.50	W_{22}	3.01
L_{31}	19.85	W_{231}	0.15
L_{32}	17.97	W_{32}	3.00

example, the impedance values are: $Z_{11} = 132.0\ \Omega$, $Z_{12} = 24.0\ \Omega$, $Z_{21} = 138.0\ \Omega$, $Z_{22} = 20.8\ \Omega$, $Z_{31} = 137.9\ \Omega$, $Z_{32} = 24.0\ \Omega$. The four resonant frequencies can then be calculated from (5.1) with $N = 4$. They are here located at $f_{zr1} = 1.410$ GHz, $f_{r2} = 1.800$ GHz, $f_{r3} = 2.155$ GHz and $f_{r4} = 2.555$ GHz. The J inverters impedance values are with $Z_{J01} = Z_{J34} = 78.0\ \Omega$, $Z_{J12} = Z_{J23} = 138.5\ \Omega$.

Fig. 5.8 shows theoretical responses of the proposed quad-band ABSR (a) and quad-band filter. As highlighted for the tri-band case, the ripple is not perfectly constant for all pass-bands, but it has little influence on the performance of the filter and the final response is in accordance with the specifications. For this filter, the maximum level of the reflection coefficient in pass-band regions is about 20 dB.

The proposed filter has been also implemented in microstrip technology using a RO4003C Rogers substrate. Fig. 5.9(a) presents a schematic view of the quad-band band-pass filter. The dimensions of the filter are shown in Table 5.3. Fig. 5.9(b) presents the EM simulated and measured filter's responses. The fabricated filter's size is 101.5×100.1 mm^2 without taking into account the two 50 Ω access lines. We can observe good in-band responses and excellent band-to-band isolation of about 60 dB between each pass-band. The measured return loss for each band is better than 18.9 dB, 17.6 dB, 17.7 dB and 12.3 dB respectively. The measured insertion loss from the first pass-band to the fourth pass-band are 1.40 dB, 1.75 dB, 2.53 dB and 2.10 dB respectively.

5.2.4 Quint-band band-pass filter

As a last example, a quint-band band-pass filter based on the proposed ABSRs is presented in this section in order to show the general aspect of the proposed solution. The filter design follows the same steps as for the quad-band band-pass filter presented. The arbitrary specifications we have chosen for this example are:

1. Pass-band 1: 1.40 GHz-1.52 GHz (BW: 120 MHz);

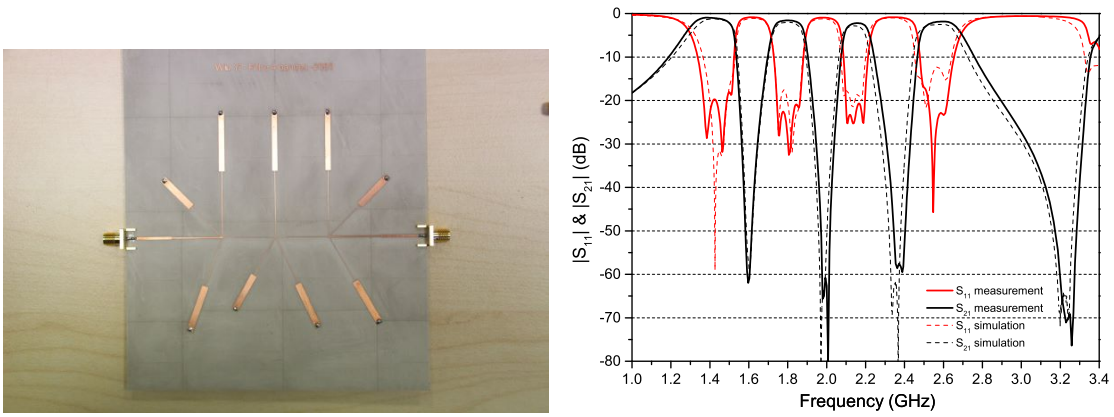

(a) (b)

Figure 5.9 – The fabricated quad-band circuit (a) its EM-simulated (solid lines) and measured (dotted lines) S-parameters (b).

2. Pass-band 2: 1.72 GHz-1.82 GHz (BW: 100 MHz);
3. Pass-band 3: 1.98 GHz-2.05 GHz (BW: 70 MHz);
4. Pass-band 4: 2.24 GHz-2.33 GHz (BW: 90 MHz);
5. Pass-band 5: 2.56 GHz-2.63 GHz (BW: 70 MHz).

First of all, we choose the four TZs at $f_{z1} = 1.60$ GHz, $f_{z2} = 1.85$ GHz, $f_{z3} = 2.2$ GHz, and $f_{z4} = 2.5$ GHz respectively. We also have $f_{z6} = 3.20$ GHz. The impedance values of the ABSRs are then chosen following the same procedure and constraints as in three previous cases. For this example the impedance values are: $Z_{11} = 140.8\ \Omega$, $Z_{12} = 30.0\ \Omega$, $Z_{21} = 135.0\ \Omega$, $Z_{22} = 22.5\ \Omega$, $Z_{31} = 138.1\ \Omega$, $Z_{32} = 22.4\ \Omega$, $Z_{41} = 140.0\ \Omega$, $Z_{42} = 21.0\ \Omega$. The five resonant frequencies can then be calculated from (5.1) with $N = 5$. They are here located at $f_{r1} = 1.460$ GHz, $f_{r2} = 1.744$ GHz, $f_{r3} = 2.014$ GHz, $f_{r4} = 2.300$ GHz and $f_{r5} = 2.609$ GHz as shown in Fig. 5.10(a) with the following J inverters values : $Z_{J01} = Z_{J34} = 82.5\ \Omega$, $Z_{J12} = Z_{J23} = 137.8\ \Omega$. Fig. 5.10(b) shows the theoretical response of the proposed quint-band filter with optimized J values. Again, it is in good accordance with the specifications.

This filter was fabricated under the same conditions as the other ABSR-based filters (See Fig. 5.11(a)). The fabricated filter's details size information is shown in Table 5.4. The overall size of the filter is 113.4×93.5 mm^2 without taking into account the two 50 Ω access lines. EM simulations and measurements are in good agreement as shown in Fig. 5.11(b). Good in-band behaviours and excellent band-to-band isolation better than 50 dB are obtained. The measured return loss from the first band to the last one are better than 20.0 dB, 16.2 dB, 12.9 dB, 12.4 dB and 10.3 dB, successively. The measured insertion loss for each individual pass-band is 1.72 dB, 3.22 dB, 3.63 dB, 3.81 dB and 3.37 dB, successively.

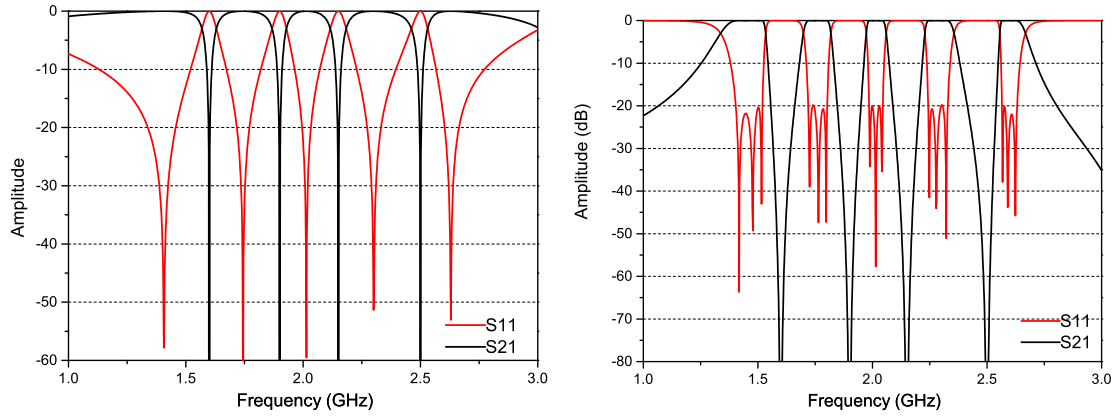

(a) (b)

Figure 5.10 – Quint-band Star-like Resonators S parameters (a); idea responses of the quad-band bandpass filter (b).

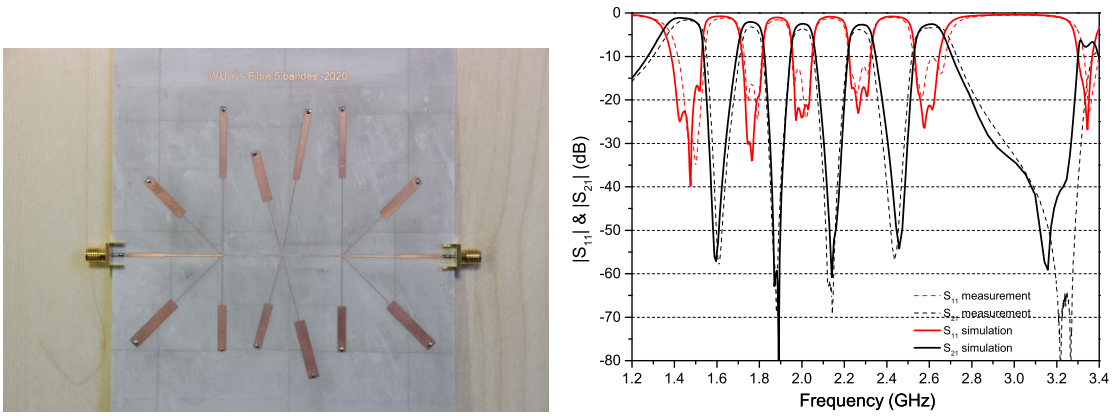

(a) (b)

Figure 5.11 – Picture of the quint-band circuit (a) and its EM-simulated (solid lines) and measured (dotted lines) S-parameters (b).

Table 5.4 – Dimension of the quint-band band-pass filters with ABSR.

Symbol	Values (mm)	Symbol	Values (mm)
L_{J01}	22.05	W_{J01}	0.53
L_{J02}	22.83	W_{J02}	0.12
L_{11}	29.83	W_{11}	0.12
L_{12}	27.18	W_{12}	2.38
L_{21}	25.90	W_{21}	0.11
L_{22}	22.0	W_{22}	4.02
L_{31}	21.80	W_{231}	0.12
L_{32}	17.40	W_{32}	3.54
L_{41}	19.20	W_{41}	0.10
L_{42}	17.22	W_{42}	3.00

In order to reflect the characteristics of the MBPFs based on ABSR with hign number of pass-bands, Table 5.5 gives a performance comparison of the proposed quad and quint-band MBPFs with some previous works available in the literature. Different characteristics are given: the filter order, the TZs performance (CTZs) (controllable or not), the center frequency (CF), the insertion loss (IL), the 3-dB bandwidth, the band-to-band isolation (ISO) between the i^{th} and $(i+1)^{th}$ pass-band ($i \in [1;4]$) and the total filter sizes (λ_g is the guided wavelength at the center frequency of all bands). Despite some limitations (total frequency range limited by the first harmonic of the first TZ, non-constant matching level), our proposed design method exhibits several advantages with respect to the former ones. First, the TZs between the bands are totally controllable for the proposed two cases. This is a great advantage compared with most of filters. Second, a few MBPFs can achieve high-order filtering responses. Our proposed method is adequate to achieve high-order and high numbers of pass-bands with a simple implementation method. Third, the band-to-band isolation is better than all existing MBPFs. Fourth, compared to coupled structure solutions, the proposed synthesis methods needs less optimization due to a low number of parameters, which is really important for a quick design of MBPFs with high-order responses.

A sixfold-band band-pass filter with 2^{nd}-order response is also described in Appendix 7.5 to show the generalization of this method. To have more pass-bands, the multilayer PCB configuration may be used to make implementations as presented in chapter 3 (section 3.2.2).

5.3 Conclusion

In this chapter, we proposed a simple but powerful synthesis method using ABSRs to design MBPFs. Five examples with dual-band to sext-band band-pass filters based on the proposed ABSRs were studied, simulated, implemented in microstrip technology and measured. Good in-

Table 5.5 – Comparisons with the other quad-,quint-band MBPFs.

Ref.	PB	Filter order	CTZs	CF (GHz)	IL (dB)	ISO (dB)	BW% (3dB)	Size ($\lambda_g \times \lambda_g$)
[57]	4	2	No	1.91/3.55 5.36/6.92	0.6/1.65 1.05/1.85	ISO_{12}>25, ISO_{23}>13 ISO_{34}>20	16.5/6.9 7.4/5.4	0.23×0.12
[58]	4	2	No	0.96/2.51 3.71/5.11	0.12/0.7 0.3/0.53	ISO_{12}>19, ISO_{23}>19 ISO_{34}>19	109.4/30.4 5.11/35.2	0.14×0.14
[59]	4	2	No	0.96/2.51 3.71/5.11	0.12/0.7 0.3/0.53	ISO_{12}>22, ISO_{23}>40 ISO_{34}>23	6.9/9.4 3.8/4.9	0.2×0.2
[60]	4	2	No	0.96/2.51 3.71/5.11	0.12/0.7 0.3/0.53	ISO_{12}>40, ISO_{23}>40 ISO_{34}>30	6.7/4.2 3.7/14.8	0.19×0.15
This work	4	3	Yes	1.44/1.80 2.14/2.54	1.40/1.75 2.10/2.53	ISO_{12}>61.3 ISO_{23}>62.2 ISO_{34}>61.8	20.64/11.22 8.46/10.61	0.64×0.63
[57]	5	2	No	0.62/1.33 2.03/2.75 3.45	0.47/1.14 1.80/1.39 1.26	ISO_{12}>32, ISO_{23}>13 ISO_{34}>20,ISO_{45}>15	28.8/9.4 2.7/5.3 5.5	0.04×0.18
[58]	5	2	No	0.94/2.42 3.7/4.6 5.75	0.12/0.68 0.28/0.65 0.57	ISO_{12}>15, ISO_{23}>15 ISO_{34}>15,ISO_{45}>15	110.6/33.5 17.6/16 20	0.14×0.14
[61]	5	2	No	1.5/2.5 3.5/4.5 5.8	1.5/1.8 0.9/1.2 2.5	ISO_{12}>35, ISO_{23}>30 ISO_{34}>35,ISO_{45}>30	4.5/4.5 3.6/4.5 2.7	0.24×0.17
[62]	5	3	No	0.6/0.9 1.2/1.5 1.8	2.8/2.9 2.9/2.6 2.3	ISO_{12}>28, ISO_{23}>26 ISO_{34}>30,ISO_{45}>15	5.8/5.2 5.8/8.2 8	0.22×0.05
This work	5	3	Yes	1.46/1.77 2.01/2.28 2.60	1.72/3.22 3.63/3.81 3.37	ISO_{12}>56.8 ISO_{23}>60.1 ISO_{34}>61.4 ISO_{45}>55.6	14.31/8.64 6.10/6.47 5.83	0.72×0.60

band responses and high band-to-band isolation are easily obtained with this simple procedure. However, there are also some drawbacks in this method. Filters occupy relatively large surface with respect to coupled-line filters. There are uncontrollable TZs before the first and last pass-bands. They are difficult to implement with other techniques. Some deeper research may need to be done to deal with these problems. However, conversely to the methods presented in chapters 3 and 4, this method is not analytical and need some optimization operations as soon as the ideal filter is developed. Nevertheless, these optimizations are relatively simple and do not need a lot of time.

Chapter 6

Conclusion and perspectives

6.1 Conclusion

In this dissertation, we mainly focused on theoretical and practical aspects of multiband band-pass filters (MBPFs) in planar microstrip technology. We developed the theory of a generalized frequency transformation. Based on the proposed approach, several examples have been successfully implemented with non-coupled and coupled structures. A new type of transformation function in an in-line topology was proposed. Two methods have been used to solve the transfer function and illustrated by coupled-line filters. We also discussed the design of MBPFs based on ABSRs, Some verifications are also presented. The major contributions of this research are outlined as follows:

* First, in chapter 3, we present a generalized synthesis method for designing MBPF with a frequency transformation approach. Generalized analytical equations are presented for the construction of multiband filters with an arbitrary number of pass-bands. Several synthesis examples are also presented to illustrate the well-established theory. We also propose some examples the star-like implementation thus obtained with non-coupled and coupled structures. Very good filters performance have been observed for all the proposed MBPFs.
* Second, in chapter 4, we propose a novel transformation function to synthesis MBPFs in an in-line topology. Based on this transformation function, MBPFs up to sext-band were synthesized, designed, and measured. Measurement are fully consistent with theory.
* Third, in chapter 5, we present a simple method to quickly design MBPFs using ABSRs. It simplify the frequency transformation method with star-like topology without sacrificing filter performance. Filters up to sext-band were presented to demonstrate the proposed approach.

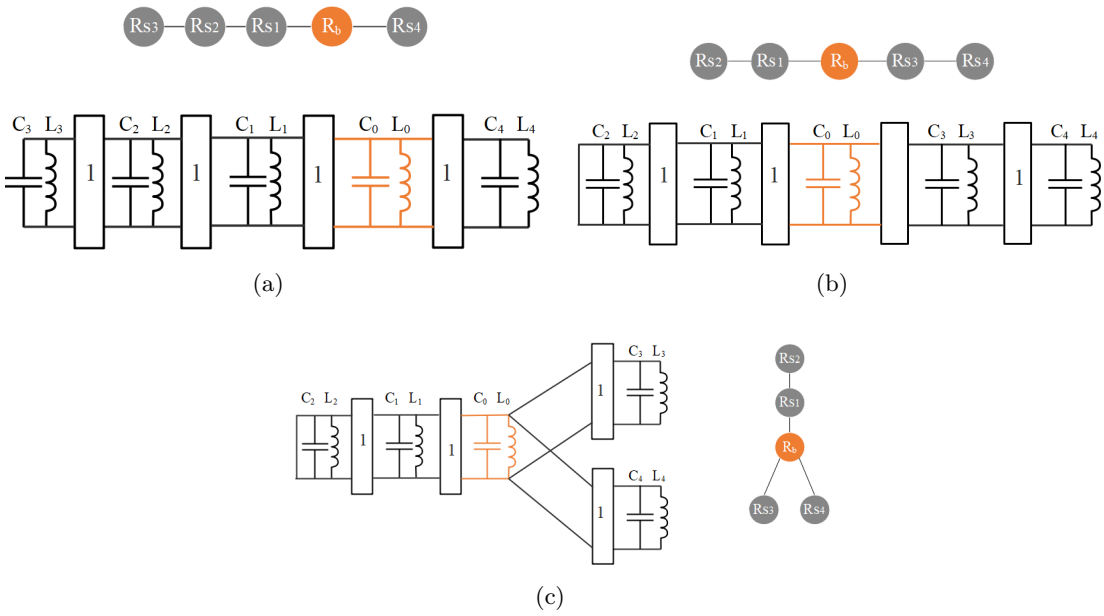

Figure 6.1 – Quint-band band-pass filter with mixed topology- mixed topology (a), (b) and (c).

6.2 Perspectives

6.2.1 Multiband filters with mixed topology

Besides the star-like and in-line topology, MBPFs can also be synthesized from mixed frequency transformation method. The mixed approach can be regarded as the mixture of the star-like and in-line topologies. The mixed frequency transformation can be expressed as:

$$\Omega = T^{(m)}(\omega) = b_0\left(\frac{\omega}{\omega_0} - \frac{\omega_0}{\omega}\right)$$
$$-\frac{1}{b_1\left(\frac{\omega}{\omega_1} - \frac{\omega_1}{\omega}\right) - \frac{1}{b_2\left(\frac{\omega}{\omega_2} - \frac{\omega_2}{\omega}\right)\cdots - \frac{1}{b_l\left(\frac{\omega}{\omega_l} - \frac{\omega_l}{\omega}\right)}}} - \frac{1}{b_{l+1}\left(\frac{\omega}{\omega_{l+1}} - \frac{\omega_{l+1}}{\omega}\right)} - \frac{1}{b_m\left(\frac{\omega}{\omega_m} - \frac{\omega_m}{\omega}\right)} - \ldots, \quad (6.1)$$

This transform function is composed of three terms: The first term on the right side of 6.1 is the transformed band-pass filters (b_0 and ω_0); the second term corresponds to the in-line topology (b_1 to b_l, ω_1 to ω_l); the last term is the star-like topology (b_{l+1} to b_m, ω_{l+1} to ω_m). As we described in chapter 4, there are two ways to extract the parameters of the proposed transform function with star and in-line topology. Nevertheless, for a mixed frequency transformation case, the transformed network can not be regarded as ladder networks anymore: frequency mapping technique may be used to extract circuit values. For implementation, In this thesis, we main focus on planar technoniques. However, the microstrip technology is limited by its Q-factors, which may case great insertion losses when pass-bands become narrow. As a promising

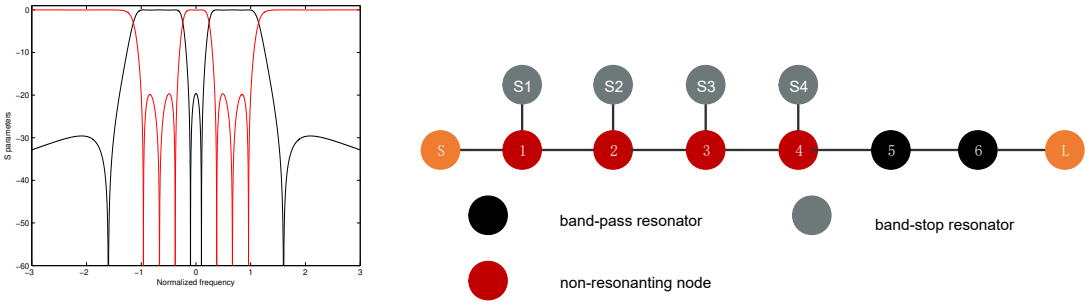

(a) (b)

Figure 6.2 – (a) dual-band band-pass filter with four TZs ($\pm 1.6j$ and $\pm 0.1j$) theoretically responses in normalized frequency; (b) topology based on extracted pole method.

platform, the substrate integrated waveguide (SIW) represents a relevant candidate for the design of microwave and millimeter wave component due to high power handling capacity, light weight, and relative high Q factors. SIW could be well adopted to the implementation of the mixed topology.

6.2.2 Multiband band-pass filter based on extracted pole technique

Extracted pole filters are fast growing solutions for the manufacture of microwave filters with several transmission zeros [63, 64, 65, 66, 67, 68]. Extracted pole filter is a more efficient technique than the classical cross-coupled filter as the number of TZs increases. Another good reason for studying this technique is to implement TZs in an inline or quasi-inline topology. This is a very fascinating choice for a high selective filter involving about the same number of resonators [67, 68]. For multiband cases, for a giving filtering function, which contains the poles and TZs information, we can use the circuit approach described in [69] to extract the circuit values for each band-pass, band-stop resonator and non-resonating node step by step. Finally, this extracted circuits could be implemented by various techniques.

Fig. 6.2(a) presents a dual-band third order elliptic filter (4 TZs and 6 poles) and its potential implementation by using an in-line topology with extracted-pole method. The band-pass resonators (resonators 5-6) provide two poles and the non-resonating nodes (1-4) provide another 4 poles. The four TZs can be created by band-stop resonators ($S_1 - S_4$). Such a method could be a great opportunity to design high performance multiband filters with strict specifications in terms of rejected bands, in particular. Coparing this method to frequency transformation method. MBPFs based on frequency transformation methods can not control the in-band TZs. Also, MBPFs with arbitrary placed in-band TZs are rarely reported. So, with great interest, the extracted pole technique could be used for the synthesis multiband filter with flexible TZs. Moreover, the miniaturization of filters has always been a research hotspot.

The employment of extracted-pole method may reduce the number of resonators to achieve a minimized footprint.

Chapter 7

Appendix

7.1 Expression governing the resonant angular frequencies of the band-stop resonators

As presented in Chapter 3, the resonant angular frequencies of the stop-band parts of an N-band band-pass resonator (MBPR) are the positive solutions of (3.16).

Proof : In the case of an N-band band-pass filters, the coefficients n_p of the $U^{(N)}(\omega)$ function (see (3.5)) are given by (3.12) in the case of an odd value of p ($p = 2q-1$, $q \in [1; N]$).

For $q = N$ and so $p = 2N-1$, this equation leads to:

$$n_{2N-1} = -\frac{\omega_0}{b_0} \tag{7.1}$$

knowing that $\mathcal{P}_0\left(\mathcal{W}^{(1\to N-1)}\right) = 1$ as defined in Section 3.1.1. So, (3.12) becomes:

$$\begin{aligned} n_p &= n_{2q-1} \\ &= (-1)^{N-q}\, n_{2N-1}\mathcal{P}_{N-q}\left(\mathcal{W}^{(1\to N-1)}\right) \end{aligned} \tag{7.2}$$

Applying (7.2) with $q = N-1$ ($p = 2N-3$) leads to:

$$n_{2N-3} = -n_{2N-1}\mathcal{P}_1\left(\mathcal{W}^{(1\to N-1)}\right) \tag{7.3}$$

Considering any angular frequency of the stop-band parts ω_k, $k \in [1; N-1]$, this expression can be written as follow:

$$n_{2N-3} = -n_{2N-1}\left[\mathcal{P}_1\left(\mathcal{W}_{\{k\}}^{(1\to N-1)}\right) + \omega_k^2\right] \tag{7.4}$$

which implies that:

$$n_{2N-1}\mathcal{P}_1\left(\mathcal{W}_{\{k\}}^{(1\to N-1)}\right) = -\left[n_{2N-3} + n_{2N-1}\omega_k^2\right] \tag{7.5}$$

In the same way, for $q = N-2$ ($p = 2N-5$), (7.2) becomes:

$$\begin{aligned} n_{2N-5} &= n_{2N-1}\mathcal{P}_2\left(\mathcal{W}^{(1\to N-1)}\right) \\ &= n_{2N-1}\left[\mathcal{P}_2\left(\mathcal{W}_{\{k\}}^{(1\to N-1)}\right) + \omega_k^2\mathcal{P}_1\left(\mathcal{W}_{\{k\}}^{(1\to N-1)}\right)\right] \\ &= n_{2N-1}\mathcal{P}_2\left(\mathcal{W}_{\{k\}}^{(1\to N-1)}\right) - \left[n_{2N-3}\omega_k^2 + n_{2N-1}\omega_k^4\right] \end{aligned} \tag{7.6}$$

which leads to:

$$n_{2N-1}\mathcal{P}_2\left(\mathcal{W}_{\{k\}}^{(1\to N-1)}\right) = n_{2N-5} + n_{2N-3}\omega_k^2 + n_{2N-1}\omega_k^4 \tag{7.7}$$

Continuing thus for the other values of q from $N-1$ to 1, one can show that:

$$n_{2N-1}\mathcal{P}_{N-q}\left(\mathcal{W}_{\{k\}}^{(1\to N-1)}\right) = \sum_{r=0}^{N-q} n_{2(q+r)-1}\omega_k^{2r} \tag{7.8}$$

Let's focus now on the case $q = 1$ ($p = 1$). First, using (7.2), we have:

$$\begin{aligned} n_1 &= (-1)^{N-1}n_{2N-1}\mathcal{P}_{N-1}\left(\mathcal{W}^{(1\to N-1)}\right) \\ &= (-1)^{N-1}\omega_k^2 n_{2N-1}\mathcal{P}_{N-2}\left(\mathcal{W}_{\{k\}}^{(1\to N-1)}\right) \end{aligned} \tag{7.9}$$

Using (7.8), this expression becomes

$$\begin{aligned} n_1 &= (-1)^{N-1}\omega_k^2\frac{1}{(-1)^{N-2}}\sum_{r=0}^{N-2} n_{2r+3}\omega_k^{2r} \\ &= -\sum_{r=1}^{N-1} n_{2r+1}\omega_k^{2r} \end{aligned} \tag{7.10}$$

Therefore, we obtain the equation governing the resonant angular frequencies of the band-stop resonators :

$$\sum_{r=0}^{N-1} n_{2r+1}\omega_k^{2r} = 0 \tag{7.11}$$

This equation has $2(N-1)$ solutions, one half being positive and the other half negative. Of course, in this case, only the positive solutions are retained.

7.2 Resonant angular frequencies and slope parameters for quad-band band-pass to sext-band band-pass filter.

Resonating angular frequencies and slope parameters for quad-band band-pass filters in a star-like topology.

$$\omega_0 = \sqrt{\frac{-n_0 n_7}{n_1}} \tag{7.12}$$

$$\omega_1 = \sqrt{-\frac{n_5}{3n_7} + \sqrt[3]{\Omega_1} + \sqrt[3]{\Omega_2}} \tag{7.13}$$

$$\omega_2 = \sqrt{-\frac{n_5}{3n_7} + \Delta_3\sqrt[3]{\Omega_1} + \Delta_4\sqrt[3]{\Omega_2}} \tag{7.14}$$

$$\omega_3 = \sqrt{-\frac{n_5}{3n_7} + \Delta_4\sqrt[3]{\Omega_1} + \Delta_3\sqrt[3]{\Omega_2}} \tag{7.15}$$

$$b_0 = \sqrt{\frac{-n_0}{n_1 n_7}} \tag{7.16}$$

$$b_1 = \frac{\omega_1(\omega_1^2 - \omega_2^2)(\omega_1^2 - \omega_3^2)}{Y_3\omega_1^4 + Y_2\omega_1^2 + Y_1} \tag{7.17}$$

$$b_2 = \frac{\omega_2(\omega_2^2 - \omega_1^2)(\omega_2^2 - \omega_3^2)}{Y_3\omega_2^4 + Y_2\omega_2^2 + Y_1} \tag{7.18}$$

$$b_3 = \frac{\omega_3(\omega_3^2 - \omega_1^2)(\omega_3^2 - \omega_2^2)}{Y_3\omega_3^4 + Y_2\omega_3^2 + Y_1} \tag{7.19}$$

where:

$$\Omega_1 = \Delta_1 + \sqrt{\Delta_1^2 + \Delta_2^3} \tag{7.20}$$

$$\Omega_2 = \Delta_1 - \sqrt{\Delta_1^2 + \Delta_2^3} \tag{7.21}$$

$$\Delta_1 = \frac{n_5 n_3}{6n_7^2} - \frac{n_5^3}{27n_7^3} - \frac{n_1}{2n_7} \tag{7.22}$$

$$\Delta_2 = \frac{n_3}{3n_7} - \frac{n_5^2}{9n_7^2} \tag{7.23}$$

$$\Delta_3 = \frac{-1 + j\sqrt{3}}{2} \tag{7.24}$$

$$\Delta_4 = \frac{-1 - j\sqrt{3}}{2} \tag{7.25}$$

$$Y_1 = \frac{n_2 - \frac{n_0 n_3}{n_1} - \frac{n_1}{n_7}}{n_7} \tag{7.26}$$

$$Y_2 = \frac{n_4 - \frac{n_0 n_5}{n_1} - \frac{n_3}{n_7}}{n_7} \tag{7.27}$$

$$Y_3 = \frac{n_6 - \frac{n_0 n_7}{n_1} - \frac{n_5}{n_7}}{n_7} \tag{7.28}$$

Resonant angular frequencies and slope parameters for quint-band band-pass filters in a star-like topology.

$$\omega_0 = \sqrt{-\frac{n_0 n_9}{n_1}} \tag{7.29}$$

$$\omega_1 = \sqrt{-\frac{n_7}{4n_9} - \frac{1}{2}(\sqrt{R_0} + \sqrt{R_1})} \tag{7.30}$$

$$\omega_2 = \sqrt{-\frac{n_7}{4n_9} - \frac{1}{2}(\sqrt{R_0} - \sqrt{R_1})} \tag{7.31}$$

$$\omega_3 = \sqrt{-\frac{n_7}{4n_9} + \frac{1}{2}(\sqrt{R_0} - \sqrt{R_1})} \tag{7.32}$$

$$\omega_4 = \sqrt{-\frac{n_7}{4n_9} + \frac{1}{2}(\sqrt{R_0} + \sqrt{R_1})} \tag{7.33}$$

where:

$$R_0 = (\frac{n_7}{2n_9})^2 - \frac{2n_5}{3n_9} + R_3 + \frac{n_2^5 - 3n_3 n_7 + 12 n_1 n_9}{(3n_9)^2 R_3} \tag{7.34}$$

$$R_2 = (\frac{n_7}{2n_9})^2 - \frac{2n_5}{3n_9} - R_3 - \frac{n_2^5 - 3n_3 n_7 + 12 n_1 n_9}{(3n_9)^2 R_3} \tag{7.35}$$

$$R_3 = \frac{R_5}{3n_9 \sqrt[3]{2(R_4 + \sqrt{(R_4^2 - 4R_5^3)})}} \tag{7.36}$$

$$\begin{aligned} R_4 = 2n_7^2 - 9n_3n_5n_7 + 27n_3^2n_9 \\ +27n_7^2n_1 - 72n_1n_5n_9 \end{aligned} \tag{7.37}$$

$$R_1 = R_2 - \frac{4n_5n_7n_9 - n_7^3 - 8n_3n_9^2}{4n_9^3\sqrt{R_0}} \tag{7.38}$$

$$R_5 = n_5^2 - 3n_3n_7 + 12n_1n_9 \tag{7.39}$$

Resonant angular frequencies and slope parameters for sext-band band-pass filters in a star-like topology.

$$b_0 = \sqrt{-\frac{n_1}{n_0n_9}} \tag{7.40}$$

$$b_1 = \frac{\omega_1(\omega_1^2 - \omega_2^2)(\omega_1^2 - \omega_3^2)(\omega_1^2 - \omega_4^2)}{Y_4\omega_1^6 + Y_3\omega_1^4 + Y_2\omega_1^2 + Y_1} \tag{7.41}$$

$$b_2 = \frac{\omega_2(\omega_2^2 - \omega_1^2)(\omega_2^2 - \omega_3^2)(\omega_2^2 - \omega_4^2)}{Y_4\omega_2^6 + Y_3\omega_2^4 + Y_2\omega_2^2 + Y_1} \tag{7.42}$$

$$b_3 = \frac{\omega_3(\omega_3^2 - \omega_1^2)(\omega_3^2 - \omega_2^2)(\omega_3^2 - \omega_4^2)}{Y_4\omega_3^6 + Y_3\omega_3^4 + Y_2\omega_3^2 + Y_1} \tag{7.43}$$

$$b_4 = \frac{\omega_4(\omega_4^2 - \omega_1^2)(\omega_4^2 - \omega_2^2)(\omega_4^2 - \omega_3^2)}{Y_4\omega_4^6 + Y_3\omega_4^4 + Y_2\omega_4^2 + Y_1} \tag{7.44}$$

$$Y_1 = \frac{n_2 - \dfrac{n_0n_3}{n_1} - \dfrac{n_1}{n_9}}{n_9} \tag{7.45}$$

$$Y_2 = \frac{n_4 - \dfrac{n_0n_5}{n_1} - \dfrac{n_3}{n_9}}{n_9} \tag{7.46}$$

$$Y_3 = \frac{n_6 - \dfrac{n_0n_7}{n_1} - \dfrac{n_5}{n_9}}{n_9} \tag{7.47}$$

$$Y_4 = \frac{n_8 - \dfrac{n_0n_9}{n_1} - \dfrac{n_7}{n_9}}{n_9} \tag{7.48}$$

$$n_{11}\omega^{11} - n_9\omega^9 + n_7\omega^7 - n_5\omega^5 + n_3\omega^3 - n_1\omega = 0 \tag{7.49}$$

$$\omega_0 = \sqrt{\frac{-n_0 n_1 1}{n_1}}, \tag{7.50}$$

$$b_0 = \sqrt{-\frac{n_1}{n_0 n_{11}}} \tag{7.51}$$

$$b_1 = \frac{\omega_1(\omega_1^2-\omega_2^2)(\omega_1^2-\omega_3^2)(\omega_1^2-\omega_4^2)(\omega_1^2-\omega_5^2)}{X\omega_1^8 + Y\omega_1^6 + Z\omega_1^4 + W\omega_1^2 + V} \tag{7.52}$$

$$b_2 = \frac{\omega_2(\omega_2^2-\omega_1^2)(\omega_2^2-\omega_3^2)(\omega_2^2-\omega_4^2)(\omega_2^2-\omega_5^2)}{X\omega_2^8 + Y\omega_2^6 + Z\omega_2^4 + W\omega_2^2 + V} \tag{7.53}$$

$$b_3 = \frac{\omega_3(\omega_3^2-\omega_1^2)(\omega_3^2-\omega_2^2)(\omega_3^2-\omega_4^2)(\omega_3^2-\omega_5^2)}{X\omega_3^8 + Y\omega_3^6 + Z\omega_3^4 + W\omega_3^2 + V} \tag{7.54}$$

$$b_4 = \frac{\omega_4(\omega_4^2-\omega_1^2)(\omega_4^2-\omega_2^2)(\omega_4^2-\omega_3^2)(\omega_4^2-\omega_5^2)}{X\omega_4^8 + Y\omega_4^6 + Z\omega_4^4 + W\omega_4^2 + V} \tag{7.55}$$

$$b_5 = \frac{\omega_5(\omega_5^2-\omega_1^2)(\omega_5^2-\omega_2^2)(\omega_5^2-\omega_3^2)(\omega_5^2-\omega_4^2)}{X\omega_5^8 + Y\omega_5^6 + Z\omega_5^4 + W\omega_5^2 + V} \tag{7.56}$$

$$X = \frac{n_{10} - \frac{n_0 n_{11}}{n_1} - \frac{n_9}{n_{11}}}{n_{11}} \tag{7.57}$$

$$Y = \frac{n_8 - \frac{n_0 n_9}{n_1} - \frac{n_7}{n_{11}}}{n_{11}} \tag{7.58}$$

$$Z = \frac{n_6 - \frac{n_0 n_7}{n_1} - \frac{n_5}{n_{11}}}{n_{11}} \tag{7.59}$$

$$W = \frac{n_4 - \frac{n_0 n_5}{n_1} - \frac{n_3}{n_{11}}}{n_{11}} \tag{7.60}$$

$$V = \frac{n_2 - \frac{n_0 n_3}{n_1} - \frac{n_1}{n_{11}}}{n_{11}} \tag{7.61}$$

$$\tag{7.62}$$

7.3 Star-like multiband filters: characteristics, layout and additional realization

Characteristics of the quad-band band-pass filter with different bandwidths

Table 7.1 – Component values of the ideal L-C quad-band third-order band-pass filter.

Resonators ($i \in [1;3]$)		
$L_0^{(i)} = 1.602$ nH	$L_1^{(i)} = 1.874$ nH	$L_2^{(i)} = 1.645$ nH
$L_3^{(i)} = 1.388$ nH	$L_4^{(i)} = 1.241$ nH	
$C_0^{(i)} = 2.436$ pF	$C_1^{(i)} = 2.850$ pF	$C_2^{(i)} = 2.502$ pF
$C_3^{(i)} = 2.333$ pF	$C_4^{(i)} = 2.080$ pF	
$J_1^{(i)} = 0.0070$ S	$J_2^{(i)} = 0.0072$ S	
$J_3^{(i)} = 0.0069$ S	$J_4^{(i)} = 0.0064S$	
Inverters ($J_{i,i+1}$)		
$J_{01} = J_{34} = 0.013$ S	$J_{12} = J_{23} = 0.0069$ S	

Table 7.2 – Microstrip quad-band third-order band-pass filter: length and width dimensions *(in mm)*.

Resonators			
$L_0 = 16.70$	$L_1 = 19.01$	$L_2 = 16.2$	$L_3 = 15.30$
$W_0 = 1.30$	$W_1 = 3.80$	$W_2 = 3.30$	$W_3 = 3.51$
$L_{J1} = 21.30$	$L_{J2} = 18.40$	$L_{J3} = 15.70$	
$W_{J1} = 0.11$	$W_{J2} = 0.12$	$W_{J3} = 0.10$	
Inverters			
$L_{01} = 19.23$	$L_{12} = 19.85$		
$W_{01} = 0.51$	$W_{12} = 0.11$		

Quad-band band-pass filter with equal bandwidths

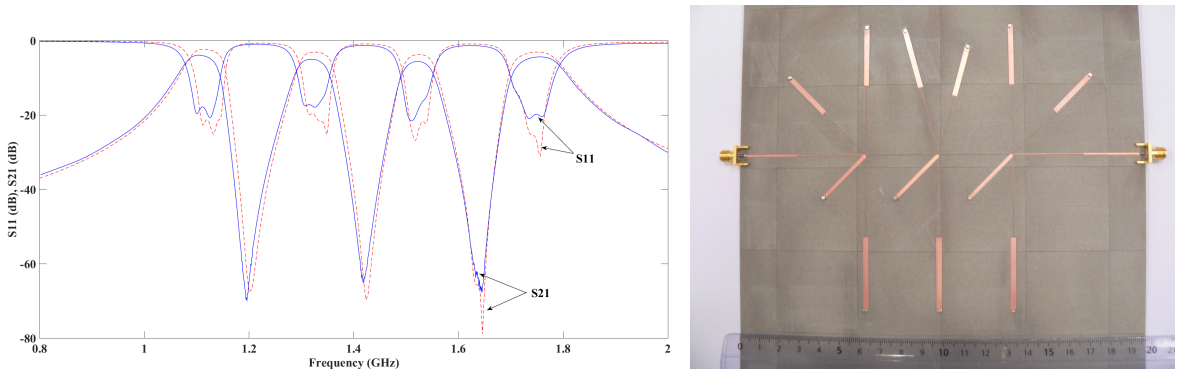

(a) (b)

Figure 7.1 – EM-simulated (dotted lines) and measured (solid lines) S-parameters of the quad-band band-pass filter with same bandwidth (a); picture of the fabricated quad-band filter (b).

Sixfold-band band-pass filter layout and dimensions

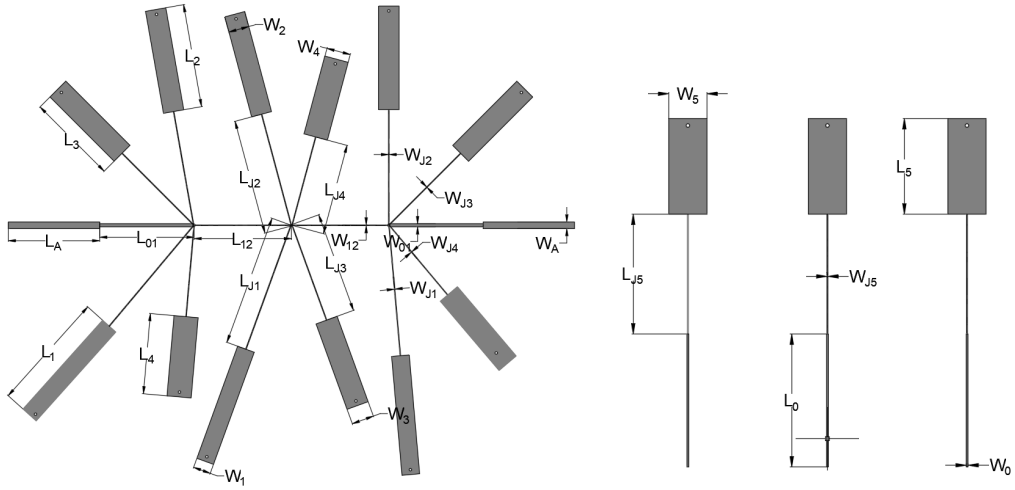

(a) (b)

Figure 7.2 – Dimension of the proposed sixfold-band band-pass filter: (a) top layer and (b) bottom layer.

Table 7.3 – Microstrip sixfold-band third-order band-pass filter: length and width dimensions.

Resonators		
$L_0 = 15.30$	$L_1 = 19.70$	$L_2 = 17.10$
$W_0 = 0.30$	$W_1 = 2.92$	$W_2 = 3.42$
$L_3 = 15.00$	$L_4 = 13.30$	$L_5 = 11.05$
$W_3 = 3.97$	$W_4 = 2.92$	$W_5 = 4.40$
$L_{J1} = 21.80$	$L_{J2} = 19.10$	$L_{J3} = 16.80$
$W_{J1} = 0.10$	$W_{J2} = 0.12$	$W_{J3} = 0.10$
$L_{J4} = 15.10$	$L_{J5} = 13.80$	
$W_{J4} = 0.009$	$W_{J5} = 0.008$	
Inverters		
$L_{01} = 15.60$	$L_{12} = 16.12$	
$W_{01} = 0.55$	$W_{12} = 0.11$	

7.4 In-line topology sets of synthesis equations for tri-band and quad-band with the frequency mapping technique

Tri-band:

For triple band case, the frequency transformation function can be rewritten as:

$$U^{(3)}(\omega) = \frac{\omega^6 + \sum_{p=0}^{5} n_p \omega^p}{-(n_5\omega^5 + n_3\omega^3 + n_1\omega)} \tag{7.63}$$

Using the mapping principles, the following synthesis equations can be obtained

$$\omega_0 = \sqrt{\frac{-n_0 n_5}{n_1}}, \tag{7.64}$$

$$\omega_1 = \sqrt{\frac{-n_1}{n_5}\frac{X_1}{X_2}} \tag{7.65}$$

$$\omega_2 = \sqrt{-\frac{X_2}{X_1}} \tag{7.66}$$

$$b_0 = \sqrt{\frac{-n_0}{n_1 n_5}} \tag{7.67}$$

$$b_1 = \sqrt{\frac{\omega_1}{X_1}} \tag{7.68}$$

$$b_2 = \frac{\omega_2 X_1}{\frac{n_1}{n_5}\frac{X_1}{X_2} + \frac{X_2}{X_1} - \frac{n_3}{n_5}} \tag{7.69}$$

where

$$X_1 = \frac{n_4 - \frac{n_0 n_5}{n_1} - \frac{n_3}{n_5}}{n_5} \tag{7.70}$$

$$X_2 = \frac{n_2 - \frac{n_0 n_3}{n_1} - \frac{n_1}{n_3}}{n_5} \tag{7.71}$$

Quad-band:

In the quad-band case, the transformation function is:

$$U^{(4)}(\omega) = \frac{\omega^8 + \sum_{p=0}^{7} n_p \omega^p}{-(n_7\omega^7 + n_5\omega^5 + n_3\omega^3 + n_1\omega)} \tag{7.72}$$

Using the same mapping principle as mentioned above, the following synthesis equations can also be expressed in the quad-band case as follow:

$$\omega_0 = \sqrt{\frac{-n_0 n_7}{n_1}} \tag{7.73}$$

$$b_0 = \sqrt{\frac{-n_0}{n_1 n_7}} \tag{7.74}$$

$$\omega_1 = \sqrt{\frac{-n_1}{n_7}\frac{X_1}{X_3}} \tag{7.75}$$

$$\omega_2 = -\sqrt{-\frac{X_3}{X_1}\frac{\frac{n_5}{n_7} - \frac{n_1}{n_7}\frac{X_1}{X_3} - \frac{X_2}{X_1}}{\frac{n_3}{n_7} - \frac{n_1}{n_7}\frac{X_2}{X_3} - \frac{X_3}{X_1}}} \tag{7.76}$$

$$\omega_3 = \sqrt{-\frac{\frac{n_3}{n_7} - \frac{n_1}{n_7}\frac{X_2}{X_3} - \frac{X_3}{X_1}}{\frac{n_5}{n_7} - \frac{n_1}{n_7}\frac{X_1}{X_3} - \frac{X_2}{X_1}}} \tag{7.77}$$

$$b_1 = \sqrt{-\frac{n_1}{n_7}\frac{1}{X_1 X_3}} \tag{7.78}$$

$$b_2 = \frac{\omega_2 X_1}{\frac{-n_5}{n_7} + \frac{n_1}{n_7}\frac{X_1}{X_3} + \frac{X_2}{X_1}} \tag{7.79}$$

$$b_3 = \frac{-\omega_2\omega_3}{(\frac{n_5}{n_7} + w_1^2 + w_2^2 + w_3^2 + \frac{w_1 w_2}{b_1 b_2})b_2} \tag{7.80}$$

$$X_1 = \frac{n_6 - \frac{n_0 n_7}{n_1} - \frac{n_5}{n_7}}{n_7} \tag{7.81}$$

$$X_2 = \frac{n_4 - \frac{n_0 n_5}{n_1} - \frac{n_3}{n_7}}{n_7} \tag{7.82}$$

$$X_3 = \frac{n_2 - \frac{n_0 n_3}{n_1} - \frac{n_1}{n_7}}{n_7} \tag{7.83}$$

7.5 Sixfold-band band-pass filter based on ABSRs.

This part give the theoretical responses and measurement results for sixfold-band band-pass filters based on ABSRs. Fig. 7.3 shows the layout of the filter and its simulated and measured S-parameters. Table. 7.4 give the filters' dimensions. A good correlation is obtained by EM simulation and measurement except in terms of insertion losses. Nevertheless, the important measured losses (between 3.3 and 5.5 dB according to the band) are mainly due to the internal low-cost laser etching realization process which alters the substrate characteristics. The adjacent band-to-band isolation are above 36.1dB, 41.1dB, 38.4dB, 41.7dB and 39.2dB respectively which shows we can achieve sharp and deep rejections between the adjacent pass-bands.

7.6 Conclusion and perspectives

Quad-band case with mixed-inline topology

This appendix presents the expressions of all the n_p coefficients ($n_p \in [0; 7]$) as a function of the cut-off angular frequencies firstly and then as a function of the resonant angular frequencies and the susceptance slope parameters.

$$b_0 = \sqrt{\frac{-n_0}{n_1 n_7}} \tag{7.84}$$

$$\omega_0 = \sqrt{\frac{-n_0 n_7}{n_1}} \tag{7.85}$$

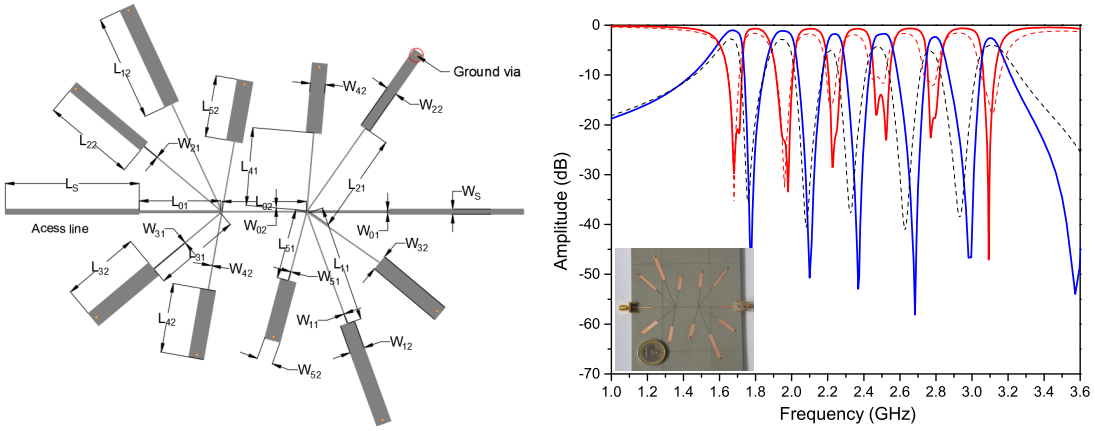

(a) (b)

Figure 7.3 – Schematic of sext-band band-pass filter based on ABSRs (a); EM-simulated (dotted lines) and measured(solid lines) S-parameters of the sext-band band-pass filter (b).

For the band-stop resonant frequencies and slop parameters, we can extract them step by step, firstly, we can get the resonant frequency of the resonant frequency of the last resonator, it's the square roots of the maximum value of the following equation:

$$n_7\omega_3^6 + n_5\omega_3^4 + n_3\omega_3^2 + n_1 = 0 \tag{7.86}$$

the following solved value is b_3,

$$b_3 = \omega_3\sqrt{\frac{2\omega_3^2 + \frac{n_5}{n_7}\omega_3^4 - \frac{n_1}{n_7}}{X_1\omega_3^4 + X_2\omega_3^2 + X_3}} \tag{7.87}$$

When we obtain the value of ω_3, b_3, the other needed values can be solved step by step.

$$\omega_2 = \frac{1}{\omega_3^2}\sqrt{\frac{2\omega_3^2 + \frac{n_1}{n_7}\frac{\omega_3}{b_3}}{X_1 - \frac{\omega_3}{b_3}}} \tag{7.88}$$

$$\omega_1 = \sqrt{\frac{-n_1}{n_7\omega_2^2\omega_3^2}} \tag{7.89}$$

$$b_2 = \frac{-\omega_1\omega_3}{b_1\frac{n_5}{n_7} + \omega_1^2 + \omega_2^2 + \omega_3^2} \tag{7.90}$$

$$b_1 = \frac{\omega_1}{X_1 - \frac{\omega_3}{b_3}} \tag{7.91}$$

Table 7.4 – Dimension of the sext-band band-pass filters with ABSR.

Symbol	Values (mm)	Symbol	Values (mm)
L_{J01}	18.55	W_{J01}	0.47
L_{J02}	19.0	W_{J02}	0.18
L_{11}	26.64	W_{11}	0.10
L_{12}	23.81	W_{12}	2.35
L_{21}	22.83	W_{21}	0.10
L_{22}	20.73	W_{22}	2.38
L_{31}	19.96	W_{231}	0.11
L_{32}	17.60	W_{32}	3.55
L_{41}	17.73	W_{41}	0.12
L_{42}	15.60	W_{42}	3.36
L_{51}	15.98	W_{51}	30.10
L_{52}	13.80	W_{52}	3.55

$$X_1 = \frac{n_6 - \frac{n_0 n_7}{n_1} - \frac{n_5}{n_7}}{n_7} \tag{7.92}$$

$$X_2 = \frac{n_4 - \frac{n_0 n_5}{n_1} - \frac{n_3}{n_7}}{n_7} \tag{7.93}$$

$$X_3 = \frac{n_2 - \frac{n_0 n_3}{n_1} - \frac{n_1}{n_7}}{n_7} \tag{7.94}$$

List of Figures

List of Tables

List of Publications

International Journals

— Y. Wu, E. Fourn, P. Besnier, and C. Quendo, "Direct synthesis of multiband band-pass filters with generalized frequency transformation methods,"IEEE Transactions on Microwave Theory and Techniques, accepted for publication, 2021.

International Conferences

— Y. Wu, E. Fourn, and P. Besnier, "Novel sext-band band-pass filter with non-coupled structure based on multi-shorted-stub resonators," in 2020 Asia-Pacific Microwave Conference (APMC2020), 2020.

— Y. Wu, E. Fourn, P. Besnier, and C. Quendo, "Direct synthesis of quad-band band-pass filter by frequency transformation methods," in 2019 49$^{\text{th}}$ European Microwave Conference(EuMC), pp. 196–199, 2019.

National Conferences

— Y. Wu, E. Fourn, and P. Besnier and C. Quendo, "Synthèse de filtres quadri-bandes par transformation de fréquences et implémentation en technologie microruban," in XXI$^{\text{èmes}}$ Journées Nationales Microondes(JNM2019), 2019.

BIBLIOGRAPHY

[1] L. Zhu, High-Q Multi-band Filters. University of Waterloo, 2019.

[2] H. Miyake, S. Kitazawa, T. Ishizaki, T. Yamada, and Y. Nagatomi, "A miniaturized monolithic dual band filter using ceramic lamination technique for dual mode portable telephones," in 1997 IEEE MTT-S International Microwave Symposium Digest, vol. 2. IEEE, 1997, pp. 789–792.

[3] V. Crnojević-Bengin, Advances in multi-band microstrip filters. Cambridge University Press, 2015.

[4] L.-C. Tsai and C.-W. Hsue, "Dual-band bandpass filters using equal-length coupled-serial-shunted lines and z-transform technique," IEEE Transactions on Microwave Theory and Techniques, vol. 52, no. 4, pp. 1111–1117, 2004.

[5] C. Quendo, E. Rius, A. Manchec, Y. Clavet, B. Potelon, J.-F. Favennec, and C. Person, "Planar tri-band filter based on dual behavior resonator (dbr)," in 2005 European Microwave Conference, vol. 1. IEEE, 2005.

[6] C. Law and K. M. Cheng, "A new, compact, low-loss, microstrip filter design for tri-band applications," in 2008 Asia-Pacific Microwave Conference. IEEE, 2008, pp. 1–5.

[7] V. Lunot, S. Bila, and F. Seyfert, "Optimal synthesis for multi-band microwave filters," in 2007 IEEE/MTT-S International Microwave Symposium. IEEE, 2007, pp. 115–118.

[8] X. Guo, L. Zhu, and W. Wu, "Design method for multiband filters with compact configuration in substrate integrated waveguide," IEEE Transactions on Microwave Theory and Techniques, vol. 66, no. 6, pp. 3011–3018, 2018.

[9] C.-Y. Chen and C.-Y. Hsu, "A simple and effective method for microstrip dual-band filters design," IEEE Microwave and Wireless Components Letters, vol. 16, no. 5, pp. 246–248, 2006.

[10] X. Y. Zhang, J. Shi, J.-X. Chen, and Q. Xue, "Dual-band bandpass filter design using a novel feed scheme," IEEE Microwave and Wireless Components Letters, vol. 19, no. 6, pp. 350–352, 2009.

[11] S. Luo and L. Zhu, "A novel dual-mode dual-band bandpass filter based on a single ring resonator," IEEE microwave and wireless components letters, vol. 19, no. 8, pp. 497–499, 2009.

[12] S. Sun, "A dual-band bandpass filter using a single dual-mode ring resonator," IEEE Microwave and Wireless Components Letters, vol. 21, no. 6, pp. 298–300, 2011.

[13] J. Xu, W. Wu, and C. Miao, "Compact microstrip dual-/tri-/quad-band bandpass filter using open stubs loaded shorted stepped-impedance resonator," IEEE Transactions on Microwave Theory and Techniques, vol. 61, no. 9, pp. 3187–3199, 2013.

[14] L. Zhu, R. R. Mansour, and M. Yu, "Compact waveguide dual-band filters and diplexers," IEEE Transactions on Microwave Theory and Techniques, vol. 65, no. 5, pp. 1525–1533, 2017.

[15] L. Zhu, R. R. Mansour, and M. Yu, "Triple-band cavity bandpass filters," IEEE Transactions on Microwave Theory and Techniques, vol. 66, no. 9, pp. 4057–4069, 2018.

[16] S. Bila, R. Cameron, P. Lenoir, V. Lunot, and F. Seyfert, "Chebyshev synthesis for multi-band microwave filters," in 2006 IEEE MTT-S International Microwave Symposium Digest. IEEE, 2006, pp. 1221–1224.

[17] G. Macchiarella and S. Tamiazzo, "A design technique for symmetric dualband filters," in IEEE MTT-S International Microwave Symposium, 2005, pp. 115–118.

[18] G. Macchiarella and S. Tamiazzo, "Design techniques for dual-passband filters," IEEE Transactions on Microwave Theory and Techniques, vol. 53, no. 11, pp. 3265–3271, 2005.

[19] R. J. Cameron, C. M. Kudsia, and R. R. Mansour, Microwave filters for communication systems: fundamentals, design, and applications. John Wiley & Sons, 2018.

[20] J.-S. G. Hong and M. J. Lancaster, Microstrip filters for RF/microwave applications. John Wiley & Sons, 2004, vol. 167.

[21] F. Martin, L. Zhu, J. Hong, and F. Medina, Balanced microwave filters. John Wiley & Sons, 2018.

[22] L. Zhu, S. Sun, and R. Li, Microwave bandpass filters for wideband communications. John Wiley & Sons, 2011, vol. 232.

[23] S. Luo, L. Zhu, and S. Sun, "A dual-band ring-resonator bandpass filter based on two pairs of degenerate modes," IEEE Transactions on Microwave Theory and Techniques, vol. 58, no. 12, pp. 3427–3432, 2010.

[24] X. Y. Zhang, J.-X. Chen, Q. Xue, and S.-M. Li, "Dual-band bandpass filters using stub-loaded resonators," IEEE Microwave and Wireless Components Letters, vol. 17, no. 8, pp. 583–585, 2007.

[25] L. Gao, X. Y. Zhang, B.-J. Hu, and Q. Xue, "Novel multi-stub loaded resonators and their applications to various bandpass filters," IEEE Transactions on Microwave Theory and Techniques, vol. 62, no. 5, pp. 1162–1172, 2014.

[26] F.-C. Chen, Q.-X. Chu, and Z.-H. Tu, "Tri-band bandpass filter using stub loaded resonators," Electronics Letters, vol. 44, no. 12, pp. 747–749, 2008.

[27] W.-Y. Chen, M.-H. Weng, and S.-J. Chang, "A new tri-band bandpass filter based on stub-loaded step-impedance resonator," IEEE Microwave and Wireless Components Letters, vol. 22, no. 4, pp. 179–181, 2012.

[28] S. Amari and U. Rosenberg, "New in-line dual-and triple-mode cavity filters with nonresonating nodes," IEEE transactions on microwave theory and techniques, vol. 53, no. 4, pp. 1272–1279, 2005.

[29] K. Zhou, C.-X. Zhou, and W. Wu, "Substrate-integrated waveguide dual-mode dual-band bandpass filters with widely controllable bandwidth ratios," IEEE Transactions on Microwave Theory and Techniques, vol. 65, no. 10, pp. 3801–3812, 2017.

[30] H.-W. Xie, K. Zhou, C.-X. Zhou, and W. Wu, "Substrate-integrated waveguide triple-band bandpass filters using triple-mode cavities," IEEE Transactions On Microwave Theory And Techniques, vol. 66, no. 6, pp. 2967–2977, 2018.

[31] K. Zhou, C.-X. Zhou, and W. Wu, "Dual-mode characteristics of half-mode siw rectangular cavity and applications to dual-band filters with widely separated passbands," IEEE Transactions on Microwave Theory and Techniques, vol. 66, no. 11, pp. 4820–4829, 2018.

[32] W. Ieu, D. Zhou, D. Zhang, and D. Lv, "Compact dual-mode dual-band hmsiw bandpass filters using source–load coupling with multiple transmission zeros," Electronics Letters, vol. 55, no. 4, pp. 210–222, 2019.

[33] R. Li, X. Tang, and F. Xiao, "Substrate integrated waveguide dual-mode filter using slot lines perturbation," Electronics Letters, vol. 46, no. 12, pp. 845–846, 2010.

[34] M. Rezaee and A. R. Attari, "Realisation of new single-layer triple-mode substrate-integrated waveguide and dual-mode half-mode substrate-integrated waveguide filters using a circular shape perturbation," IET Microwaves, Antennas & Propagation, vol. 7, no. 14, pp. 1120–1127, 2013.

[35] W. Shen, X.-W. Sun, W.-Y. Yin, J.-F. Mao, and Q.-F. Wei, "A novel single-cavity dual mode substrate integrated waveguide filter with non-resonating node," IEEE Microwave and Wireless Components Letters, vol. 19, no. 6, pp. 368–370, 2009.

[36] K. Zhou, C. Zhou, and W. Wu, "Substrate-integrated waveguide triple-band filter with improved frequency and bandwidth allocations," Electronics Letters, vol. 54, no. 19, pp. 1132–1134, 2018.

[37] K. Zhou, C.-X. Zhou, H.-W. Xie, and W. Wu, "Synthesis design of siw multiband bandpass filters based on dual-mode resonances and split-type dual-and triple-band responses," IEEE Transactions on Microwave Theory and Techniques, vol. 67, no. 1, pp. 151–161, 2018.

[38] X. Nicholson, Y. Shang, G. Wang, and M. Lancaster, "Design of multiple-passband filters using coupling matrix optimization," IET Microw. Antennas Propag, vol. 6, no. 1, pp. 24–30, 2012.

[39] Y. Zhang, K. A. Zaki, J. A. Ruiz-Cruz, and A. E. Atia, "Analytical synthesis of generalized multi-band microwave filters," in 2007 IEEE/MTT-S International Microwave Symposium. IEEE, 2007, pp. 1273–1276.

[40] G. Macchiarella, "Accurate synthesis of inline prototype filters using cascaded triplet and quadruplet sections," IEEE transactions on microwave theory and techniques, vol. 50, no. 7, pp. 1779–1783, 2002.

[41] U. Rosenberg and S. Amari, "Novel coupling schemes for microwave resonator filters," IEEE Transactions on Microwave Theory and Techniques, vol. 50, no. 12, pp. 2896–2902, 2002.

[42] R. J. Cameron, "Advanced coupling matrix synthesis techniques for microwave filters," IEEE Transactions on Microwave Theory and Techniques, vol. 51, no. 1, pp. 1–10, 2003.

[43] M. Mokhtaari, J. Bornemann, K. Rambabu, and S. Amari, "Coupling-matrix design of dual and triple passband filters," IEEE Transactions on Microwave Theory and Techniques, vol. 54, no. 11, pp. 3940–3946, 2006.

[44] M. Mokhtaari, J. Bornemann, and S. Amari, "Coupling-matrix design of dual/triple-band uni-planar filters," in 2006 IEEE MTT-S International Microwave Symposium Digest. IEEE, 2006, pp. 515–518.

[45] A. G. Lamperez, "Analytical synthesis algorithm of dual-band filters with asymmetric pass bands and generalized topology," in 2007 IEEE/MTT-S International Microwave Symposium. IEEE, 2007, pp. 909–912.

[46] A.-S. Liu, T.-Y. Huang, and R.-B. Wu, "A dual wideband filter design using frequency mapping and stepped-impedance resonators," IEEE transactions on microwave theory and techniques, vol. 56, no. 12, pp. 2921–2929, 2008.

[47] X.-P. Chen, K. Wu, and Z.-L. Li, "Dual-band and triple-band substrate integrated waveguide filters with chebyshev and quasi-elliptic responses," IEEE Transactions on Microwave Theory and Techniques, vol. 55, no. 12, pp. 2569–2578, 2007.

[48] H. Di, B. Wu, X. Lai, and C.-H. Liang, "Synthesis of cross-coupled triple-passband filters based on frequency transformation," IEEE microwave and wireless components letters, vol. 20, no. 8, pp. 432–434, 2010.

[49] J. Lee and K. Sarabandi, "Design of triple-passband microwave filters using frequency transformations," IEEE Transactions on Microwave Theory and Techniques, vol. 56, no. 1, pp. 187–193, 2008.

[50] A. Garcia-Lamperez and M. Salazar-Palma, "Single-band to multiband frequency transformation for multiband filters," IEEE Transactions on Microwave Theory and Techniques, vol. 59, no. 12, pp. 3048–3058, 2011.

[51] X. Guo, L. Zhu, and W. Wu, "Design method for multiband filters with compact configuration in substrate integrated waveguide," IEEE Transactions on Microwave Theory and Techniques, vol. 66, no. 6, pp. 3011–3018, 2018.

[52] G. Mansour, M. J. Lancaster, P. S. Hall, P. Gardner, and E. Nugoolcharoenlap, "Design of filtering microstrip antenna using filter synthesis approach," Progress In Electromagnetics Research, vol. 145, pp. 59–67, 2014.

[53] A. Manchec, Y. Clavet, C. Quendo, E. Rius, J. F. Favennec, and C. Person, "Cross-coupled microstrip dual behavior resonator (dbr) filter," in 2006 European Microwave Conference. IEEE, 2006, pp. 556–559.

[54] J.-C. Lu, Y.-W. Lin, C.-K. Liao, and C.-Y. Chang, "Five-pole parallel-coupled microstrip cascade quadruplet filters for high selectivity and flat group delay," in 2009 Asia Pacific Microwave Conference. IEEE, 2009, pp. 878–881.

[55] Y. Wu, E. Fourn, P. Besnier, and C. Quendo, "Direct synthesis of quad-band band-pass filter by frequency transformation methods," in 2019 49th European Microwave Conference (EuMC). IEEE, 2019, pp. 196–199.

[56] C. Quendo, A. Manchec, Y. Clavet, E. Rius, J.-F. Favennec, and C. Person, "General synthesis of n-band resonator based on n-order dual behavior resonator," IEEE microwave and wireless components letters, vol. 17, no. 5, pp. 337–339, 2007.

[57] J. Xu, W. Wu, and C. Miao, "Compact microstrip dual-/tri-/quad-band bandpass filter using open stubs loaded shorted stepped-impedance resonator," IEEE Transactions on Microwave Theory and Techniques, vol. 61, no. 9, pp. 3187–3199, 2013.

[58] Q. Yang, Y.-C. Jiao, and Z. Zhang, "Compact multiband bandpass filter using low-pass filter combined with open stub-loaded shorted stub," IEEE Transactions on Microwave Theory and Techniques, vol. 66, no. 4, pp. 1926–1938, 2018.

[59] H.-W. Wu and R.-Y. Yang, "A new quad-band bandpass filter using asymmetric stepped impedance resonators," IEEE Microwave and Wireless Components Letters, vol. 21, no. 4, pp. 203–205, 2011.

[60] Y. Zhang, L. Gao, and X. Y. Zhang, "Compact quad-band bandpass filter for dcs/wlan/wimax/5g wi-fi application," IEEE Microwave and Wireless Components Letters, vol. 25, no. 10, pp. 645–647, 2015.

[61] K.-W. Hsu, W.-C. Hung, and W.-H. Tu, "Compact quint-band microstrip bandpass filter using double-layered substrate," in 2013 IEEE MTT-S International Microwave Symposium Digest (MTT). IEEE, 2013, pp. 1–4.

[62] C.-F. Chen, "Design of a compact microstrip quint-band filter based on the tri-mode stub-loaded stepped-impedance resonators," IEEE microwave and wireless components letters, vol. 22, no. 7, pp. 357–359, 2012.

[63] G. Macchiarella and S. Tamiazzo, "Cooking microwave filters: Is synthesis still helpful in microwave filter design?" IEEE Microwave Magazine, vol. 21, no. 3, pp. 20–33, 2020.

[64] R. V. Snyder, G. Macchiarella, S. Bastioli, and C. Tomassoni, "Emerging trends in techniques and technology as applied to filter design," IEEE Journal of Microwaves, vol. 1, no. 1, pp. 317–344, 2021.

[65] J. D. Rhodes and R. J. Cameron, "General extracted pole synthesis technique with applications to low-loss te/sub011/mode filters," IEEE Transactions on Microwave Theory and Techniques, vol. 28, no. 9, pp. 1018–1028, 1980.

[66] M. Yu and Y. Yang, "Unified extracted pole filter synthesis: Bridging the gap between em and circuit simulations," IEEE Microwave Magazine, vol. 21, no. 3, pp. 84–95, 2020.

[67] G. Macchiarella and S. Tamiazzo, "Design of extracted-pole filters: An application-oriented synthesis approach," in 2020 IEEE/MTT-S International Microwave Symposium (IMS). IEEE, 2020, pp. 440–443.

[68] G. Macchiarella and S. Tamiazzo, "An application-oriented design procedure for cascaded-block extracted-pole filters," IEEE Transactions on Microwave Theory and Techniques, 2020.

[69] S. Amari and G. Macchiarella, "Synthesis of inline filters with arbitrarily placed attenuation poles by using nonresonating nodes," IEEE Transactions on Microwave Theory and Techniques, vol. 53, no. 10, pp. 3075–3081, 2005.

INSA de RENNES
Service des Formations

AVIS DU JURY SUR LA REPRODUCTION DE LA THESE SOUTENUE

Titre de la thèse:
Development of Multiband Band-Pass Filters in Planar Technologies

Nom Prénom de l'auteur : WU YI

Membres du jury :
- Monsieur BILA Stéphane
- Monsieur PRIGENT Gaëtan
- Monsieur BESNIER Philippe
- Monsieur QUENDO Cédric
- Madame PODEVIN Florence
- Monsieur FOURN Erwan

Président du jury : QUENDO Cédric

Date de la soutenance : 18 Juin 2021

Reproduction de la these soutenue

☒ Thèse pouvant être reproduite en l'état
☐ Thèse pouvant être reproduite après corrections suggérées

Fait à Rennes, le 18 Juin 2021

Signature du président de jury

Le Directeur,

Abdellatif MIRAOUI

DOCTORAT BRETAGNE LOIRE / MATHSTIC

INSA RENNES

Titre : Développement de filtres multibandes en technologies planaires

Mots clés : Filtre hyperfréquence, multibande, filtre passe-bande, technologie planaire

Résumé : Les évolutions récentes dans le développement des systèmes de communicationont grandement stimulé la demande d'équipe-ments multifonctions. Les composants micro-ondes doivent aujourd'hui être compacts, très performants et faible coût. Parmi tous les composants d'un système de communication, les filtres passe-bandes joue un rôle essentiel. Depuis quelques temps, les filtres multibandes font l'objet de nombreuses études pour leur capacité à opérer simultanément sur au moins deux bandes de fréquences distinctes. Dans cette thèse, nous nous concentrons sur ce type de composants et plus particulièrement sur leur synthèse et leur conception dans différentes topologies et sur leur implémentation en technologie microruban.

Dans ce document, nous explorons tout d'abord une première technique de conception de filtres multibandes basée sur une méthode de transformation de fréquences.

Une topologie en étoile est proposée pour synthétiser et implémenter ces filtres mutlibandes en utilisant soit des structures non couplées soit au contraire des structures couplées. Une seconde topologie d'implémentation en ligne cette fois est ensuite proposée pour concevoir des filtres multibandes. Cette seconde topologie permet plus facilement d'augmeter le nombre de bandes passantes au delà de 6 simultanément. Enfin, une dernière topologie de résonateurs multibandes basée sur l'association de résonateur coupe-bande est proposée. Elle permet d'obtenir rapidement des structures présentant un grand nombre de bandes. Toutes les méthodes de conception proposées ci-dessus ont été validées théoriquement et expérimentalement. Les résultats expérimentaux obtenus, en très bonne corrélation avec les simulations, démontrent l'efficacité de ces méthodes.

Title : Development of Multiband Band-Pass Filters in Planar Technologies

Keywords : Microwave filter, multiband, band-pass filter, planar technologies

Abstract : Recent advances in the develop-ment of communication systems have greatly stimulated the demand on multi-function equip-ment. Compact, high performance, and lower cost RF/microwave devices are all necessary and required today. Among these devices, band-pass filters play an irreplaceable role in any type of RF/microwave communication systems. Even more recently, multiband filters have been widely studied due to the ability to operate at two or more independent frequency bands simultaneously. In this thesis, we focus on such components and more precisely on their synthesis and design with different topologies and make their implementation with microstrip technology.

In this dissertation, first, we explore the synthesis strategy with frequency transformation method. A star-like topology was proposed to synthesis and design multiband band-pass filters with non-coupled and compact coupled structures. Second, an advanced in-line topology was presented to design multiband band-pass filter up to sixfold-band. In the last part, a novel multiband resonator named associated band-stop resonator is proposed to design quickly high-order multiband band-pass filters. The above-mentioned synthesis techniques have been verified theoretically and experimentally. The obtained experimental results, in very good correlation with simulated ones, prove the effectiveness of the proposed methods.